Palacký University Olomouc
Faculty of Science

Department of Optics

# Photonic switching for quantum information processing

Ph.D. Thesis

Vojtěch Švarc

Palacký University Olomouc
Faculty of Science

Department of Optics

# Photonic switching for quantum information processing

Ph.D. Thesis

Author: Mgr. Vojtěch Švarc
Study programme: B1701 Physics
Field of study: Optics and Optoelectronics
Form of study: Full-time
Supervisor: prof. Mgr. Jaromír Fiurášek, Ph.D..
Co-supervisor: RNDr. Miroslav Ježek, Ph.D.

Thesis submitted on: .....

Univerzita Palackého
Přírodovědecká fakulta

Katedra optiky

# Fotonické spínání pro kvantové zpracování informace

Disertační práce

Autor: Mgr. Vojtěch Švarc
Studijní program: B1701 Fyzika
Studijní obor: Optika a optoelektronika
Forma studia: Prezenční
Školitel: prof. Mgr. Jaromír Fiurášek, Ph.D.
Konzultant: RNDr. Miroslav Ježek, Ph.D.

Práce odevzdána dne: .....

## Abstract

Photonic switches represent valuable tools in quantum technologies and quantum optics in general. In this Thesis, we discuss different platforms for photonic switching and address a wide scale of applications across all fields of quantum optics. We implement photonic switching experimentally via a Mach-Zehnder interferometer with embedded integrated electro-optic phase modulators. We reach versatile sub-ns low-latency switching with 26 dB extinction, convenient for a feedforward operation. To provide long-term stability of the interferometer, we implement active phase locking. The phase lock exploits external reference light operating on a different wavelength than the quantum signal. This solution enables stability of 0.05 degrees maintained over 15 hours. Further, we propose and demonstrate applications of the photonic switch. Firstly, we perform active time multiplexing via a loop configuration of the photonic switch. We achieve complete control over 4 time bins, allowing for qudit preparation or photon-number-resolving detection. Secondly, we theoretically investigate Fock state conversion with linear optics. The proposed protocol probabilistically converts $m$-photon state to $n$-photon state by subtracting $m - n$ photons at a sequence of feedforward-controlled beam splitters. We verify the feasibility of the protocol by experimental $|2\rangle$ to $|1\rangle$ conversion using an extended version of the photonic switch.

## Keywords

`Photonic switching, Mach-Zehnder interferometer, interference, phase modulation, active phase locking, Fock state conversion, photon subtraction, feedforward, linear optics`

**Acknowledgments**

I would like to express my deepest appreciation to Miroslav Ježek for his invaluable mentoring, insightful advice, and unwavering support throughout my Ph.D. I am extremely grateful to Jaromír Fiurášek for his patient guidance and valuable feedback throughout the preparation of this Thesis.

I am also thankful to all my collaborators and colleagues for their company, advice, and help whenever I needed it. Special thanks to Gleb Mazin being not only an enthusiastic cooperator but also my great friend. Many thanks to Martina Nováková as an outstanding leader at the beginning of my Ph.D. and during my master's and bachelor's studies. Thanks should also go to Jirka Fadrný, Pepa Hloušek, and Michal Dudka for exemplary cooperation. Without you, the research presented in this Thesis would not be possible. I am also grateful to QuantumFuture Research Group in Padova. Thank you for warm adoption into your wonderful team during my Ph.D. internship. Especially I would like to acknowledge Francesco Santaguistina for excellent collaboration and friendly companionship.

I would be remiss in not mentioning all my friends and musicians who have been supporting me and have been giving me joy that helped me to stay sane during my Ph.D. studies. Last but not least, I would like to extend my sincere thanks to my family for their continuous support and unconditional love giving me through my journey of life.

Vojtěch Švarc

**Declaration**

I hereby declare I have written this Ph.D. Thesis by myself while being supervised by prof. Mgr. Jaromír Fiurášek, Ph.D. and RNDr. Miroslav Ježek, Ph.D. Also, I declare that every resource used is properly cited. I confirm this Thesis is based on original research, clarifying my personal contribution to individual projects in Author contribution. I agree with the Thesis being used for teaching purposes and being made available on the website of the Department of Optics.

Signed in Olomouc on ..... .....

Vojtěch Švarc

## Author contribution

This Thesis is based on three publications where I act as the first author. Here, let me clarify my personal contribution to the individual research projects.

In work [1], I was responsible for the experimental implementation, measurements, and data processing, being supervised by Martina Nováková and Miroslav Ježek. Further, I participated in the manuscript preparation. Gleb Mazin contributed to the time-multiplexing part by FPGA programming and driving the phase modulator via his hardware.

This work was further extended in publication [2], where we focused on the optimization of the active phase locking. The optimization to the current precision is predominantly a result of my own research, ideas, and experimental implementations. For example, I developed the concept of local setup detuning, limiting the long-term stability. Further, I optimized the experimental setup, performed all measurements, data analysis, and prepared the manuscript. Miroslav Ježek supported me with ideas and advice, and he also provided me with feedback on the manuscript. Michal Dudka contributed by assembling an improved version of the PID controller.

The project [3] can be divided into a theoretical section and an experimental section. The theoretical section, including the concept, theory, simulations, and an experimental proposal, was performed by Jaromír Fiurášek. My personal contribution in this part laid in a revision of his findings. The experimental section, consisting of the experimental implementation, measurements, and data evaluations, was predominantly performed by me. Josef Hloušek helped me with a coincidence unit and also shared with me a part of his experimental setup. Miroslav Ježek coordinated the theoretical and experimental parts. Regarding the manuscript preparation, Jaromír Fiurášek was the main coordinator. He prepared the theoretical part while I described the experimental part. Miroslav Ježek revised the manuscript.


[1] V. Švarc, M. Nováková, G. Mazin, and M. Ježek, "Fully tunable and switchable coupler for photonic routing in quantum detection and modulation," *Opt. Lett.* 44, 5844-5847 (2019)

[2] V. Švarc, M. Nováková, M. Dudka, and M. Ježek, "Sub-0.1 degree phase locking of a single-photon interferometer," *Opt. Express* 31, 12562-12571 (2023)

[3] V. Švarc, J. Hloušek, M. Nováková, J. Fiurášek, and M. Ježek, "Feedforward-enhanced Fock state conversion with linear optics," *Opt. Express* 28, 11634-11644 (2020)

# Contents

# Chapter 1

# Introduction

A century has passed since the fundamental principles of quantum theory were formulated. Quantum physics exhibits many counterintuitive properties with no equivalent in classical physics such as superposition principle, quantum interference, and non-locality. Although initially there were limited possibilities to experimentally verify all of these properties, experiments were eventually implemented to confirm predictions of quantum theory. Later, applications utilizing the unique properties of quantum systems were proposed. Quantum communication can prevent leakage of secret information to an eavesdropper leading to inherently secure communication. Quantum metrology breaks classical limits for measurement precision enabling gravitional wave observation with unprecedented sensitivity [4]. Quantum information protocols outperform classical computers in specific tasks [5]. The holy grail of quantum information processing, the universal quantum computing, has a potential application in many fields. Large scale of combinatorics problems will be solved more efficiently, impacting advanced manufacturing, banking, and financial sector [6]. Also, quantum simulations for chemical engineering could be done much efficiently, massively improving the development of new materials. On the other hand, the advent of efficient quantum computing would threaten encryption methods used today. To implement quantum applications, various quantum protocols are investigated on different platforms such as atoms, ions, superconducting materials, and photons.

The photonic platform is capable of quantum communication, quantum metrology as well as universal quantum computing. However, there are enormous technological demands for efficient single-photon generation, advanced quantum state processing, and efficient detection of photons to make the photonic-based protocols applicable in practice. Advanced quantum state processing often requires fast switching between two or more modes or their mixing. In some cases, we need to perform a specific operation depending

on the result of a measurement. This operation is referred to as feedforward. Therefore, it is extremely useful to achieve fast photonic routing with low latency. Photonic switching is used in quantum cryptography [7], photonic simulations [8], scalable boson sampling [9–11], universal quantum computing [12, 13], entanglement synthesizing [14], and multi-mode quantum processing [15]. Further, fast photonic switching has facilitated a pioneering demonstration of postselection-loophole-free violation of Bell's inequality with genuine time-bin entanglement [16]. Fast switching also plays an important role in single-photon generation and photon counting. Specifically, in the last few years, high-efficiency single-photon generation has been demonstrated employing active time multiplexing [17–20]. In addition, active time multiplexing was used to demonstrate a high-dynamic range photon-number-resolving detection [21].

A convenient way to achieve fast photonic switching with low latency is to employ a Mach-Zehnder interferometer with an integrated phase modulator. In this case, 100 GHz response is feasible [22] and thanks to the low-voltage control of the modulator, low latency and high repetition rate are provided. A major drawback lies in the environmentally-induced phase drift in the Mach-Zehnder interferometer. Although inherently stable configurations exist, they are not free of issues and do not fit all applications. Therefore, commonly the long-term stability of the Mach-Zehnder interferometer requires active phase locking. Active phase locking at a single-photon level is feasible but extremely challenging due to Poissonian photodetection noise. As a consequence, the typical precision of single-photon phase locking is a few degrees, and the response is slower than 0.1 s [23, 24]. An efficient strategy to overcome this issue is to lock the phase via a bright reference light co-propagating with the signal photons [2, 25–27].

In this Thesis, we present experimental research in the field of photonic switching for single-photon applications with an emphasis on quantum information processing. We have implemented an ultra-fast photonic switch by using a Mach-Zehnder interferometer with an embedded integrated electro-optic modulator. Also, we provided the Mach-Zehnder interferometer with continuous active phase locking by adding a reference beam to the setup. We achieved stability of 0.05 degrees for 15 hours which is an unprecedented result within actively stabilized single-photon interferometers. Further, we present applications of photonic switching: Firstly, the photonic switch can perform temporal multiplexing by using a loop configuration. Specifically, we demonstrate temporal multiplexing for photon-number-resolving detection and qudit preparation. Secondly, we present a theoretical and experimental protocol for Fock state conversion with linear optics. The protocol transforms arbitrary $m$-photon state to $n$-photon state by subtracting $m - n$ photons

at feedforward-controlled photonic switches. Our approach uses within each subtraction step the results of all previous subtraction steps enabling the conversion with maximal probability. We use the photonic switch for experimental proof-of-principle conversion from a two-photon state to a single-photon state.

This Thesis is structured as follows: In Chapter 2 we discuss the current state-of-the-art technology of photonic switching and phase-locking of single-photon interferometers. In Chapter 3 we present important theoretical, experimental, and technical aspects of our research. Firstly, we introduce a refined model of a Mach-Zehnder interferometer and the phase estimation under real conditions. Secondly, we discuss methods of phase control in the Mach-Zehnder interferometer. Thirdly, we provide concise explanations of photodetection and data processing in our experiments. Fourthly, relevant quantum optics theory is summarized. In Chapter 4 we present active stabilization of a Mach-Zehnder interferometer published as work [2]. In Chapter 5 we present the photonic switching via phase modulation of a Mach-Zehnder interferometer and its applications in temporal multiplexing published as work [1]. In Chapter 6 we present theoretical and experimental research in Fock state conversion published as work [3]. In Chapter 7 we summarize the main results of the Thesis.

# Chapter 2

# Contemporary state of research

Linear optics represents a promising platform for the practical implementation of quantum communication and quantum information processing. Quantum communication with photons is natural since photons can travel over a long distance without interacting directly with each other. On the other hand, the absence of direct photon-photon interaction complicates the photonic quantum information processing. To provide interaction between photons, linear optical elements such as beam splitter are commonly used. Although a large scale of quantum interactions is possible with linear optics, these interactions are often probabilistic leading to several possible outcomes. Fortunately, this problem can be mitigated by a feedforward operation [28]. Firstly, a measurement of a subsystem is performed. Then, depending on the measurement outcome, an appropriate operation is performed on the output state in order to produce the desired quantum state. The operation is performed by an active element, commonly being a photonic switch. The switch is an important part of the feedforward, and moreover, it can perform a wide range of operations efficiently even while acting deterministically in the protocol. Especially, the photonic switch becomes very powerful as a part of loop-based protocols. In this case, the switch is used repeatedly, and complex quantum operations are feasible via a relatively simple experimental design.

Recently, universal quantum computing in loop-based architecture was proposed. As shown in Fig. 2.1(a), the core part of the scheme consists of two nested loops, two on-off photonic switches, and one multi-level switch enabling multi-mode interference between time-bin encoded input state. The scheme is resource-efficient since it can hypothetically process an arbitrarily long time-bin sequence using a relatively simple design. However, performing universal quantum computing requires additional resources including non-gaussian and squeezed ancilla states. Unfortunately, these states are loss-sensitive, giving extreme demands on the technical parameters of

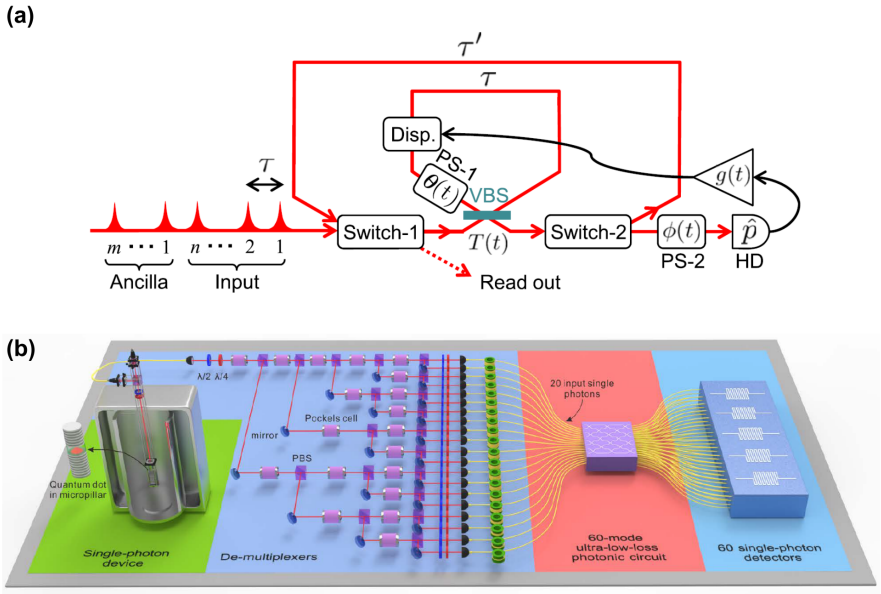


**Figure 2.1:** Quantum information processing with linear optics exploiting photonic switching. (a) Loop-based universal quantum computing. (b) Boson sampling in path mode. Panels (a) and (b) are adopted from [13] and [11], respectively.

the setup. For fault-tolerant computing, the squeezing should exceed 20.5 dB meaning the loop loss cannot exceed 1% even for perfectly squeezed ancillas. Therefore, except for the high quality of the squeezing, ultra-low-loss components including switches are required. On the other hand, the switching should be fast enough to keep the loops short and therefore increase the speed and the stability of the system while reducing the loop loss. Although practical quantum computing via this scheme still represents a technological challenge, specific blocks of the scheme were implemented with interesting results. In 2019, the inner loop with 3-level switching was realized. Using squeezed states and homodyne detection, this configuration allows for entanglement synthesizing [14]. In 2022, the outer loop was added to demonstrate arbitrary multi-mode unitary operation via this configuration [15]. Due to losses, limited switching levels, and other setup imperfections, these demonstrations were limited to three modes. Apart from quantum computing, a similar architecture enables boson sampling. Boson sampling is a generalized quantum random walk that scales exponentially for classical computers. The boson sampling employing photonic switching was demonstrated with time bins [10] and a spatial mode [11] [see Fig. 2.1(b)].

Further, the photonic switching in loop architecture is used to enhance single-photon generation. The most common single-photon sources are based

on the spontaneous-parametric-down conversion. However, this process is probabilistic and to avoid multi-photon contribution, the single-photon rate is limited. An efficient strategy how to increase the rate while avoiding multi-photon contributions is active time and spatial multiplexing of single-photon sources depicted in Fig. 2.2(a). Using photonic switching and optical delay lines, the success rate of photon generation in a given time window is increased. Kaneda et al. combined spatial and time multiplexing to reach 10× enhancement of single-photon generation [19] resulting in 67% efficiency. Also, the detection of photostatistics can be efficiently implemented by active time multiplexing [21]. Tideau et al. implemented a high-dynamic range detector enabling evaluation of photostatistics containing $10^{-7}$ up to $3 \times 10^5$ photons. As shown in Fig. 2.2(b), their scheme uses one single-photon detector, a photonic switch, and a delay line. In their approach, they split the incident pulse into a train of pulses with an exponential decay and observe the saturation effect of the single-photon detector. For a specific time bin, the saturation disappear, depending on the photon number and the photostatistics. Therefore, it is possible to reconstruct the photostatistics from the shape of the saturation pattern. Further, our research team recently demonstrated balanced photon-number-resolving detection via active time multiplexing [1]. For more information see Chapter 5.

Photonic switching is also used to probe fundamental laws of quantum physics. One of the recent fundamental tests is directly applicable in quantum communications based on energy-time entanglement. This way of communication is extremely secure since the secret key is produced during the detection. However, despite this, there are still loopholes enabling to break the security in principle. Recently, a post-selection loophole was closed elegantly by exploiting photonic switching. Typically, time bins used for the communication are prepared and overlapped via unbalanced Mach-Zehnder interferometers. However, this passive scheme results in the typical three-peak pattern, where the time bins are overlapped within the middle peak only. As a result, the interference occurs in 50% of cases and the remaining events are discarded, enabling a potential attack. Vedovato et al. closed this loophole by deterministic switching of the short bin to the longer arm and the long bin to the shorter arm as shown in Fig. 2.2(c). Consequently, a perfect overlap of the time bins is provided enabling improved security and also more effective communication since all events contribute to the secret key. Other examples of fundamental tests based on photonic switching are entanglement swapping [29] and two-dimensional quantum random walk [8].

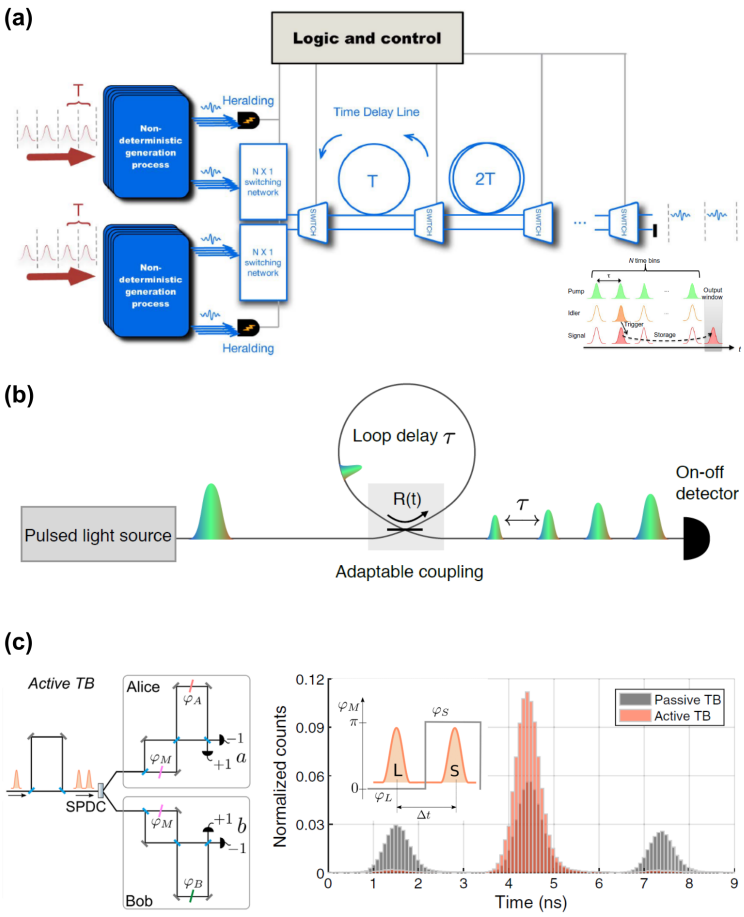


**Figure 2.2:** Other quantum applications of photonic switching. (a) Active multiplexing of single photon sources. Single photon sources with low efficiency are multiplexed in time and space via photonic switches and loops to approximate an on-demand single-photon source (adopted from [18, 19]). (b) Photon counting using active time multiplexing (adopted from [21]). (c) Postselection-loophole-free Bell test using genuine time-bin entanglement (adopted from [16]).

## 2.1 Approaches to the photonic switching

There are several techniques of photonic switching used in quantum optics. The most common switching methods are based on phase modulation in a Mach-Zehnder interferometer and polarization modulation using a Pockels cell. Alternatively, commercial latching switches or acousto-optic modulators are utilized. Each of these options has several advantages and disadvantages and each of them is suitable for a different application. Choosing the most appropriate switching method is usually a trade-off between speed, loss, and

the complexity of the switching solution. In this section, we will describe the most common methods of photonic switching and we will discuss their pros and cons.

### 2.1.1 Phase modulation

A common approach to photonic switching lies in exploiting phase modulation in a Mach-Zehnder interferometer. This solution enables to encode the quantum state into polarization degree of freedom, in contrast to polarization-based switching. There are several implementations of phase modulation, summarized in Table 2.1.

Firstly, an electro-optic modulator embedded in a fiber Mach-Zehnder interferometer is used [1,16,30]. The main advantage of this solution is the fast response of tens of GHz. Also, integrated electro-optic modulators operate with low voltage, therefore, the repetition rate can be arbitrarily high and low-latency operation is provided. Furthermore, high extinction is feasible, depending on visibility optimization. The main disadvantage of this solution is the higher loss caused mainly by inefficient in-out chip coupling. Also, fiber optics has in general higher loss than the free-space optical elements. This solution can be also fully integrated on a chip (known as the Mach-Zehnder modulator). The extinction is limited and strongly wavelength-dependent due to manufacturing imperfections causing non-balanced splitting ratios of the Mach-Zehnder interferometer beam splitters. This effect can be diminished by cascading more Mach-Zehnder interferometers [31–34] at the expense of higher loss.

If losses are more critical and the polarization mode is used to carry the quantum state, a free-space Mach-Zehnder interferometer with bulk electro-optic modulators can be used [35]. This approach cannot provide such a fast response and the repetition rate is limited, though. This fact is caused by a high voltage required to drive the bulk electro-optic modulator, analogically to polarization switching discussed further. Extinction is typically lower compared to fiber setups since it is harder to overlap precisely the interfering light beams.

Another implementation of phase modulation is the thermal tuning commonly used for on-chip optical circuits. One of the advantages is that it is possible to implement in this way complex interferometric networks performing multi-mode unitary operations [36]. Although the thermal tuning is quite simple to implement, it is slow (kHz). Electro-optic modulation cannot be used while we aim to keep the interferometric network small and thus stable, since electro-optic needs a longer interaction length (a few cm). On-chip implementations also suffer from higher loss caused mainly by inef-

| | PHASE MODULATION | | | | |
|---|---|---|---|---|---|
| modulation | ELECTRO-OPTICAL | | | THERMAL | OPTICAL |
| implementation | FIBER | | BULK | ON-CHIP | FIBER |
| work | [1] | [30] | [35] | [36] | [39] |
| bandwidth | 10 GHz | 10 GHz | 63 MHz | ∼kHz | 1-5 GHz |
| extinction | 26 dB | 19 dB | 16 dB | NA | 16-21 dB |
| loss | 7 dB | 5 dB | 5 dB | NA | 1.3-2.1 dB |
| tunability | full | full | 2 levels | full | full |
| repetition rate | arb. | arb. | 2.5 MHz | arb. | 50 MHz |
| long-term stab. | yes | no | yes | yes | NA |

**Table 2.1:** Single-photon photonic switching based on phase modulation. Electro-optical, thermal, and optical methods are used, either in free space, in fibers, or on-chip. In work [39], they present more regimes of the switch. The first provides faster operation at the expense of higher loss and lower extinction. The second regime enables for lower loss and higher extinction at the expense of slower response. Abbreviations: arb. = arbitrary, stab. = stability, NA = not available.

ficient in/out coupling although moderate coupling losses have been demonstrated [37, 38].

Finally, the phase can be modulated by an external optical pulse via Kerr non-linearity in a fiber. This solution provides a fast response while keeping loss moderate, offering an interesting alternative to phase modulation via integrated electro-optic modulators. The main disadvantage of this solution is the high delay (500-2500 ns) of the optical signal due to weak interaction between the driving and signal pulses. Although for many applications the delay does not cause any issue, in others, such as temporal multiplexing/demultiplexing, the delay represents the minimal distance between the time bins making this switch impractical for these applications. Also, we are not aware of any practical use of this switching method implying potential presence of additional issues not addressed by Hall et al.

Now let us discuss another typical issue of the phase-modulation-based switches, which is the phase stability. We will further address this topic in more detail in Section 2.3. There are three classes of Mach-Zehnder interferometer-based switches in terms of stability. The first is the classical geometry of a Mach-Zehnder interferometer containing two separate arms implemented in fiber or free space. These devices can offer the highest visibility (extinction) in general since both arms are accessible individually [1, 16]. As a consequence, it is also easy to reconfigure the setups. On the other hand, they suffer from phase instabilities requiring active phase locking to maintain

their long-term performance [1, 16, 35]. As shown in Chapter 4, ultra-precise phase locking is possible even for single-photon Mach-Zehnder interferometers. However, the price to pay is the increased complexity of the setup [2, 26].

The second class is the Sagnac geometry of the Mach-Zehnder interferometer, which is considered inherently stable since the interferometer arms are implemented as clockwise and counter-clockwise propagation through the same (or similar) path [30, 39]. The disadvantage of the Sagnac interferometer lies in the difficult addressing of individual arms. To use the Sagnac as a photonic switch, the electro-optic modulator has to be placed asymmetrically inside the Sagnac. Then, it is possible to modulate the clockwise signal while keeping the contra-clockwise signal unmodulated (or vice versa). Since the integrated electro-optic modulator is typically 5 cm long, it reduces the effective repetition rate of the setup to a few GHz [40]. Also, let us notice that even the Sagnac configuration can suffer from phase instabilities to some extent. In free-space interferometers, a small path displacement between the arms helps to address the clockwise and contra-clockwise signals, bringing a long-term thermal phase drift to the setup [41]. The same issue is present in a fiber Sagnac with polarization-independent architecture [30].

Thirdly, let us comment on the phase stability of integrated Mach-Zehnder interferometers. Although these devices are considered inherently stable as well, in practice, they may suffer from long-term phase drift, depending on the Mach-Zehnder interferometer length. While thermally tuned devices can be very short and thus inherently stable, electro-optic modulation-based interferometers are several cm long since the electro-optic interaction is weaker. Then, a slow phase drift is present, however [40].

### 2.1.2 Polarization modulation

If the speed and repetition rate are not crucial but the loss is critical, polarization-based switching in free space is the best choice. In this case, indeed, the polarization mode cannot be a carrier of the quantum state. A typical application in the context of quantum optics is the active time multiplexing of single-photon sources, single-photon counting, boson sampling, entanglement synthesizing, or implementation of multi-mode quantum operations in the time domain [10, 14, 15, 19, 21]. These approaches and their parameters are summarized in Table 2.2.

Polarization-based switching is performed by using a Pockels cell and two polarizing beam splitters. Pockels cell acts as a waveplate with a voltage-controlled retardance. Without a voltage applied, the Pockels cell keeps the original polarization. By applying half-wave voltage, the polarization is switched to orthogonal thus the signal is switched to the second output port of

| | POLARIZATION MODULATION | | | |
|---|---|---|---|---|
| modulation | ELECTRO-OPTICAL | | | |
| implementation | BULK (Pockels cell) | | | |
| work | our new | [14] | [10] | [21] |
| bandwidth | ∼39 MHz | ∼35 MHz | 30 MHz | 150 kHz |
| min. sw. time | 60 ns | 66 ns | 130 ns | 2400 ns |
| extinction | ≥23 dB | NA | 10 dB est. | NA |
| loss | 0.1 dB | 0.1 dB | 0.2 dB | 0.1-0.2 dB est. |
| tunability | 25 levels∗ | 3 levels | ≥ 8 levels | 2 levels |
| repetition rate | ≤100 kHz | ∼ MHz est. | NA | NA |

**Table 2.2:** Single-photon photonic switching based on the polarization modulation. Pockels cells using electro-optical effect are used. Abbreviations: est. = estimated, NA = not available, min. sw. time = minimal switching time. This parameter reflects the fact that the real operation of the Pockels cells is slower than the corresponding bandwidth. The main reason is that a Pockels cell driver typically needs a minimal recovery time to reach genuine multi-level operation. ∗ 9 arbitrary tunable levels, 25 partially dependent levels

the polarizing beam splitter. Polarization-based switching is much simpler to implement compared to phase modulation in free-space Mach-Zehnder interferometer and, additionally, active phase locking is not needed. Polarization-based switching is usually used as a part of time-multiplexing schemes due to these features and ultra-low loss operation.

The main disadvantage is the high driving voltage requirement leading to limited speed and repetition rate. Also, the multi-level switching operation is hard to achieve. Commercial drivers typically offer 2-level (on-off) operation and very rarely 3-level operation. The number of switching levels determines the complexity of the time-bin processing. There is the aim to increase the number of switching levels. One way is to use low-voltage Pockels cells with a half-wave voltage of around 150 V. Then linear amplifiers can be used and the multilevel operation is enabled. However, these devices have slightly higher losses than classical Pockels cells. An alternative solution is to cascade Pockels cells at the expense of higher losses and increased complexity. Our research team has recently achieved 25-level switching using a single Pockels cell. We have developed in-house 5-level drivers providing arbitrary tunable voltages up to 500 V. Also, we acquired custom-made Pockels cells with individual control of each of the two non-linear crystals. Therefore, while combining two 5-level drivers we reach 9 arbitrarily adjustable switching levels. It corresponds to 25 partially dependent levels since the effective modulation is equal to a mean voltage applied to the individual crystals. This represents a sig-

| | OTHERS | | |
|---|---|---|---|
| modulation | LATCHING SWITCHES | | AOM |
| implementation | FIBER | | BULK |
| work | [18] | [42] | [10] |
| bandwidth | 3 MHz | 6 MHz | ≥3 MHz est. |
| extinction | 20 dB est. | 20 dB | ≥10 dB |
| loss | 3.3 dB | <0.4 dB | 0.8 dB |
| tunability | 4 levels | 2 levels | 2 levels |
| repetition rate | 500 kHz | 1 MHz | NA |

**Table 2.3:** Other methods of single-photon photonic switching. Firstly, commercial latching switches are used and, secondly, acousto-optic modulation is exploited. Abbreviations: est. = estimated, NA = not available, AOM = acousto-optic modulation. This parameter reflects the fact that the real operation of the Pockels cells is slower than the corresponding bandwidth.

nificant improvement in the low-loss photonic switching. These results were achieved very recently and the work is still in progress, not being published yet.

### 2.1.3 Other methods of photonic switching

Instead of phase modulation and polarization modulation, commercial latching switches or acousto-optic modulators summarized in Table 2.3 can be exploited. Their advantage lies in relatively easy implementation into the experimental setup, though the parameters cannot reach the phase-modulation methods nor the polarization-modulation implementations. The response is comparable to or slower than Pockels cells while having moderate losses. Also, these switches work in on-off regime solely thus more advanced modulation is not feasible. In terms of acousto-optic modulators, the frequency of the optical signal is shifted by the frequency of the acoustic wave. In most cases, it does not represent an issue or sometimes the frequency shift is even desired. However, this effect is undesired if the switched narrowband optical signal has to further interfere with the non-shifted signal.

Alternative methods of photonic switching using light-matter interactions have been investigated. Proof-of-principle photonic switching using Rydberg blockade [43], quantum-dot-cavity systems [44] or single-molecule vacuum Rabi splitting [45] was demonstrated, the extinction ratio is extremely low, though.

## 2.2 Parameters of the photonic switching

As discussed in the previous section, a perfect photonic switch has not been invented yet. Therefore, choosing a photonic switch for a specific application requires consideration of various parameters such as speed, latency, extinction, and losses. In this section, we briefly discuss these parameters in the context of quantum optics.

**Speed and latency**

Speed or response is determined by the bandwidth or, equivalently, by the rise/fall time of the switch. The switching speed determines the possible rate of the protocol if other restrictions such as limited switching repetition rate do not apply. Fast switching capability is very important in loop-based time multiplexing since its speed determines the length of an optical delay line [1, 10, 14]. Also, fast switching plays an important role in quantum communication, especially when time bins are actively transferred to path mode [16].

Another parameter, strongly connected to the speed, is latency. It determines the delay between an external triggering and the switching operation. It is important in the context of feedforward control since the higher the latency, the longer the optical delay line is required. Generally, both the speed and latency are dependent on the driving voltage of the switching (the driving electronics is as important here as the switch itself). In general, switches controlled by low voltage are much faster and also have lower latency.

**Repetition rate**

For some types of switches (those based on bulk electro-optic modulators, acousto-optic modulators, or latched switches), there is a limit on the repetition rate for the switching operation. Although the repetition rate can be restricted by the switch itself, more commonly it is given by the capabilities of driving electronics. This is valid, for example,for bulk electro-optic modulators driven by hundreds of volts or kilovolts. In the context of quantum optics, the repetition rate represents a limiting factor for the speed of the protocol.

**Loss** is an important parameter in the context of quantum optics since a quantum state cannot be cloned [46] or deterministically amplified without noise. For discrete variable protocols, losses decrease the success probability of the protocol but do not deteriorate the quantum state itself while using a coincidence-basis measurement. Loop-based time-multiplexing protocols are more loss-sensitive since the signal passes the photonic switch repeatedly [10, 13–15]. On the other hand, in continuous-variable protocols the loss is more critical since it deteriorates the purity of the quantum state (eg. the amount of squeezing) [47–49].

**Extinction** is the crosstalk ratio between the on and off states of the switch. In quantum protocols, it determines the error caused by the switching operation when a 100:0 regime of the switch is required. Extinction in general does not represent an issue in quantum protocols, however, it limits some alternative approaches to be applicable in practice [43–45]. Although not commonly needed, ultra-high extinction exceeding 60 dB can be achieved by cascading more Mach-Zehnder interferometers at the expense of higher loss and increased complexity [31–34].

**Multi-level operation**

In a classical sense, by a switch, a two-level (on-off) device is meant. Here, for simplicity, as a photonic switch, we call all devices that can be rapidly reconfigured and have two or more switching levels. Alternatively, the multi-level photonic switch is referred to as a switch, switchable tunable photonic coupler, switchable beam splitter, or high-speed tunable beam splitter. In quantum technology, the multi-level switching feature is crucial, although for some applications two-level switching is sufficient [16–19]. For example, universal quantum computing in the time domain requires a photonic switch with multi-level operation [13]. The number of levels then restricts the dimensionality of the protocol.

**Configuration** means the number of input and output ports. Common configurations are 1×1, 1×2, 2×1, and 2×2. These configurations can operate at high speed in contrast to M×N switches which exist but their speed is typically low. On-off M×N switching can be performed by commercial latching switches or multi-level M×N switch can be produced as an integrated optical device. The speed is, however, restricted to kHz range due to thermal tuning. Generally, fast multi-level 2×2 switches are crucial devices in the context of quantum optics since they act as real-time tunable beam splitters.

## 2.3 Active phase locking

As already mentioned, photonic switches based on phase modulation in a Mach-Zehnder interferometer suffer from environmentally-induced phase drift. While short-term phase fluctuations can be reduced by a passive protection of the interferometer, long-term stability requires active phase locking. Interferometers locked to a specific phase are widely used in many fields of photonics research and technology, such as quantum information processing [28,35], quantum metrology [4, 50, 51], quantum communication [25–27, 52, 53], and tests of fundamental physics [3, 16, 29, 54]. In this section, we will discuss the pros and cons of different approaches to single-photon interferometer stabilization. Further, we will discuss important parameters of phase locking, their

importance in the context of quantum technology, and various approaches to optimize them.

### 2.3.1 Approaches to the active phase locking

Single-photon stabilization methods can be divided into two groups – sequential methods and continuous methods. Sequential methods switch periodically between the phase locking and the quantum processing [28, 55–58]. The advantage of the approach is the simplicity since no auxiliary light is needed. On the other hand, the quantum processing is prolonged due to the phase locking, and, more importantly, sequential stabilization cannot achieve such precision as continuous phase locking. Firstly, sequential methods are slower since the phase is not controlled all the time. Secondly, the phase estimation using a faint single-photon signal is less precise due to limited photon statistics.

Continuous methods are the opposite – more complex and more precise. To provide a continuous phase lock, an auxiliary light acting as a phase reference is injected into the interferometer. The reference can be a strong light, increasing the signal-to-noise ratio and the potential speed of the stabilization. A spatial or spectral mode is typically used to differentiate the signal and the reference. A small path displacement can be used for free-space setups with the main advantage of zero crosstalk between the signal and the reference [29, 35]. The disadvantage is that a long-term phase drift between the signal and the reference may be present since the index of refraction changes locally in time [41]. The wavelength discrimination, suitable for free-space and fiber setups, is more complex since a wavelength (de)multiplexing stage has to be added. On the other hand, this approach is more robust since the signal and the reference propagate the same path [2, 25–27]. To enhance the phase tunability between the signal and the reference, it is possible to multiplex the reference into two modes, such as two orthogonal polarizations [59, 60]. Full tunability was also demonstrated recently by using two frequency-shifted reference beams and heterodyne detection [61].

In special cases, it is possible to achieve continuous phase locking without the need for an external reference [16]. Vedovato et al. employed fast switching in a balanced Mach-Zehnder interferometer to provide a perfect overlap between time bins in their experimental demonstration of a post-selection loophole-free Bell test. Their stabilization method lies in suppressing lateral peaks in a typical time-bin interference pattern (see Fig. 2.2). If the lateral peaks vanish, perfect interference is attained between the short and long time bins, which implies correct phase setting in the Mach-Zehnder interferometer switch.

### 2.3.2 Important parameters of the active phase locking

Optimal phase locking should exhibit excellent phase stability, long-term performance, continuous operation, and minimal crosstalk between the signal and the reference. Since the last two parameters were already addressed in the previous section, here we will focus on the precision of the phase lock and the long-term operation solely.

#### Precision

Precision is an essential parameter of the phase lock. Depending on the application, a different precision is required. Time-bin quantum communication is the least demanding application in terms of phase precision since it operates with zero or $\pi$ phase shifts which are insensitive to the phase error. A few-degree stability is thus satisfying [23]. Photonic switching or interferometric networks using a feedforward require typically improved phase precision since the phase can be switched to arbitrary values [3, 28]. Generally speaking, the phase stability within the range of 0.1-1 degrees is considered as excellent in this context. Such precision leads to 0.09%-0.9% error in the most sensitive point of $\frac{\pi}{2}$. Similar phase stability should be achieved in protocols involving homodyne detection. Homodyne detection is an interferometric measurement method enabling to reconstruct a quantum state in a phase space. Since homodyne detection exploits strong local oscillator and continuous detection, the phase can be locked continuously even without an external reference. Despite of this, homodyne detection with sub-degree phase precision is rare [47–49]. The utmost phase precision is required for loop-based protocols where the error cumulates with each roundtrip. We further investigate the performance of loop-based time multiplexing in Section 5. Our analysis reveals that even a slight relative error of 0.1 degrees can non-negligibly impact the time multiplexing pattern (depending on other parameters). 1-degree error causes significant modulation of the pattern, therefore in general the phase precision should be kept below 0.1 degrees. The phase precision becomes very critical for higher dimensions of the time-bin multiplexing (tens of bins). For example, aiming for 20 balanced time bins, a minimal step of the switched phase is 0.1 degrees for specific parameters (details in Table 5.1). Consequently, the phase error in such cases should be substantially smaller than the minimal step.

#### Long-term operation

Practical operation of an interferometer requires its long-term stability. Although in proof-of-principle tests or fundamental demonstrations this requi-

rement is not necessary, it is helpful to operate a photonic switch or an interferometric network without the necessity of frequent reconfiguration.

In terms of single-photon devices, the long-term stability is achieved only in four works [2,23,41,62], whereas five works demonstrated short-term stability solely [24,25,47,48,63]. Long-term operation requires except of sufficient dynamic range of a phase modulator also a stable phase between the signal and the reference. In terms of spatial displacement between the signal and the reference, the refractive index has to be locally stable which is not usually possible. In dual-wavelength configurations, it is necessary to maintain the spectral stability of the signal and the reference. Further, the phase lock has to be independent of the total intensity of the reference or superior intensity stability has to be provided. If these requirements are not satisfied, the long-term stability is not achieved. One way how to achieve the intensity-independent operation is to monitor the total intensity of the reference and adaptively adjust the setpoint of the phase lock [2]. Secondly, a low-amplitude phase modulation can be applied to the reference. The intensity fluctuations then modify the amplitude of the modulation pattern, therefore the phase lock can be corrected for the intensity fluctuations [26]. Note however that this approach is suitable only for unbalanced Mach-Zehnder interferometers in time-bin quantum communication since the quantum signal is insensitive to the global phase. Specifically, the fourth-order interference, depending only on the phase difference between Alice and Bob, takes part here. Thirdly, heterodyne-detection-based phase lock is also intensity independent since the phase is evaluated from a beat pattern, not the intensity directly [61].

# Chapter 3

# Methods and tools

In this chapter, we describe theoretical concepts, experimental techniques, devices, and measurement techniques crucial for the research presented in this Thesis. These descriptions do not aim to be exhaustive. The theory presented here represents a concise reminder of well-known concepts or specific details not covered in textbooks. In terms of techniques, we aim to give more detailed descriptions than provided in articles. For example, we include practical instructions on how to operate the phase locking using our equipment. This chapter is divided into four sections. Firstly, we introduce a refined model of a Mach-Zehnder interferometer. Secondly, we describe phase locking and phase modulation methods. Thirdly, we briefly address photodetection and signal processing. Finally, we include selected concepts of quantum optics.

## 3.1 Mach-Zehnder interferometer

A Mach-Zehnder interferometer (MZI) is a commonly used interferometric configuration since both interferometer arms are easily accessible. In this section, we delve into detailed analysis of the MZI. Firstly, we summarize the fundamental concepts of coherence theory. After that, we introduce a general model of the MZI, taking into account splitting ratios of beam splitters. Then, we discuss an MZI with two wavelengths. Finally, we provide a specialized analysis of real-world imperfections (referred to as local setup detuning).

### 3.1.1 Interference

An optical signal is an electromagnetic wave described by time-dependent complex amplitude $u(t)$. Optical amplitude is not directly accessible by measurement, but we can measure intensity $I(t)$

$$I(t) = |u(t)|^2. \tag{3.1}$$

Let us assume two copies of the optical signal relatively delayed by a time $\tau$. When perfectly overlapped, the resulting complex amplitude reads

$$u_{\mathrm{OUT}} = K_1 u\left(t+\tau\right) + K_2 u\left(t\right), \tag{3.2}$$

where the coefficients $K_{1,2}$ denote complex amplitude transmittances. A detector measures a mean value of the intensity

$$\langle I_{\mathrm{OUT}} \rangle = \left\langle |K_1 u\left(t+\tau\right) + K_2 u\left(t\right)|^2 \right\rangle, \tag{3.3}$$

which can be rewritten as

$$\langle I_{\mathrm{OUT}} \rangle = |K_1|^2 \left\langle |K_1 u\left(t+\tau\right)|^2 \right\rangle + |K_2|^2 \left\langle |K_1 u\left(t\right)|^2 \right\rangle + 2\mathrm{Re}\left[K_1 K_2^* \left\langle u\left(t+\tau\right) u^*\left(t\right)\right\rangle\right]. \tag{3.4}$$

Let us define a temporal coherence function $\Gamma\left(\tau\right)$ as

$$\Gamma\left(\tau\right) = \left\langle u\left(t+\tau\right) u^*\left(t\right)\right\rangle. \tag{3.5}$$

The temporal coherence function with zero delay is equal to the input intensity

$$\Gamma\left(0\right) = \left\langle |u\left(t\right)|^2 \right\rangle = \left\langle |u\left(t+\tau\right)|^2 \right\rangle = \langle I_{\mathrm{IN}} \rangle. \tag{3.6}$$

assuming stationary processes. It is convenient to normalize the temporal coherence function as follows

$$\gamma\left(\tau\right) = \frac{\Gamma\left(\tau\right)}{\Gamma\left(0\right)} = \frac{\Gamma\left(\tau\right)}{\langle I_{\mathrm{IN}} \rangle}. \tag{3.7}$$

The parameter $\gamma\left(\tau\right)$ is called complex degree of temporal coherence and its absolute value is in the range of 0 to 1. If we rephrase Eq. (3.4) using Eq. (3.7), we get

$$\langle I_{\mathrm{OUT}} \rangle = \langle I_{\mathrm{IN}} \rangle \left( |K_1|^2 + |K_2|^2 + 2\mathrm{Re}\left[K_1 K_2^* \gamma\left(\tau\right)\right] \right). \tag{3.8}$$

Now let us assume the optical signal in a form of

$$u(t) = A(t)\, e^{-i\omega_0 t}, \tag{3.9}$$

where $\omega_0$ is central angular frequency of the optical signal. Then the mean output intensity reads

$$\langle I_{\mathrm{OUT}} \rangle = \langle I_{\mathrm{IN}} \rangle \left[ K_1^2 + K_2^2 + 2K_1 K_2 |\gamma(\tau)| \cos(\omega_0 \tau) \right], \tag{3.10}$$

where we assume $K_{1,2}$ are real. Alternatively, if we omit mean values and rephrase $\langle I_{\mathrm{IN}} \rangle K_{1,2}^2 = I_{1,2}$, we get the well-known interference law

$$I_{\mathrm{OUT}} = I_1 + I_2 + 2\sqrt{I_1 I_2}|\gamma(t)| \cos\varphi, \tag{3.11}$$

where we use phase $\varphi$ defined as $\varphi = \omega_0 \tau$. The first two terms correspond to intensity offset and the third term corresponds to correlation between the original and the delayed optical signal. If we modulate phase, we get cosine modulation of the intensity. We can measure a contrast of the interference pattern, also called visibility. Visibility is defined as

$$V = \frac{I_{\mathrm{MAX}} - I_{\mathrm{MIN}}}{I_{\mathrm{MAX}} + I_{\mathrm{MIN}}}, \tag{3.12}$$

where $I_{\mathrm{MAX}}$ and $I_{\mathrm{MIN}}$ correspond to interference maximum ($\cos\varphi = 1$) and interference minimum ($\cos\varphi = -1$), respectively. It is easy to prove that for balanced interference $I_1 = I_2$ the visibility is equal to the absolute value of the complex degree of temporal coherence $|\gamma(\tau)|$.

For $\tau = 0$ and balanced interference one would expect to always reach maximal visibility ($V = 1$). In practice, this is not true. The optical signal has to perfectly overlap in all possible modes, such as polarization mode, spatial mode, and spectral mode. Reaching perfect visibility under real conditions represents an experimental challenge.

### 3.1.2 General model of an MZI

A general model of an MZI is shown in Fig. 3.1. Incident light with intensity $I_{\mathrm{IN}}$ is split on a beam splitter into two separate paths and overlapped on the second beam splitter. Using Eq. (3.11) together with beam splitter transmittances $T_{1,2}$ and reflectances $R_{1,2}$, the output intensities $I_{\mathrm{OUT}1,2}$ are

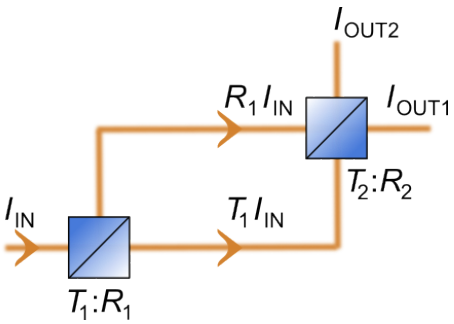


**Figure 3.1:** A generic model of an MZI. Incident light with intensity $I_{\mathrm{IN}}$ is split into two separate paths and overlapped on the second beam splitter. Output intensities $I_{\mathrm{OUT1,2}}$ depend on the phase in the MZI.

$$I_{\mathrm{OUT1}} = \left(R_2T_1 + T_2R_1 + 2\sqrt{T_1T_2R_1R_2}|\gamma(\tau)|\cos\varphi\right) I_{\mathrm{IN}}, \tag{3.13}$$

$$I_{\mathrm{OUT2}} = \left(R_1R_2 + T_1T_2 - 2\sqrt{T_1T_2R_1R_2}|\gamma(\tau)|\cos\varphi\right) I_{\mathrm{IN}}. \tag{3.14}$$

The minus sign in Eq. 3.14 is caused by $\pi$ phase drift by the reflection at the second beam splitter. Using Eqs. (3.12), (3.13), and (3.14), visibilities for output ports are

$$V_1 = \frac{2\sqrt{T_1T_2R_1R_2}|\gamma(\tau)|}{T_1T_2 + R_1R_2}, \tag{3.15}$$

$$V_2 = \frac{2\sqrt{T_1T_2R_1R_2}|\gamma(\tau)|}{R_1T_2 + T_1R_2}. \tag{3.16}$$

From Eqs. 3.15 and 3.16 we can see that the visibility is dependent on the splitting ratios of the beam splitters. The dependence between $T_1$, $T_2$, and corresponding visibilites are plotted in Fig. 3.2. Here we assume $|\gamma(\tau)| = 1$. Note that maximum visibility for one output port is achieved when $T_1 + T_2 = 1$. Perfect visibilities for both output ports require balanced beam splitters $T_{1,2} = 0.5$. Note that this discussion can be extended to different interferometric geometries such as Michelson or Sagnac by choosing $T_1 = T_2$ and $R_1 = R_2$.

Is there a simpler way to mathematically describe MZI output intensities? Rephasing splitting ratios in Eqs. (3.13) with visibility in Eq. (3.15) leads to

$$I_{\mathrm{OUT1}} = V_2\left(1 + V_1\cos\varphi\right) I_{\mathrm{IN}}, \tag{3.17}$$

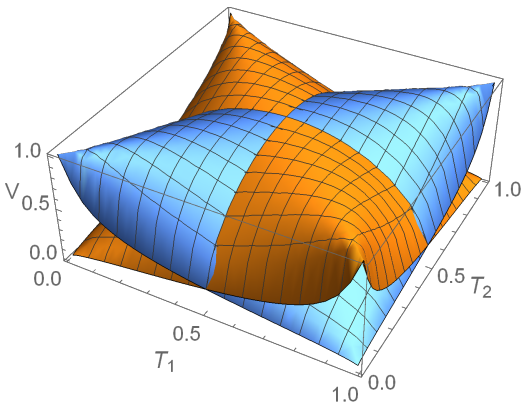


**Figure 3.2:** Maximal visibilities in an MZI depending on transmittances $T_{1,2}$ of beam splitters.

analogically for the second output port

$$I_{\mathrm{OUT2}} = V_1 \left(1 + V_2 \cos\varphi\right) I_{\mathrm{IN}}. \tag{3.18}$$

This is a convenient way to describe MZI output intensities. From these equations, one simply evaluates the MZI phase

$$\varphi = \arccos\left[\frac{\dfrac{I_{\mathrm{OUT1}}}{V_2} - \dfrac{I_{\mathrm{OUT2}}}{V_1}}{I_{\mathrm{OUT1}} + I_{\mathrm{OUT2}}}\right]. \tag{3.19}$$

This equation is beneficial when estimating the phase in an MZI since we have access only to visibilities and output intensities. Typically, we measure the visibilites prior to a phase measurement, and we assume they keep constant. Also, we assume that the measured intensities only depend on the phase in the interferometer. In Section 3.1.4, we will discuss what happens if these assumptions are not satisfied. Before that, let us describe an MZI, where two different wavelengths are propagating.

### 3.1.3 An MZI with two wavelengths

In some cases it is convenient to inject more than one light beam into an MZI. Let us consider to have an MZI with two optical signals, one with the wavelength $\lambda_{\mathrm{s}}$ and the other with the wavelength $\lambda_{\mathrm{r}}$. In this case, each optical

signal interferes with a different phase since

$$\varphi = \omega\tau = 2\pi\frac{\Lambda}{\lambda}, \tag{3.20}$$

where $\Lambda$ is the optical path difference. We can define relative phase between the two wavelengths as follows

$$\varphi_{\mathrm{REL}} = \varphi_{\mathrm{s}} - \varphi_{\mathrm{r}} = 2\pi\left(\frac{\Lambda_{\mathrm{s}}}{\lambda_{\mathrm{s}}} - \frac{\Lambda_{\mathrm{r}}}{\lambda_{\mathrm{r}}}\right). \tag{3.21}$$

By considering different $\Lambda_{\mathrm{r}}$ and $\Lambda_{\mathrm{s}}$, we account for the fact that in a real interferometer, a chromatic dispersion is present.

In general, the relative phase $\varphi_{\mathrm{REL}}$ is not constant but drifts in time. Indeed, the relative phase $\varphi_{\mathrm{REL}}$ drifts when interferometer arms are not locked, thus $\Lambda_{\mathrm{s,r}}$ are drifting. However, even with precisely locked arms, we can observe $\varphi_{\mathrm{REL}}$ fluctuations since it depends also on the wavelength stability. The small drift of relative phase $\Delta\varphi_{\mathrm{REL}}$ can be expressed by applying derivative to Eq. (3.21) resulting in

$$\Delta\varphi_{\mathrm{REL}} = 2\pi\left(\frac{\Lambda_{\mathrm{s}}}{\lambda_{\mathrm{s}}^2}\Delta\lambda_{\mathrm{s}} - \frac{\Lambda_{\mathrm{r}}}{\lambda_{\mathrm{r}}^2}\Delta\lambda_{\mathrm{r}}\right), \tag{3.22}$$

where $\Delta\lambda_{\mathrm{s,r}}$ are small wavelength drifts ($\lambda \gg \Delta\lambda$). One way to eliminate the relative phase drift caused by wavelength fluctuations is to precisely balance the interferometer arms. Then chromatic dispersion should be equal in each arm to achieve $\Lambda_s = \Lambda_r = 0$ for both wavelengths. In practice, interferometers usually have some degree of imbalance, and in some cases, the imbalance is even required. Then, it is beneficial to lock both wavelengths in order to avoid the relative phase drift.

### 3.1.4 Local setup detuning

In Section 3.1.2 we introduced a general model of an MZI. We assumed that the two beam splitters composing the MZI have splitting ratios constant over time. Also, we assumed that the phase can be perfectly evaluated by the knowledge of output intensities and visibilities. Under real conditions, these assumptions are not satisfied perfectly. Here, we will discuss how the phase estimation is affected in this case.

Let us introduce time-dependent losses $\mu_{\mathrm{O}}$ and $\mu_{\mathrm{A}}$ in the MZI as illustrated in Fig. 3.3. Parameter $\mu_{\mathrm{A}}$ describes the case when the first splitting ratio is drifting or the MZI arms are detuning relatively over time. Parameter $\mu_{\mathrm{O}}$

describes the case when output ports are detuned relatively or the detection efficiencies are mutually drifting.

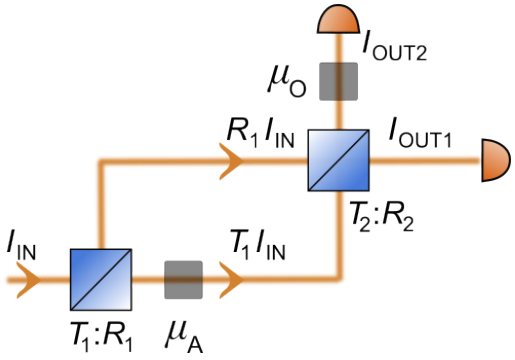


**Figure 3.3:** A detailed model of an MZI with time-dependent losses $\mu_A$ and $\mu_O$. This model simulates a realistic setup suffering from local detuning over time.

Let us first discuss what happens when the parameter $\mu_O$ is present solely. In this case we estimate the phase $\varphi_{EST}$ as follows

$$\varphi_{EST} = \arccos\left[\frac{\frac{I_1}{V_2} - \frac{I_2}{V_1}(1-\mu_O)}{I_1 + I_2(1-\mu_O)}\right]. \tag{3.23}$$

Note that if $\mu_O = 0$, then $\varphi_{EST}$ is equivalent to the real phase $\varphi$ described by Eq. 3.19. However, if $\mu_O \neq 0$, the phase is estimated with an error given as

$$\varphi_{ERR} = \varphi_{EST} - \varphi. \tag{3.24}$$

For example, let us assume that $\mu_O = 1\%$ is introduced. Then, the incorrect phase estimation causes a phase error of 0.3 degrees. Here we assume a high-visibility regime and phase locked close to $\frac{\pi}{2}$. More advanced analysis is plotted in Fig. 3.4. In the high-visibility regime $V_{1,2} = 1$, the phase error is approximately linearly increasing with $\mu_O$ while the slope is decreasing for higher $\varphi$. We get much higher error in the low-visibility regime $V_1 = 0.3$, $V_1 = 0.6$. Now, the curves are not linear, and their slope grows with $\varphi$, oppositely to the high-visibility regime. For 169 degrees, the curve stops below 2% of loss since the phase estimation is out of range of the arccos function.

Secondly, let us consider only parameter $\mu_A$ is introduced in the MZI ($\mu_O = 0$). This case is more tricky because the fluctuations of $\mu_A$ affect except for the intensity in the MZI arms also the visibilities. To describe this effect, it is necessary to express the intensities and visibilities in Eq. 3.19

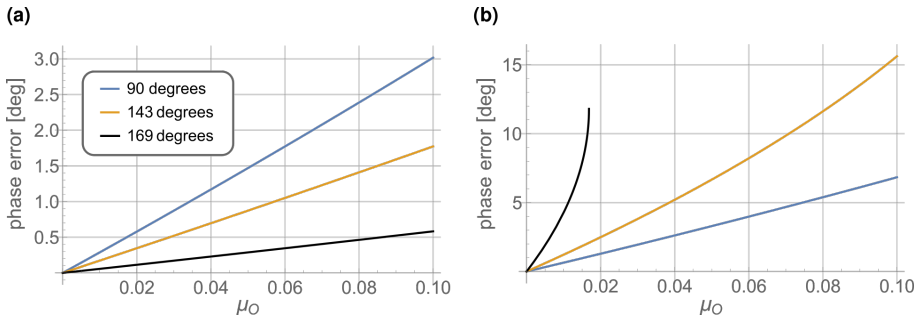


**Figure 3.4:** Impact of $\mu_{\mathrm{O}}$ to the phase estimation. (a) High-visibility regime ($V_{1,2} = 1$). (b) Low-visibility regime ($V_1 = 0.3$, $V_2 = 0.6$).

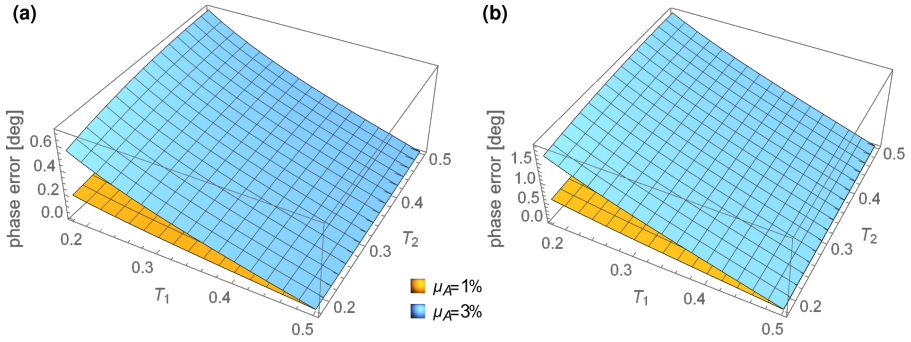


**Figure 3.5:** Impact of $\mu_{\mathrm{A}}$ to the phase estimation. (a) Phase is locked to 90 degrees. (b) Phase is locked to 143 degrees.

using Eqs. (3.13), (3.14), (3.15), and (3.16). Also, let us incorporate $\mu_{\mathrm{A}}$ into the first beam splitter, thus $T_1 \to T_1(1-\mu_{\mathrm{A}})$. Then, the estimated phase reads

$$\varphi_{\mathrm{EST}} = \arccos\left[\frac{a + b\cos\varphi}{2\sqrt{T_1T_2(1-T_1)(1-T_2)}(1-T_1\mu_{\mathrm{A}})}\right], \tag{3.25}$$

where

$$\begin{aligned} a &= T_2(1-T_2)(1-2T_1)\mu_{\mathrm{A}} \\ b &= 2\sqrt{T_1T_2(1-T_1)(1-T_2)(1-\mu_{\mathrm{A}})}, \end{aligned}$$

assuming $|\gamma(\tau)| = 1$. In Fig. 3.5 we plot the phase error $\varphi_{\mathrm{ERR}}$ for two $\mu_{\mathrm{A}}$ depending on $T_1, T_2$. The phase error $\varphi_{\mathrm{ERR}}$ is negligible if $\mu_{\mathrm{A}}$ is small and the first beam splitter is balanced perfectly ($T_1 = 0.5$). Unfortunately, this cannot be always satisfied, especially in dual-wavelength fiber setups, since fiber couplers show a strong dependence on wavelength. Therefore, the splitting ratio typically differs from 50:50 at least for one of the wavelengths.

So far we have not discussed what happens when the second beam splitter splitting ratio is drifting. In this case, we would get the same result as in the previous case since the interference law and the visibilities are symmetric in terms of the first and the second beam splitter.

## 3.2 Phase control

*In the world of quantum dreams,*
*Where light and matter interweave,*
*We strive to lock the photon streams,*
*With precision so supreme.*

*A single-photon Mach-Zehnder phase,*
*Challenged by Poissonian noise and haze,*
*But with dual-wavelengths and reference rays,*
*Our stability sets a new phase.*

Credit: ChatGPT

In this section we will discuss how to actively stabilize a phase in the interferometer and how to modulate the phase as desired. Firstly, we will describe a method of an active phase control enabling to continuously stabilize a single-photon MZI with a high precision. Secondly, we will introduce two methods of fast phase switching using the electro-optic effect.

### 3.2.1 Phase stabilization

To stabilize the phase in the MZI, we use an active feedback loop consisting of ultra-sensitive photodiodes, an analog PID controller, and a fiber stretcher as shown in Fig. 3.6(a). Voltage equivalents of detected intensities are fed into the PID controller. The PID controller evaluates the phase error and applies the corresponding voltage to the fiber stretcher to compensate for the phase error. Here we aim to describe technical details of the feedback loop which are not fully covered in the work [2]. Firstly, we describe in more detail the functionality and the specifications of the PID controller. Also, the tuning procedure of the PID controller is described. Secondly, we provide technical details of the fiber stretcher. Finally, we discuss the potential improvement of the phase lock.

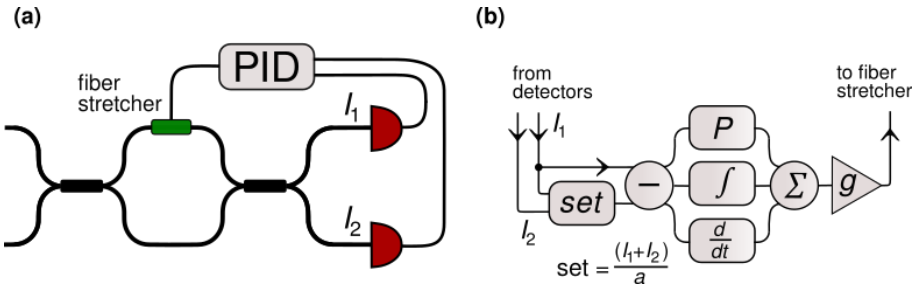


**Figure 3.6:** (a) Active feedback loop consisting of ultra-sensitive photodiodes, an analog PID controller, and a fiber stretcher. (b) Scheme of the PID controller with an adaptive setpoint.

### PID controller

We use an analog PID controller developed as a part of my Bachelor and Master Theses [64, 65]. Further, Michal Dudka assembled two improved versions of the PID controller depicted in Figs 3.7(a,b). The PID controller has improved functionality to satisfy the specific demands of phase locking. Most importantly, it has an adaptive setpoint term enabling the correct operation of the phase lock even with fluctuating intensity. The PID controller is schematically depicted in Fig. 3.6(b). The adaptive setpoint processes voltage equivalents of intensities $I_1, I_2$, and generates a fraction of their sum corresponding to a specific phase. For example, half of their sum corresponds to the middle of the interference fringe ($\frac{\pi}{2}$). Subsequently, the setpoint is subtracted from $I_1$ and the resulting error signal is split among proportional, integral, and derivative terms. While the proportional term simply amplifies the error signal, the integral term operates with low frequencies (up to 10 Hz), and the derivative term responds to high-frequency components of the error signal (kHz). Proportional, integral, and derivative terms are summed, and the resulting signal is after amplification applied to the fiber stretcher.

The PID controller provides excellent tunability. Gain of each of P, I, and D terms and the ending amplifier is fine-tunable by precision 10-turn potentiometers. The gain ranges typically from 0 to 80 or from 0 to 8. Also, cut-off frequencies of I and D terms are discretely adjustable by eight-way switches. The low-pass cut-off frequencies of the I term go from 0.1 Hz up to 230 Hz while the high-pass cut-off frequencies are in the range from 20 Hz up to 60 kHz. The adaptive setpoint is fine-tunable by a precision 10-turn potentiometer as well. In practice, the operating point of the interferometer is tunable with the resolution below 0.01 degrees. Finally, the difference term and the ending amplifier have also adjustable low-pass filers (knobs LOW

G and LOW DIFF). However, we omit them since they turned out to be superfluous.

Let us describe the adaptive setpoint in more detail. To work properly (to provide genuine intensity-independent operation) it is necessary to calibrate first. As a first step, we subtract the detection offsets by knobs OFF1,2. Then we scan interference fringes and observe if the adaptive setpoint is phase-dependent. If so, we provide the phase independence by knob BAL. This knob effectively balances voltages from detectors. The voltages are not typically balanced due to slightly different optical losses in each output.

Now let us describe a tuning procedure of the PID controller. In our approach, we typically tuned the PID controller heuristically to create an intuitive view of the stabilization process. After many trials, we developed an efficient and easy-to-follow procedure:

- set all gains to zero except for global gain
- adjust P, I, D gains following way:
- set P term to 2/3 of the point where the stabilization starts to oscillate
- set I term to lock the phase without an offset
- eventual oscillations compensate via D term

If this procedure is not satisfying, it is possible to play with the capacitances of I and D terms (see SW D and SW I in Fig. 3.7). Currently, we use cut-off frequencies from 0.1 Hz to 230 Hz with the typical setting of 6 Hz cut-off frequency. Firstly, we recommend trying every capacitance level of the I term and choose the one:

1. which is the fastest
2. with minimal tendency to oscillate

Then we recommend trying every D term and choosing the one that gives the system the highest stability and flexibility. Try to introduce fast mechanical vibrations by clapping, hitting the optical table, or similar actions in order to investigate the stability of the system. Perfect stabilization can compensate for dynamic changes without losing the absolute setpoint (the relative phase between the signal and the reference should not change). Using an oscilloscope, it is convenient to zoom voltages corresponding to the setpoint and OUT1 to intuitively evaluate and optimize the phase stability. Although it is possible to use sophisticated methods of PID optimization (measure the stability, evaluate the stability, change PID parameters, repeat the procedure),

we do not recommend such a procedure. It is time-consuming and since the environmental conditions are changing, this procedure often leads to ambiguous results.

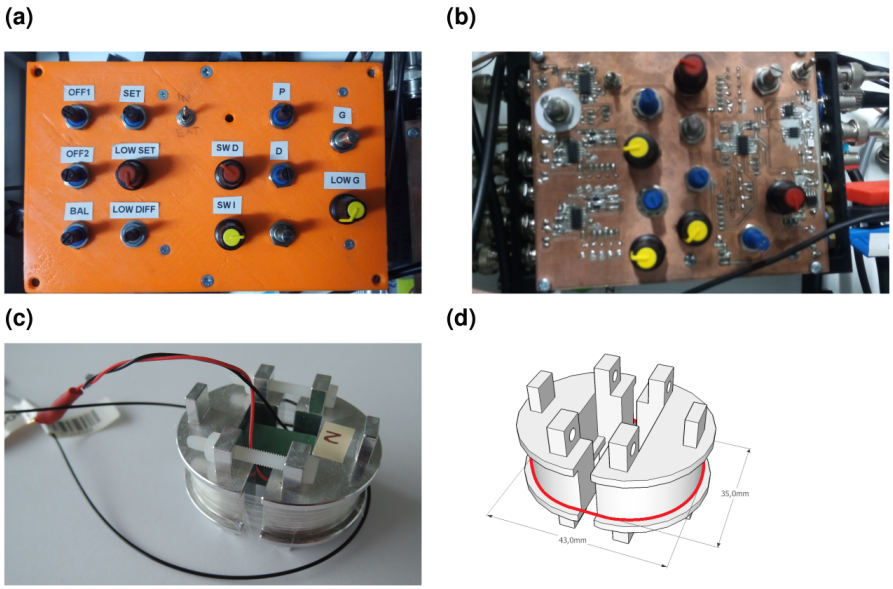


**Figure 3.7:** (a,b) In-house developed PID controllers. (c) Photo of the fiber stretcher (d) 3D model of the fiber stretcher. Panels (c) and (d) are adopted from [66].

### Fiber stretcher

A fiber stretcher is a phase modulator with a high dynamic range and a negligible loss. These properties determine the fiber stretcher as an optimal device for long-term phase drift compensation. We use an in-house developed stretcher developed by Martina Nováková and co-workers. As shown in Fig. 3.7(c), it consists of a 3-m polarization-maintaining fiber coiled around two aluminum segments. The phase modulation is provided by applying a voltage to a piezoelectric crystal placed between the aluminum segments. The phase modulation is proportional to the voltage applied to the piezo crystal. The fiber stretcher has 7.2 $\mu$F capacitance, 1 kHz bandwidth, 20 kHz resonant frequency, 0.11 V half-wave voltage, and dynamic range of $\pm 275$ $\mu$m. Since the extent of the phase drift is much smaller in our case, we use only $\pm 110$ $\mu$m corresponding to the output voltage range of the PID controller ($\pm 30$ V). For further details see work [66], where the fiber stretcher used here is referred to as FS1.

#### Possible improvements of the active feedback loop

Although the current phase locking has superior precision for any practical application, there are still possibilities for improvements. The bandwidth of the active feedback loop is currently limited to 1 kHz by the fiber stretcher. There are two ways to easily increase the bandwidth if needed. Firstly, it is possible to replace the actual fiber stretcher with a stretcher with a flatter response. For example, FS3 from [66] has an almost flat response up to 5 kHz, the dynamic range is smaller by a factor of 2, though. Alternatively, it is possible to split the output voltage from the PID controller between two phase modulators. Specifically, low-frequency components could be applied to the fiber stretcher and the high-frequency components could be sent into the electro-optic modulator.

After these improvements, the effective bandwidth of the feedback loop would be restricted by detectors to 2 kHz (more details about the detection are included in Section 3.3). However, the detectors can be easily replaced by faster ones provided that a stronger source of the reference will be used. Currently, we use a fiber-coupled luminescent diode with additional spectral and polarization filtering. This solution turned out to be very stable in terms of intensity as well as the wavelength, however, it cannot provide more than $\sim 10$ nW at the input. Therefore, the replaced reference source should keep the spectral and intensity stability benefits as well. In practice, there are a few reference sources we have not tried. For example, a spectrally-filtered superlumincent diode could work fine as well.

### 3.2.2 Fast phase switching

Although the response of the fiber stretcher is sufficient for compensating for environmental changes, it cannot perform the fast phase switching required for quantum protocols. Here we will describe an integrated electooptic modulator and a free-space electrooptic modulator both enabling fast phase switching. These devices exploit the non-linear electrooptic (Pockels) effect to modulate the phase. An external electric field applied to crystals that lack inversion symmetry changes linearly the index of refraction of the material. These materials include for example potassium dihydrogen phosphate (KDP), ammonium dihydrogen phosphate (ADP), lithium niobate ($LiNbO_3$), and $\beta$-barium borate (BBO).

Integrated electro-optic modulators are controlled by a low-voltage field which enables ultra-fast response (100 GHz bandwidth is possible) and arbitrarily high repetition rate. Another advantage lies in relatively simple implementation into the setup due to the fiber connectivity. On the other hand,

it suffers from a few dBs of losses, especially due to non-effective coupling between the fiber and the integrated circuit. In the experiments included in this Thesis, we use $LiNbO_3$ integrated phase electro-optic modulator from EOSpace shown in Fig. 3.8 (right). It has a 10 GHz bandwidth, 2.3 dB of loss, half-wave voltage of 2.4 V, and polarization crosstalk of 19 dB.


**Figure 3.8:** Photos of electro-optic modulators for fast switching. On the left side, a free-space phase modulator EM300K-PM-G-AR800 from Leysop is shown. On the right side, an integrated phase modulator PM-0K5-10-PFU-PFU-810-UL from EOSpace is depicted.

In contrast, free-space electro-optic modulators provide very low loss (down to 1%) at the expense of slower response and limited repetition rate. A free-space electro-optic modulator is typically composed of two crystals whose index of refraction of the (slow or fast) axis is controlled by hundreds or thousands of volts. Since the crystals (together with wires and driving electronics) have non-negligible capacitance, the switching response is typically limited to tens of nanoseconds. Also, these devices primarily operate in an on-off regime, although the feasibility of operating them at a few discrete levels has been demonstrated. As an example of this device, in Fig. 3.8 (left) we show a low-voltage phase electro-optic modulator from Leysop. Detailed specifications and comparison between photonic switching methods are included in Section 2.1.

## 3.3 Photodetection and signal processing

In this section, we describe the technical aspects of performed measurements. As shown in Fig. 3.9, a measurement consists of three steps: Light detection, data acquisition, and data processing. Our measurements can be divided into two regimes: a classical regime (a) and a single-photon regime (b). Schematically, they appear similar, but there are major differences in each step.

In the classical regime, the light is detected continuously with photodiodes. The produced electronic signals are converted into a stream of bits by an analog-to-digital converter and processed in a programming language

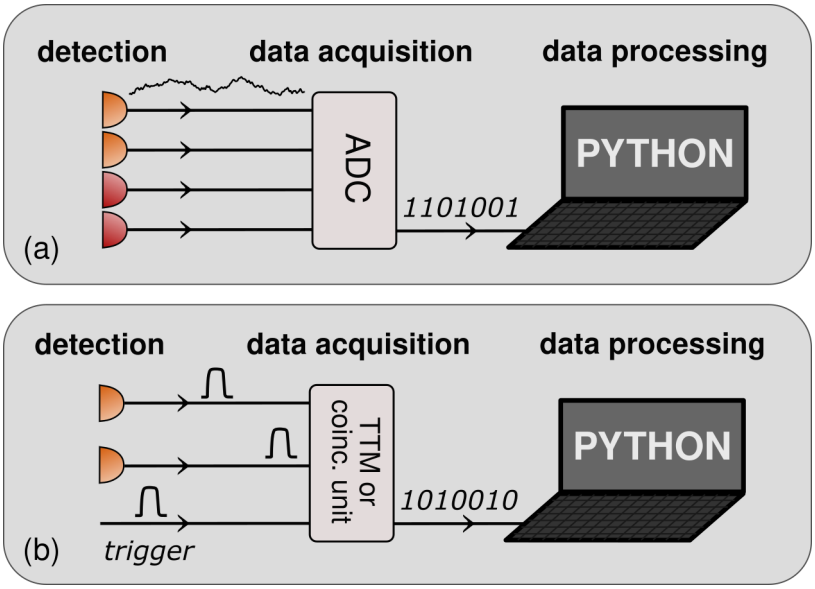


**Figure 3.9:** Building blocks of a measurement in the classical regime (a) the single-photon regime (b). For data acquisition in the classical regime, an analog-to-digital converter (ADC) is used, whereas in the single-photon regime, a time-tagging module (TTM) or a coincidence unit are exploited.

Python. The classical regime was mainly used for phase measurements in work [2]. In other works, it mainly served for auxiliary measurements for adjustments. In the single-photon regime, we use single-photon avalanche diodes to detect photons. Produced electronic pulses are acquired by a time tagger or a coincidence unit. For specific measurements, we add an external trigger to synchronize the detection with the rest of the experiment. The data are evaluated in Python as click statistics, time histograms, or coincidences. Also, additional processing is done depending on the measurement purpose.

Now, let us describe the particular measurement parts. Firstly, a brief description of photodiodes and single-photon avalanche diodes is provided. Further, the evaluation of phase stability in the classical regime is described. Finally, data acquisition and processing in the single-photon regime are illustrated. Here, we mainly focus on time histograms, although the principle of a coincidence-basis measurement is briefly discussed as well.

### 3.3.1 Photodetection

A photodiode is an optical detector based on a PIN structure or a P–N junction. Its operation relies on the interaction of photons with the diode material. When a photon with sufficient energy impinges the diode, it initi-

ates the formation of an electron-hole pair, a phenomenon referred to as the inner photoelectric effect. If this absorption event occurs within the depletion region of the junction or is within a diffusion length away from it, the resulting charge carriers are rapidly separated and propelled away from the junction by the intrinsic electric field of the depletion region. Consequently, the holes migrate towards the anode while the electrons move towards the cathode, generating a photocurrent. Photodiodes may use additional electronic circuits (for example, amplifiers) to produce stronger electronic signal. The parameters of the photodiodes are then dependent on the semiconductor structure as well as the electronics. Below, we sum up the parameters of photodiodes important in the context of this Thesis:

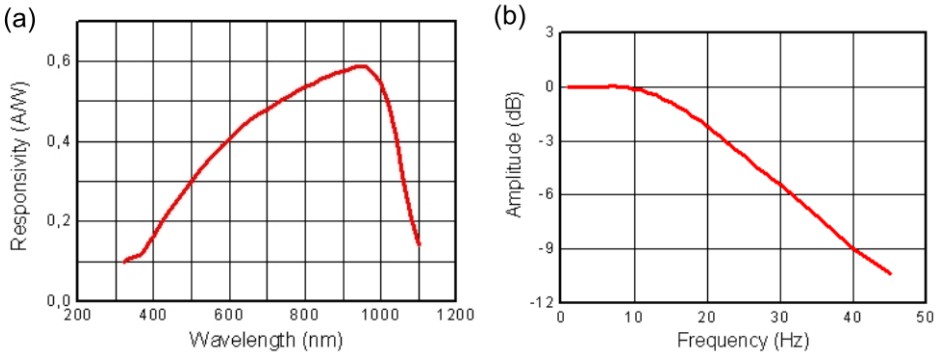


**Figure 3.10:** Examples of responsivity (a) and bandwidth (b) for Thorlabs PDF 10A photodiode. Adopted from manual [67].

- **Responsivity** gives us an information how many photons are converted into electrons producing the photocurrent. It is expressed as ampers of the photocurrent per watt of light (A/W) and it depends on the wavelength of the incident light as shown in Fig. 3.10(a). The higher the responsivity, the more sensitive the photodiode is.
- **Saturation power** gives us an information about the maximum optical power that can be detected. After that the photocurrent does not increase although the optical power is increased.
- **Bandwidth** determines the response time of the detector. As shown in Fig. 3.10(b), the response does not drop to zero immediately. Therefore, we detect even higher frequencies than is the bandwidth but their amplitude drops. Typically, 3 dB bandwidth is characterized: for the cutoff frequency, the amplitude of a detected sine-modulated optical signal drops to half.

| | PWPR-2K-SI | PDF10A |
|---|---|---|
| Responsivity at 810 nm | 0.6 A/W | 0.5 A/W |
| Saturation power | 16 nW | 16 pW |
| Bandwidth | DC – 2 kHz | DC – 20 Hz* |
| Noise-equivalent power (NEP) | 9 fW/$\sqrt{\text{Hz}}$ | 1.4 fW/$\sqrt{\text{Hz}}$ |

**Table 3.1:** Parameters of sensitive photodiodes PWPR-2K-SI from Femto and PDF10A from Thorlabs used for phase locking and measurements in the classical regime.
* 20 Hz (specs.) 30 Hz (measured)

- **Noise-equivalent power** (NEP) gives us an information about a typical noise for a given frequency window. It is counted as a power per square root of bandwidth (W/$\sqrt{\text{Hz}}$). The noise may vary for specific frequencies though it typically follows more or less the response curve. There is often a trade-off between the noise and the response – one way how to suppress a detection noise is to sacrifice the bandwidth.

In our experiments we use photodiodes for three purposes: Firstly, they are helpful for setup adjustments since a strong light can be used and the optical signal is measured instantly (compared to SPADs). Secondly, ultra-sensitive photodiodes can measure optical signals in order of a few millions of photons. In some cases, it is beneficial to measure the signal classically before plugging into SPADs. The advantages are simple processing and immediate signal visibility on oscilloscope. Thirdly, we use sensitive photodiodes to measure the reference light for active phase locking. Surprisingly, we can measure weak optical powers (1 nW) with high signal-to-noise ratio while keeping bandwidth moderate. In Table 3.1 we summarize parameters of sensitive photodiodes we use.

### 3.3.2 SPAD

Single-photon avalanche diodes (SPADs) are composed of a semiconductor with a P-N junction. A reverse bias voltage is applied to the P-N junction. If a photon impinges the diode, an electron is fired from the P-N junction. The free electron is accelerated by the bias voltage, thus it has enough energy to release other electrons. As a result, an avalanche of electrons is produced, making a short electronic pulse. The single-photon avalanche photodiodes are on-off devices – they cannot distinguish how many photons hit the detector as the avalanche is identical for one, two, or more incident photons.

In all experiments, we used single-photon avalanche diodes from Excelitas with the parameters summed up in Table 3.2. A concise explanation of SPAD parameters relevant to us follows.

- **Detection efficiency** determines the probability of a photon detection. It depends on various factors, including optics and electronics. Analogically to a PIN photodiode, the detection efficiency depends on the wavelength of the incident light. It is also worth to mention that the efficiency slightly varies with temperature. This fact is important for measuring MZI phase stability with a single-photon signal since the ambient temperature can drift during the measurement for a couple of Kelvins.

- **Dark counts** determine the detection noise. They are predominantly caused by thermal noise in the photodiode.

- **Dead time** determines the period between avalanche initiation and quenching. During this period, the detector does not react to the incident photons. Dead time also determines the maximum photon rate since for a certain rate, there are no more detection slots available. Before the saturation of the detector, the detection becomes non-linear with the number of photons due to the dead time.

- **Afterpulsing**
  When the avalanche is quenched, there is some probability that a secondary avalanche will be produced. The secondary avalanche is called an afterpulse. While we are interested in photon rate solely, afterpulses can be assumed as an additional noise. However, if we evaluate time histograms, afterpulses can be tricky. For example, we expect single optical pulses, and instead of that, we see two pulses, although the second one is much smaller. Afterpulses significantly differ for each detector, varying from 0.1% to a few percent. Also, it differs with the photon rate. While the detector is saturated or close to the saturation regime, the probability of afterpulses may increase several times.

  Mostly, we were struggling with afterpulses in work [1]. Afterpulses limited the measured extinction for fast MZI switching. When we recognized our problem as afterpulsing, we chose detectors with the lowest afterpulses. Also, we characterized the afterpulses separately and subtracted them from the data to obtain the real shape of the switching.

  Secondly, we had to correct for afterpulses in loop-based time multiplexing since the afterpulsing resulted in four spurious optical pulses delayed by 40 ns from the original ones.

| | typical values |
|---|---|
| detection efficiency at 810 nm | 60 % |
| dark counts | 10-40 per second |
| afterpulse probability | 0.1-1% |
| jitter | 0.3-0.4 ns |
| dead time | 30-40 ns |

**Table 3.2:** Parameters of single-photon avalanche photodiodes from Excellitas.

- **Jitter** is a common parameter in fast electronics. It corresponds to the time uncertainty of the avalanche generation. Although it is not the bandwidth in the classical sense, it determines the time resolution of the detection.

  In the demonstration of sub-ns optical switching [1], detection jitter together with time-tag resolution, bandwidth of the electro-optic modulator, and rise time of the driving pulses determined the rise time of the switching.

### 3.3.3 Data evaluation - phase analysis

There are several approaches how to evaluate phase fluctuations in the interferometer. The most straightforward is to calculate standard deviation

$$\sigma = \sqrt{\frac{1}{N-1}\sum_{i}^{N}\left(x_i - \langle x_i \rangle\right)^2}, \tag{3.26}$$

where $x_i$ are points from the dataset and $N$ is the number of samples. The standard deviation is a perfect uncertainty characteristic if the mean value of the measured quantity does not change in time. However, the mean value of phase typically drifts so to fully characterize phase drift we should evaluate the standard deviation for several acquisition times. Instead of that there are more sophisticated methods to characterize the phase drift.

Firstly, we can evaluate the spectrum of the phase drift by performing Fourier transform

$$\phi\left(f\right) = \int_{-\infty}^{\infty} \varphi\left(t\right) e^{-2i\pi ft} dt. \tag{3.27}$$

Then we compute the square of the absolute value, so we get the spectral

power density of the phase drift

$$G(f) = |\phi(f)|^2. \tag{3.28}$$

In practice, we have discrete data samples measured for a finite interval $T$. This limits the lowest frequency we can evaluate to $1/T$. On the other hand, the data acquisition sampling rate $R$ determines the highest frequency to be $R/2$.

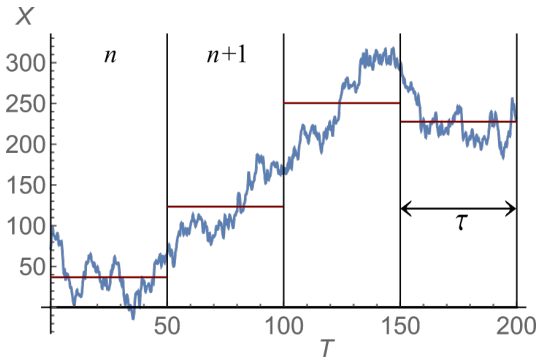


**Figure 3.11:** Data from a measurement accumulated for overall time $T$ are divided into $N$ subsets with identical duration $\tau$. The mean value of $X$ for each subset is evaluated and the mean value of the subset $n$ is subtracted from the mean value of the subset $n+1$. These particular results are squared, summed, and normalized.

An alternative approach to the spectral analysis is the Allan deviation. Basically, it is a root mean square drift depending on the duration of interval $\tau$. For a specific $\tau$ the error is the lowest possible. Therefore, Allan deviation gives a clue how to minimize the measurement error by setting an optimal measurement time [68, 69]. Allan deviation is defined as

$$\sigma_{\mathrm{A}}(\tau) = \sqrt{\frac{1}{2N}\sum_{n=1}^{N-1}\left(\langle X\rangle_{n+1} - \langle X\rangle_n\right)^2}, \tag{3.29}$$

where $\langle X\rangle_n$ is the mean value of the $n$-th subset. A more intuitive explanation is given in Fig. 3.11.

### 3.3.4 Data evaluation in the single-photon regime

As already mentioned, we use single-photon avalanche diodes for the detection and a time tagger or a coincidence unit for data acquisition. The entire process is as follows: when a photon is detected, an electronic pulse is

produced. In time tagger, arrival time of each detection event is recorded with 162 ps resolution. Sometimes we also use an external trigger which serves as a time reference. The time tags are converted to a bit string and evaluated in the programming language Python. There are several ways to process the data. The most simple is a photon rate evaluation which is used if we are interested solely in how many photons came within a specific interval. Time histograms are evaluated when we expect non-uniform photon distribution in time. For example, we expect a train of optical pulses or a specific pattern produced by fast phase switching. Also, we may be interested in coincidences between two or more channels. Although we used mostly data evaluation of single events, two-fold coincidence measurement was done in work [3]. In this section, we briefly discuss the evaluation of single events and coincidence measurements.

The most basic measurement is the acquisition of the photon rate. Here the important task is to set properly the measurement time window. A longer time window contains more photons resulting in lower photon number uncertainty. During measurements, we used an attenuated laser diode as a light source. Since the attenuated laser diode produces a weak coherent state, we get Poissonian photostatistics with uncertainty of $\sqrt{N}$ where $N$ is the number of detection events. For example, if we aim for 1% uncertainty, we need $N = 10000$, thus $\sqrt{N} = 100$ and $\frac{\sqrt{N}}{N} = 0.01$. Indeed, there are additional sources of error such as dark counts and background light. If we characterize these effects beforehand we can subtract them as a constant offset. During most of our measurements, dark counts and background light were negligible compared to the signal, therefore we typically did not perform any correction. Specifically, our typical photon rate was $10^5$ or $10^6$ events per second while the dark count rate including the background light was much below 100 events per second. Afterpulses typically do not represent an issue in photon rate measurements since they form a fixed fraction of the signal. However, afterpulse probability increases for high photon rates (close to the saturation), therefore it is convenient to keep the photon rates far from the saturation. Another reason why to stay far from the saturation is the non-linear response of the detection for a high photon flux. A photon rate measurement can be performed by a time tagger or counting unit. A counting unit brings the advantage of simplified data processing since it does not contain detailed timing information of the detection events.

Now let us describe how time histograms are evaluated. Time histograms are used when we modulate the optical signal thus we expect a specific shape of the optical signal in time. For this measurement, we need to use an external trigger that gives us a temporal reference. The external trigger is locked to

the optical source when optical pulses are used or to the modulation process (for example phase switching). Time tagger produces a stream of time tags for each detector and each trigger. During the data processing, we evaluate the relative delay between each detection event and the nearest preceding trigger. In other words, we will place each detection event in a specific temporal window depending on the delay relative to a trigger event. Then we evaluate a histogram of events in each time window. As in the previous case, we have to accumulate enough data to fit into a given uncertainty (typically chosen as $\leq 1\%$). Also, spurious effects such as dark counts, background light, and afterpulses are present. Compared to the photon rate measurements, time histograms are vulnerable to afterpulses. Specifically, we struggled with the afterpulses in demonstrations of the photonic switching and loop-based temporal multiplexing [1]. Our approach was to identify and subtract the afterpulses from the datasets. In the photonic switching demonstration, we used continuous optical signal, thus photons hit the detectors randomly in time. As a consequence, the afterpulses were overlapping with the optical signal. To identify them, we prolonged the switching time to hundreds of ns, so after switching to 100:0 (almost no photons are coming to a single output), two regions were visible – an afterpulse region and a non-afterpulse region. By subtracting these two regions, we got an estimation of the detection afterpulses. In the case of loop-based temporal multiplexing, we used short optical pulses, thus the afterpulses were temporally separated from the optical signal. As a result, the afterpulses subtraction was straightforward.

Now let us briefly introduce a coincidence measurement. A coincidence occurs if a specific number of photons is detected within a selected time window. A coincidence basis is a convenient tool in quantum optics since it can postselect events only when a protocol succeeds [70]. For example, if we use a two-fold coincidence basis and send a two-photon state through the setup, we ignore all the events when a photon is lost. Therefore, in this case, the two-fold coincidence basis emulates a loss-free setup, although the loss decreases the overall success rate of the protocol. Another benefit of a coincidence measurement is the suppression of detection noise. If the signal is processed only when both detectors click at the same time then random events such as dark counts contribute to the signal only with probability $p_{\mathrm{DARK}}^2$ instead of $p_{\mathrm{DARK}}$. The same happens with other effects such as afterpulses. A coincidence measurement is technically similar to single event measurement but requires a different data processing. Time tag measurement gives us full information about the click statistics but it produces large datasets (giga-terabytes). However, often we do not need to know when a particular coincidence event happened. Then we can simplify data processing by using a coincidence unit. The coincidence unit gives us complete information about

single events and coincidence events within a specific acquisition time, say one second. The coincidence unit can produce small, easy-to-process datasets by sacrificing the precise timing information of particular events.

## 3.4 Selected concepts of quantum optics

In this section, we will introduce the quantum formalism used in this Thesis. Specifically, we will introduce the Fock state basis, a quantum operation performed by a beam splitter, a coherent state, and an analysis of an approximate emulation of a Fock state by a weak coherent state. We expect that the reader has a basic knowledge of a quantum theory, thus the theory presented here is concise. For more detailed and rigorous explanations, we refer the reader to textbooks such as [71].

### 3.4.1 Fock state basis

Fock state basis is a common representation of a photonic quantum state. The Fock state describes how many photons are in a given mode. A quantum state can be described by superposition of Fock states

$$|\psi\rangle = \sum_{n=0}^{\infty} b_n |n\rangle , \tag{3.30}$$

having one-mode state, or for two-mode state

$$|\psi\rangle_{AB} = \sum_{n=0}^{\infty} \sum_{m=0}^{\infty} b_{n,m} |n,m\rangle_{AB} . \tag{3.31}$$

Generalization to multi-mode state is straightforward. Fock states correspond to eigenstates of a quantum harmonic oscillator. Conversion between Fock states is provided with annihilation operator $\hat{a}$ and creation operator $\hat{a}^\dagger$

$$\hat{a}^\dagger |n\rangle = \sqrt{n+1} |n+1\rangle , \tag{3.32}$$

$$\hat{a} |n\rangle = \sqrt{n} |n-1\rangle . \tag{3.33}$$

Application of the annihilation operator corresponds to photon subtraction, whereas the creation operator performs a photon addition. These operators

are valuable tools for quantum computations since every Fock state can be expressed as a product of creation operators applied to a vacuum state

$$|n\rangle = \frac{\hat{a}^{\dagger\, n}}{\sqrt{n!}} |0\rangle \,. \tag{3.34}$$

Then, the propagation through a linear optical network is equivalent to a unitary operation applied to the creation operators. This fact can be mathematically expressed as

$$\hat{U} f\left(\hat{a}^\dagger\right) |0\rangle = \hat{U} f\left(\hat{a}^\dagger\right) \hat{U}^\dagger \hat{U} |0\rangle = f\left(\hat{U}\hat{a}^\dagger\hat{U}^\dagger\right) |0\rangle \,, \tag{3.35}$$

where $\hat{U}$ stands for a unitary operator. Here, we used $\hat{U}|0\rangle = |0\rangle$, which is valid for linear optics. However, it cannot be generalized to all optical systems. For example, quadrature squeezing of a vacuum state does not satisfy this equality.

### 3.4.2 Beam splitter

A beam splitter is a crucial component in quantum optics since it enables coupling between two modes. Further, it is a key component for implementing an approximate photon subtraction, equivalent to applying the annihilation operator. Also, a lossy channel or non-efficient detection can be simulated by a beam splitter. A creation operator is transformed by a beam splitter as follows

$$\hat{a}^\dagger_{\mathrm{A}} \overset{\mathrm{BS}}{\to} t\hat{a}^\dagger_{\mathrm{C}} + r\hat{a}^\dagger_{D}, \tag{3.36}$$

$$\hat{a}^\dagger_{\mathrm{B}} \overset{\mathrm{BS}}{\to} -r\hat{a}^\dagger_{\mathrm{C}} + t\hat{a}^\dagger_{\mathrm{D}}, \tag{3.37}$$

where $t$ and $r$ ($r^2 + t^2 = 1$) are amplitude transmittance and amplitude reflectance, respectively. Using Eqs. (3.34), (3.36), and (3.37), one-photon state is split on a beam splitter as follows

$$|1,0\rangle_{\mathrm{AB}} = \hat{a}^\dagger_{\mathrm{A}} |0,0\rangle_{\mathrm{AB}} \overset{\mathrm{BS}}{\to} t\,|1,0\rangle_{\mathrm{CD}} + r\,|0,1\rangle_{\mathrm{CD}} \,, \tag{3.38}$$

$$|0,1\rangle_{\mathrm{AB}} = \hat{a}^\dagger_{\mathrm{B}} |0,0\rangle_{\mathrm{AB}} \overset{\mathrm{BS}}{\to} -r\,|1,0\rangle_{\mathrm{CD}} + t\,|0,1\rangle_{\mathrm{CD}} \,. \tag{3.39}$$

Analogically, for a Fock state injected in a single port of the beam splitter, the output state reads

$$|n,0\rangle \overset{\mathrm{BS}}{\to} \sum_{k=0}^{n} \sqrt{\binom{n}{k}} t^{n-k}\, r^k\, |n-k,\, k\rangle \quad . \tag{3.40}$$

### 3.4.3 Coherent state

A coherent state is a quantum representation of light with a Poissonian photon number statistics

$$|\alpha\rangle = \exp\left(-\frac{|\alpha|^2}{2}\right) \sum_{n=0}^{\infty} \frac{\alpha^n}{\sqrt{n!}} |n\rangle \,. \tag{3.41}$$

An approximate coherent state can be generated with an attenuated laser. A coherent state is an eigenstate of annihilation operator $\hat{a}\,|\alpha\rangle = \alpha\,|\alpha\rangle$. Thus, a coherent state propagating a lossy channel is transformed to a coherent state with a smaller mean photon number. It is very practical in experiments since losses can be simply compensated by increasing the laser power. Indeed, the coherent state cannot be used for every quantum protocol since it does not exhibit all aspects of non-classical behaviour.

Genuine non-classical behavior requires non-classical sources such as Fock state $|n\rangle$. However, the preparation of a Fock state is demanding, even in the case of a single-photon state. Although promising sources such as quantum dots exist, the quality of produced states is rather limited [72, 73]. A conventional single-photon preparation exploits non-linear effects, specifically spontaneous parametric down-conversion (SPDC). A pump photon is converted into a photon pair with some probability. Detection of one photon from the pair heralds the presence of the second photon [17–20]. The main disadvantages of this approach lie in the experimental complexity (although on-chip devices exist) and the low probability of photon pair generation. In the case of multi-photon preparation, the situation is even more complicated. Additionally, due to losses and limited detection efficiency, we get a mixture of Fock states instead of the pure state.

Luckily, we can overcome the loss and detection efficiency issues by using a coincidence basis. Thus, we only postselect the cases where the multi-photon state was detected. In this case, it is possible to emulate a genuine multi-photon state by a weak coherent state (but not for every protocol). Indeed, we need to perfectly resolve a photon number since the coherent state contains all $n$-photon states. Practically, a genuine photon number resolving detection does not exist, thus a strongly attenuated coherent state has to be used. Specifically, undesired multi-photon contributions have to rapidly drop to zero.

### 3.4.4 Post-selected Fock state from a weak coherent state

In the experiment [3], we used this approach to emulate a two-photon state. Let us describe how to optimally set parameters to balance the generation rate and the error caused by undesired multi-photon contributions. We used a setup where the optical signal is split between two single-photon detectors. For simplicity, let us assume that the detection efficiency is the same for both detectors, and it is incorporated in the overall transmittance of the setup.

Now, we are interested when we correctly assign a two-fold coincidence to a two-photon state and when the coincidence is confused with a three-photon state. For simplicity, let us ignore higher photon numbers. A two-photon state is split into two single-photon states, causing a two-fold coincidence in 50% cases. A three-photon state has more possibilities how to split

$$|3,0\rangle \rightarrow \sqrt{\frac{1}{8}}\,|3,0\rangle + \sqrt{\frac{3}{8}}\,|2,1\rangle + \sqrt{\frac{3}{8}}\,|1,2\rangle + \sqrt{\frac{1}{8}}\,|0,3\rangle\,. \tag{3.42}$$

In 75% of cases, a two-photon state impinges one detector, and a one-photon state hits the other detector, causing a spurious two-fold coincidence. Now, we should also consider that there is a finite detection efficiency. The coincidence arising from two-photon state is detected with probability $p_{2\mathrm{D}} = \mu^2$ while the coincidence caused by three-photon state is detected with $p_{3\mathrm{D}} = \mu\left[1-(1-\mu)^2\right]$ probability.

Now, we would like to characterize a relative error caused by spurious coincidences arising from the three-photon state.

$$p_{\mathrm{error}} = \frac{75\%}{50\%}\frac{p_{3\mathrm{D}}}{p_{2\mathrm{D}}}\frac{p_3}{p_2} \tag{3.43}$$

where $p_i$ is the probability of $n$-photon state. From this equation, it is easy to compute the ratio between three-photon and two-photon states for a given error. For example, in work [3], we use SPADs at 810 nm with $\mu \approx 0.6$. If we aim for the relative error of 1% or lower, then $\frac{p_3}{p_2} \leq 0.5\%$. From this condition, we can compute the appropriate coherent state. However, in the experiment, we do not have direct access to the full photostatistics, therefore we cannot completely reconstruct the coherent state. So, what is the simplest approach to set an appropriate power for the laser?

Firstly, it is possible to do a similar analysis for a one-photon state since in a two-fold coincidence measurement, we have also access to single-photon events. Alternatively, if having a more complex detection system, it is possible to evaluate three-fold coincidences and estimate $p_3$ from this knowledge. We

chose this approach in work [3]. So far, we neglected four-photon and higher-photon states. It is possible only when the coherent state is weak enough.

If we use the parameters from the example above, thus $\frac{p_3}{p_2} = 0.5\%$, then the corresponding coherent state has the photostatistics of $p_1 = 1.5 \times 10^{-2}$, $p_2 = 1.1 \times 10^{-4}$, $p_3 = 5.5 \times 10^{-7}$, and $p_4 = 2.1 \times 10^{-9}$. We can see that most of the time, there is no photon produced. Sometimes, a photon is produced but does not contribute to the two-fold coincidence signal. Only in 1 of 10000 cases we detect the desired two-photon state. Thus, even if we use a pulsed source with a 10 MHz repetition rate, the bi-photon is produced only with a kHz rate. Also, notice that the four-photon state occurs with the probability of only $10^{-9}$, thus it can be neglected in this analysis.

# Chapter 4

# Active phase locking

In this chapter, we present experimental research in active phase stabilization of single-photon interferometers published as work [2]. Although the active phase locking is briefly mentioned also in works [1, 3], this article presents the most advanced version of the active stabilization. We aimed to achieve the best possible stability with an emphasis on long-term operation. The significant improvement of the stability compared to the previous works lies in recognizing and reducing effects that had not been described yet, to the best of our knowledge. These are specifically phase estimation errors caused by local setup detuning. Also, stable total intensity and spectral stability of sources were crucial to reach long-term precision. The article contains a complete description of all techniques, theory, results, and comparisons with other approaches. We further extend the theory in Section 3.1. For a more detailed description of the active feedback loop, specifically the PID controller, see Section 3.2.1. A resume of the article follows, the full article is enclosed below.

Single-photon interferometers locked to a specific phase are widely used in many fields of photonics research and technology, such as quantum information processing [28, 35], quantum metrology [4, 50, 51], quantum communication [25–27, 52, 53], and tests of fundamental physics [3, 16, 29]. Phase locking at a single-photon level is demanding, though, and the speed and precision are limited due to the shot noise of the detected photons. These limitations can be overcome by employing an auxiliary light acting as a phase reference. This approach enables continuous stabilization with high precision, operating independently of the quantum signal. To address the signal and the reference individually, they must differ in a selected parameter, such as the wavelength.

Here, we demonstrate continuous sub-0.1 degree phase locking of a single-photon Mach-Zehnder interferometer (MZI) in the dual-wavelength configu-

ration. To lock the phase, we use spectrally stable 1.5 nW reference light adaptively corrected for intensity fluctuations, and as a result, we reach exceptional phase stability of 0.05 degrees for 15 hours demonstrated for the signal.

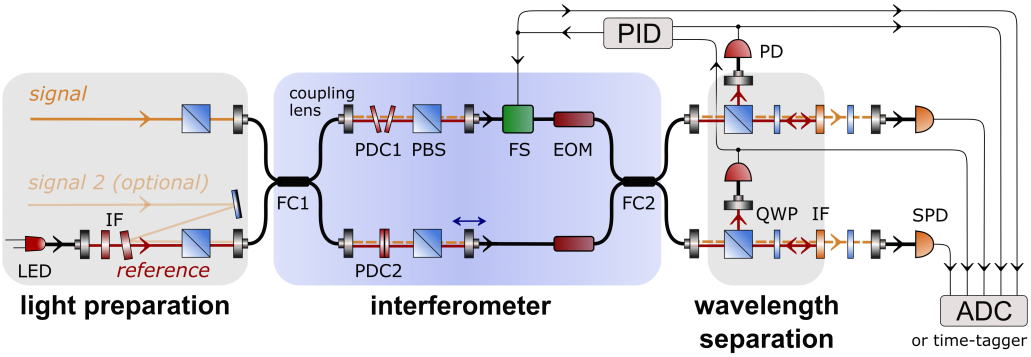


**Figure 4.1:** Experimental setup for an interferometer with active phase locking. The signal and the reference are injected into the interferometer and co-propagate through 8 m of fibers and 0.5 m of free space in each arm. The interferometer is assembled to maximize interference visibility for a broad spectrum and simultaneously provide fast phase switching. At the interferometer outputs, the signal and the reference are separated and detected. The detected reference is processed by a PID controller, and consequently, the phase is locked via a fiber stretcher. Legend: light-emitting diode (LED), interference filter (IF), polarizing beam splitter (PBS), fiber coupler (FC), phase dispersion compensator (PDC), fiber stretcher (FS), electro-optic phase modulator (EOM), quarter-wave plate (QWP), photodiode (PD), sensitive photodiode or single-photon detector (SPD), proportional-integral-derivative controller (PID), analog-to-digital convertor (ADC).

The phase lock is carried out by an active feedback loop consisting of a detector, a proportional-integral-derivative (PID) controller, and a phase modulator. The principle is the following: A phase fluctuation is imprinted to the detected light as an intensity fluctuation. Subsequently, the produced electronic signal is evaluated by the PID controller, and an appropriate voltage is fed into the phase modulator in order to compensate for the initial phase fluctuation. The precision and speed of this approach depend on noise, frequency response, and dynamic range of the feedback loop. However, maintaining high phase precision in the long term also requires the optimization of the optical part of the setup. Firstly, it is necessary to avoid relative phase drift between the signal and the reference, which implies their perfect spectral stability. Secondly, the phase lock has to be immune to fluctuations of the reference intensity. To achieve this feature, we adaptively adjust the phase-locking setpoint to follow the intensity fluctuations. However, there is

another deteriorating effect, which we refer to as local setup detuning (for detailed description see Section 3.1.4). If intensity drops only in one arm (or output) of the interferometer, the phase estimation of the reference becomes biased since the intensity decrease is indistinguishable from phase drift in this case. Consequently, we observe *relative phase drift* between the signal and the reference. In this work, we aimed to reduce all these undesired effects and optimize the control electronics in order to achieve the best possible phase-locking performance.

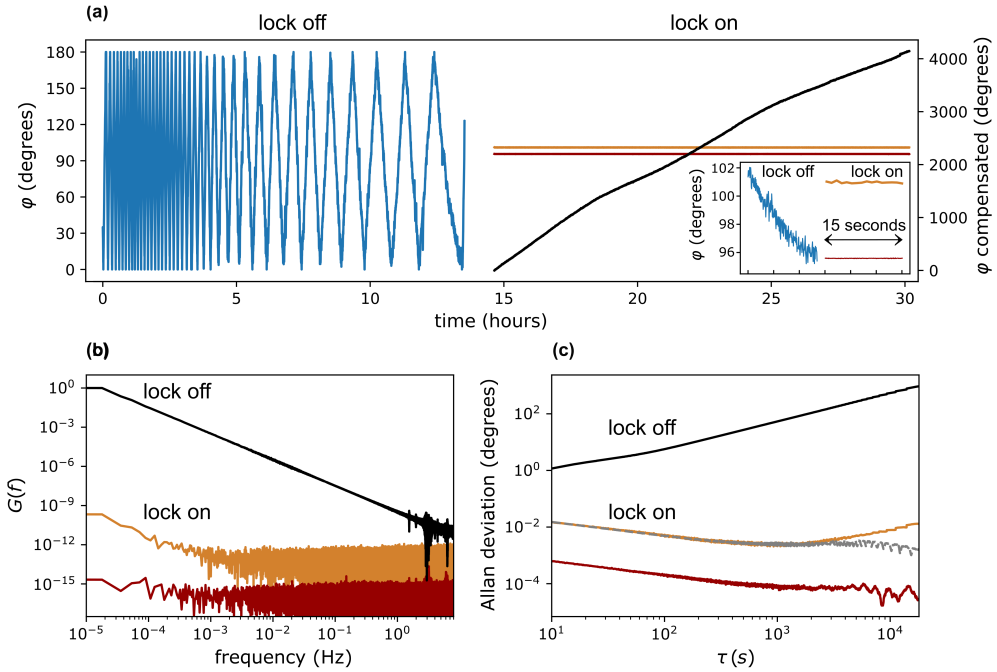


**Figure 4.2:** Comparison of stabilized and non-stabilized MZI. In stabilized MZI, the reference and the signal are represented by the red line and the orange line, respectively. (a) Stability in the time domain. The blue line represents the phase in non-stabilized MZI and the black line corresponds to the phase drift compensated during the phase locking (see the right vertical axis). The inset shows the stability in the short term. (b) Spectral power density $G$ of the phase noise. (c) Allan deviation of the phase noise. The gray line illustrates the noise level of the signal acquisition.

The experimental setup is depicted in Fig. 4.1. To achieve intensity and spectrally stable sources, we use fiber-coupled light-emitting diodes with additional spectral and polarization filtering. The signal and the reference are merged and co-propagate through the MZI. We can tune a relative phase between the signal and the reference, allowing us to lock the phase to the most

stable point of $\frac{\pi}{2}$ while operating the signal at an arbitrary phase. To achieve this ability, we developed a component called phase dispersion compensator. The element enables for slight tuning of dispersion in the setup by contra-directional tilting of two high-dispersion glass plates. At each MZI output, the wavelengths are demultiplexed via a dichroic optical isolator assembled from a polarizing beam splitter, a quarter-wave plate, and an interference filter. We reach negligible crosstalk of 30 photons/s from the reference to the signal, equivalent to extinction better than 80 dB. To reduce air flux and temperature instabilities, we cover the whole setup with styrofoam plates during all measurements. The main benefit of the passive protection is in suppressing the local setup detuning.

The active phase lock is carried out by a feedback loop composed of the photodiodes, PID controller, and a fiber stretcher. The reference with the power of 1.5 nW impinges silicon photodiodes with NEP=9 fW/$\sqrt{\text{Hz}}$ and 2 kHz bandwidth. The resulting electronic signals are processed by an in-house developed analog PID controller. Compared to a conventional PID controller, the circuit is provided with an adaptive setpoint, which corresponds to the correct phase regardless of the intensity fluctuations of the reference. The PID controller is fine-tunable in each parameter via 10-turn precision potentiometers. As a result, the target phase is set with high accuracy. To provide correct phase estimation for the adaptive setpoint, we include additional tunability to cancel out detection offsets and to balance detection efficiencies. The PID controller is designed to drive a custom-made fiber stretcher with 7.2 $\mu$F capacitance, 1 kHz bandwidth, a half-wave voltage of 0.11 V, and a dynamic range of $\pm$275 $\mu$m [66].

Now, let us present the results of the phase stability. We compare the performance of the MZI with and without the active stabilization and present the phase stability in three ways: in the time domain, in the frequency domain, and via the Allan deviation. The results in the time domain are depicted in Fig. 4.2(a). Typical phase drift of non-stabilized MZI is shown on the left side. On the right side, we show phase noise for stabilized MZI (orange and red lines) and the phase compensated during the stabilization process (black line). The inset represents a detailed view of the phase noise. While the phase lock is active, a phase drift of 4000 degrees per 15 hours is virtually eliminated. In terms of standard deviation accumulated over a typical single-photon sampling frequency of 1 Hz, we reach 0.05 degrees for the signal and 0.002 degrees for the reference within a 15-hour interval.

Further, we analyze the spectral power density of the phase noise shown in Fig. 4.2(b). During the stabilization process, the phase noise is suppressed by 9 orders of magnitude for frequencies in the range $10^{-3}$ to $10^{-5}$ Hz. For frequencies above $10^{-3}$ Hz, the phase noise is primarily given by detection

noise. Furthermore, we evaluate the Allan deviation of the phase noise depicted in Fig. 4.2(c). For the signal, we reach Allan deviation below $2 \times 10^{-2}$ degrees for time intervals from 10 s to more than 5 hours. The minimum value $2 \times 10^{-3}$ degrees is achieved for $10^3$ s. Allan deviation of the reference is evaluated to be smaller than $10^{-3}$ degrees.

In summary, we have implemented a novel technique of continuous phase locking for single-photon circuits and networks. We have experimentally demonstrated phase locking of 8.5 m long fiber-based MZI with a phase standard deviation of 0.05 degrees maintained over 15 hours. To the best of our knowledge, our results represent the most precise phase locking within single-photon interferometers. Since our method can be implemented in a vast majority of interferometric networks, it can significantly improve the performance of many phase-sensitive applications in information processing, quantum metrology, and quantum communication.

Research Article | Vol. 31, No. 8 / 10 Apr 2023 / Optics Express 12562
Optics EXPRESS

# Sub-0.1 degree phase locking of a single-photon interferometer

VOJTĚCH ŠVARC,* MARTINA NOVÁKOVÁ, MICHAL DUDKA, AND MIROSLAV JEŽEK

*Department of Optics, Faculty of Science, Palacký University, 17. listopadu 12, 77146 Olomouc, Czech Republic*
*svarc@optics.upol.cz

**Abstract:** We report a single-photon Mach-Zehnder interferometer stabilized to a phase precision of 0.05 degrees over 15 hours. To lock the phase, we employ an auxiliary reference light at a different wavelength than the quantum signal. The developed phase locking operates continuously, with negligible crosstalk, and for an arbitrary phase of the quantum signal. Moreover, its performance is independent of intensity fluctuations of the reference. Since the presented method can be used in a vast majority of quantum interferometric networks it can significantly improve phase-sensitive applications in quantum communication and quantum metrology.



## 1. Introduction

Interferometers locked to a specific phase are widely used in many fields of photonics research and technology, such as quantum information processing [1,2], quantum metrology [3–5], quantum communication [6–10], and tests of fundamental physics [11–13]. In these applications, precise phase control of single-photon interferometers and photonic routers is crucial [8,12,14]. For instance, the phase stability determines the amount of quadrature squeezing required for protocols in quantum metrology [15,16]. In quantum cryptography and quantum communication, phase instabilities increase the bit error rate, which deteriorates the speed and security [17]. Generally, sub-degree stability is considered to be sufficient for most applications except for ultra-sensitive ones such as loop-based protocols where the phase error cumulates each roundtrip [14,18,19].

Although in classical interferometry, the sub-degree phase stabilization is feasible, at the single-photon level it is extremely challenging due to Poissonian photodetection noise. As a consequence, the typical precision of single-photon phase locking is a few degrees, and the response is slower than 0.1 s [17,20]. An efficient strategy to overcome the photodetection noise is to lock the phase via a bright reference light co-propagating with the signal photons. To address the signal and the reference individually, they must differ in a selected parameter. The universal approach, suitable for both free-space and fiber setups, is to differentiate the signal and the reference by wavelength [6,8,9]. An alternative approach, suitable for free-space setups only, is to add a small transversal displacement between the signal and the reference beams [1,11].

Optimal phase locking should possess the following features: excellent phase stability, long-term performance, continuous operation, and minimal crosstalk between the signal and the reference. Most of the works in the field of single-photon interferometer phase locking did not satisfy more than two of these requirements [6,15,17,20–22]. Specifically, most of them are limited to short-term operation and few-degree stability. Two works demonstrated continuous operation, reasonably low crosstalk, and 0.2-degree stability in the short term [8] or a 4-degree stability in the long term [23]. However, achieving all of the desired features simultaneously has not been reported so far.

Here we demonstrate continuous sub-0.1 degree phase locking of a single-photon Mach-Zehnder interferometer (MZI) in the dual-wavelength configuration. To lock the phase, we use spectrally stable 1.5 nW reference light adaptively corrected for intensity fluctuations, and as

#480569 https://doi.org/10.1364/OE.480569
Journal © 2023 Received 9 Dec 2022; revised 17 Mar 2023; accepted 19 Mar 2023; published 31 Mar 2023

Optics EXPRESS

a result, we reach exceptional phase stability of 0.05 degrees for 15 hours demonstrated for the signal. Moreover, using integrated electro-optic modulators embedded in MZI, we achieve sub-ns phase switching. The single-photon signal is virtually free of crosstalk from the reference and exhibits visibility of 99.6% for 3 nm spectral width, enabling short-pulse operation. These properties make our approach directly applicable in many quantum protocols requiring fast photonic routing or low-latency feedforward operation [13,14]. Furthermore, the presented phase stabilization can facilitate demanding loop-based protocols [14,18,19,24,25] and enable ultra-stable operation of time-bin quantum communication protocols [6–8,12].

## 2. Methods

The phase lock is commonly carried out by an active feedback loop consisting of a detector, a proportional-integral-derivative (PID) controller, and a phase modulator. The principle is following: A phase fluctuation is imprinted to the detected light as an intensity fluctuation. Subsequently, the produced electronic signal is evaluated by the PID controller, and an appropriate voltage is fed into the phase modulator in order to compensate for the initial phase fluctuation. The precision and speed of this approach depend on noise, frequency response, and dynamic range of the feedback loop. However, there are additional challenges one has to count on. In this section, we will focus on intensity and wavelength-related issues and ways how to suppress them. Although these issues are not commonly addressed, they can significantly limit the performance of the active feedback loop, especially while aiming at long-term sub-degree stability.

Conventionally, the PID controller evaluates the actual phase error by comparing the intensity detected at a single interferometer output with a constant setpoint. However, as depicted in Fig. 1(a), this solution cannot distinguish between intensity and phase fluctuations. Therefore the setpoint does not correspond to the desired phase if the intensity of the reference fluctuates. This issue can be overcome by evaluating the setpoint using the actual intensity of the reference. As shown in Fig. 1(b), this is possible by monitoring both interferometer outputs, summing their outcomes, and using a fraction of the sum as the setpoint. Apart from suppressing the influence of intensity fluctuations, this adaptive setpoint improves the signal-to-noise ratio (SNR) by a factor of 2 since two independent noisy detectors are averaged.

Although the adaptive setpoint eliminates efficiently the total intensity changes, it does not sufficiently respond to local intensity fluctuations caused by an asymmetric misalignment of the setup (e.g. detuning in a single arm). This effect, which we call local setup detuning (LSD), is typically much weaker than the total intensity drift, but it is harder to determine and correct for. LSD spoils the phase estimation, which consequently leads to a phase error since the setpoint no longer corresponds to the desired phase. We divide LSD into two types described by parameters $\mu_O$ and $\mu_A$ as illustrated in Fig. 1(c).

The first type of LSD is relative detuning between interferometer outputs which is equivalent to a time-dependent loss $\mu_O$ at a single output port. The phase estimation $\varphi_{EST}$ using output intensities $I_1$ and $I_2$ is described as

$$\varphi_{EST} = \arccos\left[\frac{\frac{I_1}{V_2} - \frac{I_2}{V_1}(1-\mu_O)}{I_1 + I_2(1-\mu_O)}\right], \tag{1}$$

where $V_1$ and $V_2$ are visibilities at the corresponding output ports. If $\mu_O = 0$, $\varphi_{EST}$ is equivalent to the real phase $\varphi$. However, if $\mu_O \neq 0$, the phase is estimated with an error given as $\varphi_{EST} - \varphi$. For example, let us assume that $\mu_O = 1\%$ is introduced in the reference. Then the incorrect phase estimation causes a phase error of 0.3 degrees. Here we assume a high-visibility regime and phase locked close to $\frac{\pi}{2}$ (parameters relevant to our setup). This example illustrates that even small detuning would cause non-negligible phase error.

Optics EXPRESS

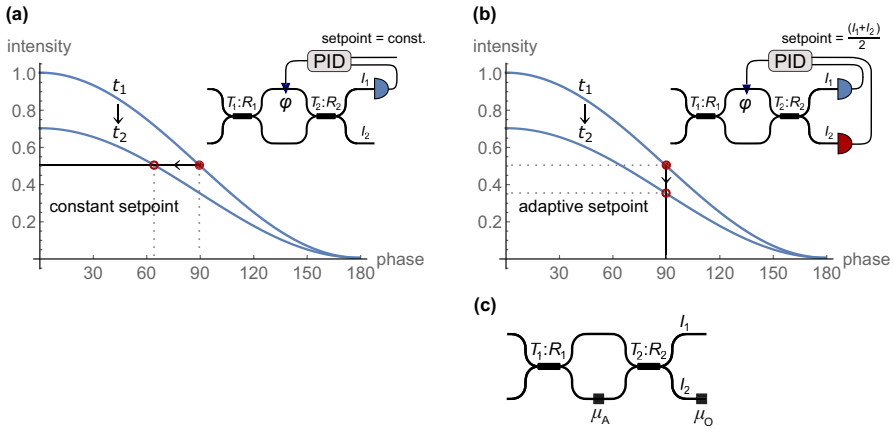


**Fig. 1.** Phase locking with (a) constant setpoint and (b) adaptive setpoint. Phase versus intensity (interference fringe) is plotted for time $t_1$ and $t_2$. The phase is set to 90 degrees in $t_1$, and then in $t_2$, the total intensity decreases. (a) If the phase is locked using one detector and a constant setpoint, the phase lock cannot distinguish between intensity and phase drift. Consequently, decreased intensity in $t_2$ leads to a phase locking error. (b) By detecting both outputs, the setpoint can be adaptively corrected for the intensity fluctuations. Therefore, the phase is kept constant despite decreased intensity in $t_2$. (c) An extended model of MZI including LSD parameters $\mu_O$ and $\mu_A$.

The second type of LSD is described by detuning of a single arm in the interferometer, equivalent to time-dependent loss $\mu_A$, which impacts the visibility and intensity distribution between the outputs. As a consequence, the phase estimation is biased since we have no access to the actual visibility during the stabilization process. To describe this effect, it is necessary to express the intensities and visibilities in Eq. (1) using transmittances $T_1$ and $T_2$ of beam splitters employed. For simplicity, let us assume perfect coherence and $\mu_O = 0$. Then the corresponding equation for the estimated phase in MZI reads

$$\varphi_{EST} = \arccos\left[\frac{T_2(1-T_2)(1-2T_1)\mu_A + 2\sqrt{T_1T_2(1-T_1)(1-T_2)(1-\mu_A)}\cos\varphi}{2\sqrt{T_1T_2(1-T_1)(1-T_2)}(1-T_1\mu_A)}\right]. \quad (2)$$

From this analysis, the phase estimation error is negligible if $\mu_A$ is small (less then 10%) and the first beam splitter is balanced perfectly ($T_1 = 0.5$). Unfortunately, fiber couplers show a strong dependence on wavelength, so the splitting ratio for either the signal or the reference typically differs from 50:50. We will demonstrate this effect using parameters relevant to our setup. Let us assume that the reference phase is locked at $\frac{\pi}{2}$ and the interferometer arm losses are relatively detuned by 1%, which corresponds to $\mu_A = 1\%$. This detuning can potentially impact both the signal and the reference. But in our case, the fiber couplers are designed for the signal with the wavelength 810 nm, thus $T_{1,2} \approx 0.5$ and the signal phase is estimated correctly. However, for the reference with the wavelength 840 nm, the fiber couplers are unbalanced ($T_{1,2} = 0.35$). According to Eq. (2), the reference phase is estimated with a 0.1-degree error. Consequently, the phase is locked with a 0.1-degree error.

So far, we have discussed phase errors caused by intensity fluctuations. Now let us briefly discuss the impact of wavelength fluctuations. As the phase $\varphi$ and the wavelength $\lambda$ are fundamentally connected by equation $\varphi = 2\pi\frac{\Lambda}{\lambda}$, $\Lambda$ being optical path difference, wavelength instabilities in general affect the phase. In the dual-wavelength configuration, the phase error is present if the phase between the signal and the reference drifts relatively. The relative phase drift

Optics EXPRESS

$\varphi_s - \varphi_r$ for small wavelength drift $\Delta\lambda$ is described as

$$\varphi_s - \varphi_r = 2\pi \left( \frac{\Lambda_s}{\lambda_s^2} \Delta\lambda_s - \frac{\Lambda_r}{\lambda_r^2} \Delta\lambda_r \right), \tag{3}$$

where indices s and r denote the signal and the reference, respectively. One way to eliminate the relative phase drift is to precisely balance the interferometer arms. Then chromatic dispersion should be equal in each arm to achieve $\Lambda_s = \Lambda_r = 0$ for both wavelengths. In practice, interferometers usually have some degree of imbalance and in some cases, the imbalance is even required. Then it is beneficial to lock the signal and the reference wavelengths in order to avoid the relative phase drift. An interesting question in this case is which wavelength gap to choose between the signal and the reference. In case of zero chromatic dispersion $\Lambda_s = \Lambda_r$ there is no preferred wavelength gap. However, if dispersion is present, then $\Lambda_s \neq \Lambda_r$ and the conventional wavelength locking cannot avoid the relative phase drift. In this case it is convenient to minimize the dispersion by choosing a small wavelength gap or to employ a more sophisticated wavelength locking, taking into account the dispersion. Note however that the smaller the wavelength gap the harder is to separate wavelengths at the output.

## 3. Experiment

The experimental setup is depicted in Fig. 2. Single-mode coupled light-emitting diode (LED) provides an intensity and spectrally stable source of the reference. The spectral stability is further improved by adding interference filters with a central wavelength of 840 nm and full width at half maximum (FWHM) of 21 nm. In the signal ports, arbitrary light within the 3 nm FWHM around 810 nm can be injected. For active phase locking characterization, we injected the signal in a single input port. The signal is generated by a single-mode coupled and spectrally filtered LED, which perfectly simulates spectral properties of typical quantum photonic sources such as a spontaneous parametric down-conversion pumped by ultra-short pulses. Before coupling into the MZI, both the signal and the reference are horizontally polarized.

The signal and the reference are merged at a balanced fiber coupler (FC1) and co-propagate through the MZI. To achieve simultaneously high visibility and fast switching capabilities, the MZI combines fiber and free-space elements. Single-mode polarization-maintaining fiber part of a total length of 8 m provides inherent spatial and polarization overlap together with the phase control. Path balancing, polarization filtration, and dispersion compensation are achieved in 0.5 m of free space. Balanced fiber couplers optimized for 810 nm are used to split and merge the interfering light. Their splitting ratios are estimated to be 51:49 for the signal and 35:65 for the reference. The splitting ratio of FC1 can be effectively modified to perfect 50:50 operation by adjusting losses in one MZI arm. The arm lengths are balanced in the free space by micrometric translation of one coupling lens. Thanks to the 21 nm broad spectrum of the reference, we can balance MZI arms within approximately two wavelengths, i.e., with phase precision of $\pm 2\pi$. To improve polarization degree of light, two pairs of polarizing beam splitters (PBSs) with extinction greater than 30 dB are used. One pair of PBSs is placed in the free-space part, and the other pair is included in the wavelength separation part. The MZI allows for sub-ns switching via 10 GHz integrated electro-optic modulators (EOMs) as presented in the work [14]. The switching operates in a different frequency region (MHz-GHz) than the active phase locking ($\leq$kHz), therefore there is no interaction between these processes. The switching capability is crucial in applications of the MZI, however, it significantly increases chromatic dispersion in the MZI. To cancel out the dispersion, we compose MZI arms symmetrically. Namely, the fiber lengths are balanced with mm precision, and similar EOMs are placed in both arms. Additional dispersion compensation and manipulation are performed in free space with a custom component called phase dispersion compensator consisting of two elements, PDC1 and PDC2. As shown in Fig. 3(a), the PDC1 consists of two 1 cm thick high-dispersion SF10 glass plates mounted

Optics EXPRESS

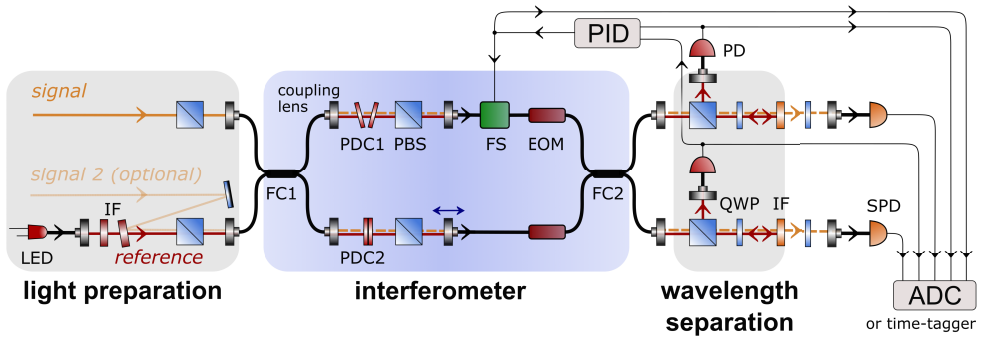


**Fig. 2.** Experimental setup for an interferometer with active phase locking. The signal and the reference are injected into the interferometer and co-propagate through 8 m of fibers and 0.5 m of free space in each arm. The interferometer is assembled to maximize interference visibility for a broad spectrum and simultaneously provide fast phase switching. At the interferometer outputs, the signal and the reference are separated and detected. The detected reference is processed by a PID controller, and consequently, the phase is locked via a fiber stretcher. Legend: light-emitting diode (LED), interference filter (IF), polarizing beam splitter (PBS), fiber coupler (FC), phase dispersion compensator (PDC), fiber stretcher (FS), electro-optic phase modulator (EOM), quarter-wave plate (QWP), photodiode (PD), sensitive photodiode or single-photon detector (SPD), proportional-integral-derivative controller (PID), analog-to-digital convertor (ADC).

on contra-directional tilting stages. The PDC1 allows for manipulating the relative optical path between the wavelengths without any misalignment of their fiber coupling. Thus we can set an arbitrary relative phase between the signal and the reference. This enables the reference to be locked at the most sensitive point of the interference fringe (phase $\frac{\pi}{2}$) regardless of the signal phase. PDC2 consists of a fixed SF10 glass plate with 3 cm thickness to compensate for the residual dispersion. As a result, we reach the visibility of 99.6% for both MZI outputs for the 3 nm broad signal and 98.6% for one output of the 21 nm broad reference.

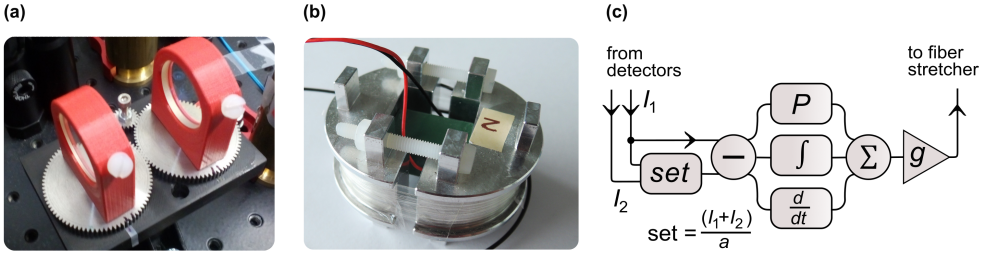


**Fig. 3.** (a) Phase dispersion compensator PDC1 used for tuning the relative phase between the signal and the reference. (b) Fiber stretcher used for the phase locking. By applying voltage to a piezoelectric crystal, the fiber coiled around two aluminium segments is stretched and the phase is changed. (c) Schematic sketch of the PID controller. Detected reference intensities $I_1, I_2$ (their voltage equivalents) are processed by the adaptive setpoint term (set) and a fraction of their sum is used as the setpoint. The setpoint is subtracted with $I_1$ and the resulting error signal is split among proportional, integral, and derivative terms. While the proportional term simply amplifies the error signal, the integral term operates with low frequencies (up to 10 Hz), and the derivative term responds to high-frequency components of the error signal (kHz). Proportional, integral, and derivative terms are summed, and the resulting signal is after amplification applied to the fiber stretcher.

Optics EXPRESS

At each MZI output, the wavelengths are demultiplexed via a dichroic optical isolator assembled from a PBS, a quarter-wave plate (QWP), and an interference filter. We reach negligible crosstalk of 30 photons/s from the reference to the signal, equivalent to extinction better than 80 dB. The separation occurs at the narrow-band interference filter centered at 810 nm, where the signal passes through while the reference is reflected back. Subsequently, the reference is reflected at the PBS. This is possible since the reference polarization is transformed from horizontal to vertical by bi-directional propagation through a 45-degree oriented QWP and $\pi$ phase shift caused by reflection at the interference filter. Since the QWP undesirably changes the signal polarization, we use a compensatory QWP after the wavelength separation part. Before the detection, both the signal and the reference are coupled into a single-mode fiber. For the signal, polarization-maintaining fibers are used, which facilitates its transfer to following experimental stages. During active phase locking tests, the signal with the power of about 1 pW ($4 \cdot 10^6$ photons/s) impinges directly the ultra-sensitive silicon photodiodes with noise equivalent power (NEP) of 1.4 fW/$\sqrt{\text{Hz}}$ and 30 Hz bandwidth. For single-photon measurements, we use single-photon avalanche diodes with a 50 Hz dark count rate plugged into a time tagger. The overall loss of the signal is around 80%, including mixing and separation of the reference. The loss is slightly higher for the reference since all components are optimized for the signal wavelength. The system was not optimized for minimum losses, though.

The active phase lock is carried out by a feedback loop composed of the photodiodes, PID controller, and a fiber stretcher. The reference with the power of 1.5 nW impinges silicon photodiodes with NEP=9 fW/$\sqrt{\text{Hz}}$ and 2 kHz bandwidth. The resulting electronic signals are processed by an in-house developed analog PID controller schematically sketched in Fig. 3(c). Full electronic scheme is available in GitHub repository [31]. Compared to a conventional PID controller, the circuit is provided with the adaptive setpoint described in Methods. Therefore, we lock the phase regardless of the intensity fluctuations of the reference. The PID controller is fine-tunable in each parameter via 10-turn precision potentiometers. As a result, the target phase is set with high accuracy. To provide correct phase estimation for the adaptive setpoint, we include additional tunability to cancel out detector offsets and to balance detection efficiencies. The PID controller is designed to drive a custom-made fiber stretcher depicted in Fig. 3(b). It has 7.2 $\mu$F capacitance, 1 kHz bandwidth, 0.11 V half-wave voltage, and dynamic range of $\pm$275 $\mu$m [26]. Since the extent of the phase drift is much smaller in our case, we use only $\pm$110 $\mu$m corresponding to the output voltage range of the PID controller.

To reduce air flux and temperature instabilities, we cover the whole setup with styrofoam plates during all measurements. The passive protection reduces the temperature drift from 2°C peak-to-peak per 2 hours to a peak-to-peak drift of 0.3°C per 15 hours. Our setup is placed on a 60x60x6 cm breadboard with no additional damping of mechanical vibrations. For the data acquisition, we use an 8-channel 18-bit analog-to-digital converter set to a sampling frequency of 16 Hz. We increase SNR by averaging the data samples to 1 Hz except for the detailed spectral characterization (Fig. 4(b)) and inset in Fig.(a) showing the short-term stability. We collect data at each detector, and additionally, we monitor the voltage applied to the fiber stretcher. The knowledge of the driving voltage, together with the information on half-wave voltage, allows for the evaluation of the compensated phase drift. The collected data are processed by an algorithm based on Eq. (1). Apart from the output intensities, it requires additional parameters such as the visibility of each MZI output and a ratio of losses in the MZI outputs. For measurements with a non-stabilized phase, these parameters are periodically recovered as interference fringes are scanned spontaneously due to the phase drift. While the stabilization process is running, interference fringe scanning is not possible, thus the additional parameters are independently measured before the stabilization starts.

Optics EXPRESS

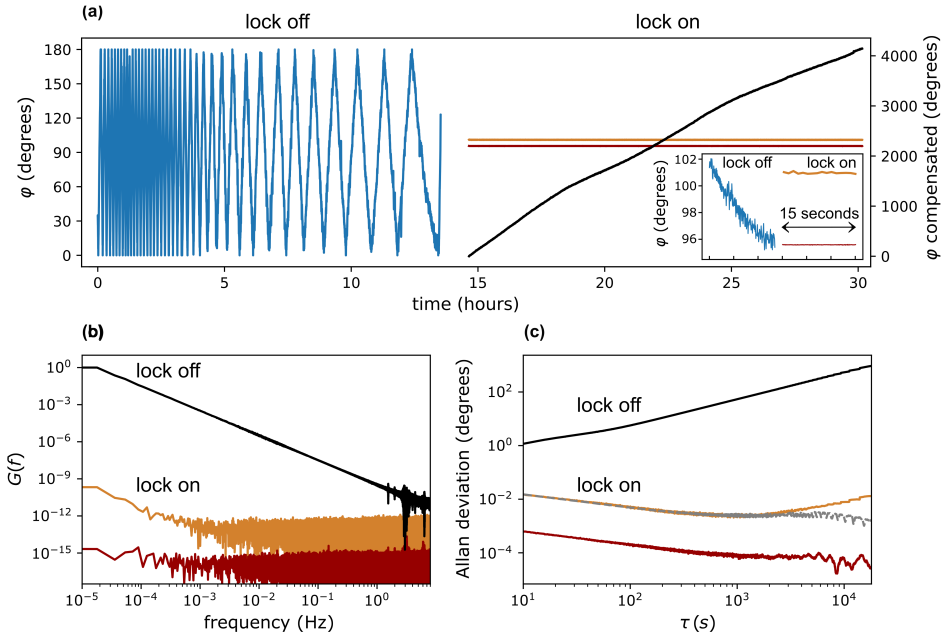


**Fig. 4.** Comparison of stabilized and non-stabilized MZI. In stabilized MZI, the reference and the signal are represented by the red line and the orange line, respectively. (a) Stability in the time domain. The blue line represents the phase in non-stabilized MZI and the black line corresponds to the phase drift compensated during the phase locking (see the right vertical axis). The inset shows the stability in the short term. (b) Spectral power density $G$ of the phase noise. (c) Allan deviation of the phase noise. The gray line illustrates the noise level of the signal acquisition.

## 4. Results and discussion

We compare the performance of the MZI with and without the active stabilization and present the phase stability in three ways: in the time domain, in the frequency domain, and via the Allan deviation. The results in the time domain are depicted in Fig. 4(a). The typical phase drift of non-stabilized MZI is shown on the left side. On the right side, we show phase noise for stabilized MZI (orange and red lines) and the phase compensated during the stabilization process (black line). The inset represents a detailed view of the phase noise. For further analysis, we use only black, orange, and red datasets since they were achieved within the same environmental conditions. While the phase lock is active, a phase drift of 4000 degrees per 15 hours is virtually eliminated. In terms of standard deviation accumulated over a typical single-photon sampling frequency of 1 Hz, we reach 0.05 degrees for the signal and 0.002 degrees for the reference within a 15-hour interval.

Further, we analyze the spectral power density of the phase noise shown in Fig. 4(b). During the stabilization process, the phase noise is suppressed by 9 orders of magnitude for frequencies in the range $10^{-3}$ to $10^{-5}$ Hz. For frequencies above $10^{-3}$ Hz, the phase noise is primarily given by detection noise. Furthermore, we evaluate the Allan deviation of the phase noise depicted in Fig. 4(c). Allan deviation corresponds to root mean square phase drift for a variable time interval $\tau$ [27]. For the signal, we reach Allan deviation below $2 \times 10^{-2}$ degrees for time intervals from 10 s to more than 5 hours. The minimum value $2 \times 10^{-3}$ degrees is achieved for $10^3$ s. Allan deviation of the reference is evaluated to be smaller than $10^{-3}$ degrees.

Optics EXPRESS

The results show that the reference exhibits higher phase precision than the signal. This discrepancy has two reasons. Firstly, the signal is affected by a higher amount of detection noise than the reference. Specifically, the detection noise overlaps with the signal up to $10^3$ s as illustrated by the gray line in Fig. 4(c). Secondly, the signal is slightly affected by the residual LSD leading to increased phase error in the long term. Considering the aforementioned reasons, the Allan deviation of the signal should be interpreted as an upper bound of the real phase error in the MZI. On the other hand, the Allan deviation of the reference gives the lower bound of the real phase error since it does not reflect LSD. We estimate that in the short term, where LSD is negligible, the real Allan deviation follows the reference curve, whereas, in the long term, it approaches the signal curve. The measured phase precision of the reference illustrates the ultimate performance of the phase lock. Therefore, the direct demonstration of sub-$10^{-3}$ degree Allan deviation for time intervals up to $10^4$ s is feasible provided that we completely cancel out LSD and improve SNR of the signal detection.

Although, in general, the performance of phase locking is dependent on the reference phase (the best performance is achieved in $\pi/2$), we are not limited to a specific phase value of the signal. In Fig. 5, we show the phase locking for an arbitrary signal phase while being locked with the reference close to $\pi/2$. This is possible due to full phase tunability between the signal and the reference achieved by the phase dispersion compensator element (see Experiment for details). Figure 5(a) shows the full tunability for a classical signal, while in Fig. 5(b) we demonstrate the tunability for the single-photon signal (count rate approx. $5 \times 10^5$ counts/s, integration time 1 s). Additional results at the single-photon level were achieved previously with preliminary versions of the setup. Firstly, we demonstrated balanced time-bin multiplexing for photon-number resolving detection using a loop configuration [14]. Secondly, we demonstrated the Fock state conversion exploiting feedforward control of the interferometer [13]. These experiments were performed before a significant improvement of the phase lock, hence they do not reflect the unprecedented phase stability presented here.

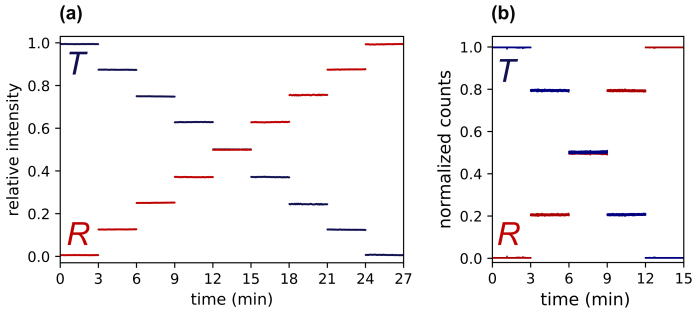


**Fig. 5.** Complete phase tunability via the phase dispersion compensator demonstrated for a classical signal (a) and single photons (b). Although the reference is locked at the most sensitive phase $\frac{\pi}{2}$, we are able to tune arbitrary splitting ratio $T$:$R$ for the signal.

Let us compare our results with other state-of-the-art experiments across various interferometer configurations and target applications. Niwa et al. reported 20 pm phase noise between 0.3 mHz and 1 Hz in 5x5 cm free-space MZI [28]. The results are achieved for strong light and classical detectors. They use advanced passive and active methods of protection against environment changes: the setup is placed in a vacuum chamber with 1 mK thermal stability, and the MZI elements are composed of ultralow expansion glass. In comparison, we reach phase noise around 100 pm within a much larger frequency interval (0.02 mHz to 1 Hz) for an 8 m long fiber interferometer placed in a standard lab environment. In the field of single-photon experiments, the phase stability is typically in order of a few degrees [6,15,17,20–23,29]. Five of

Optics EXPRESS

the aforementioned works are limited to short-term operation (up to few minutes) [6,15,20–22], whereas long-term stability (up to several hours) is achieved only in three works [17,23,29]. To the best of our knowledge, the most precise stabilization of a single-photon interferometer has been reported by Toliver et al. [8] and Roztocki et al. [30]. Toliver et al. achieved a 200 s phase lock with a standard deviation of 0.2 degrees. In contrast, we demonstrate a standard deviation of 0.05 degrees for more than 15 hours. Roztocki et al. reached Allan deviation below 0.2 degrees from $10^{-1}$ s to $10^{4}$ s, but these results were demonstrated only for a bright reference light (the phase was not reconstructed using an independent signal as in our case). In contrast, we reach Allan deviation below $5 \times 10^{-3}$ degrees for the reference within the same interval.

Our results demonstrate the unprecedented performance of dual-wavelength phase locking across single-photon interferometers. Our approach will work for all types of interferometers and complex interferometric networks, including fiber and free-space propagation. Regarding free-space interferometers, phase locking might be even simpler, as a small spatial displacement between the signal and the reference can substitute the wavelength separation. However, this scheme is not free from the relative phase drift between the signal and the reference since the index of refraction in air locally changes for each of the displaced paths [29]. In terms of fiber configuration, it is recommended to use polarization-maintaining architecture to avoid polarization drift inside the interferometer. Polarization drift causes an effect similar to LSD, affecting the phase locking. If polarization-maintaining architecture cannot be used, it is possible to employ an active polarization control. Although we demonstrate the phase-locking on a balanced interferometer, the technique can be utilized for unbalanced interferometers as well, provided that a sufficiently coherent source is employed as the reference. However, highly coherent sources can bring additional challenges due to random interference on optical surfaces and elements, leading to intensity fluctuation throughout the setup.

## 5. Conclusion

We have implemented a novel technique of continuous phase locking for single-photon circuits and networks. Our approach extends dual-wavelength stabilization methods by the adaptive setpoint, enabling precise phase locking despite the fluctuating intensity. We show that the adaptive setpoint, together with thorough optimization in all possible degrees of freedom, leads to unprecedented stability even with faint optical signals. We have experimentally demonstrated sub-0.1 degree phase locking of 8.5 m long fiber-based MZI for more than 15 hours. Specifically, we have reached a phase standard deviation of 0.05 degrees, which is equivalent to the path displacement of about 100 pm. To the best of our knowledge, our results represent the most precise phase locking of single-photon interferometers. Moreover, we have reached complete phase tunability of the device and negligible crosstalk from the reference to the single-photon signal. Since our method can be implemented in a vast majority of interferometric networks, it can significantly improve the performance of many phase-sensitive applications in information processing, quantum metrology, and quantum communication.

**Funding.** Ministerstvo Školství, Mládeže a Tělovýchovy (CZ.02.2.69/0.0/0.0/19/073/0016713, DSGC-2021-0118); Grantová Agentura České Republiky (19-19189S).

**Acknowledgments.** We thank Petr Novák for his help with the 3D printing of the phase dispersion compensator mount. Student grant DSGC-2021-0118 is funded under the OPIE project, Improvement of Doctoral Student Grant Competition Schemes and their Pilot Implementation, reg. no. CZ.02.2.69/0.0/0.0/19_073/0016713 .

**Disclosures.** The authors declare that there are no conflicts of interest related to this article.

**Data Availability.** Data underlying the results presented in this paper are available in Ref. [31].

## References

1. X. song Ma, S. Zotter, N. Tetik, A. Qarry, T. Jennewein, and A. Zeilinger, "A high-speed tunable beam splitter for feed-forward photonic quantum information processing," Opt. Express **19**(23), 22723–22730 (2011).

Optics EXPRESS


2. M. Miková, H. Fikerová, I. Straka, M. Mičuda, J. Fiurášek, M. Ježek, and M. Dušek, "Increasing efficiency of a linear-optical quantum gate using electronic feed-forward," Phys. Rev. A **85**(1), 012305 (2012).
3. V. Giovannetti, S. Lloyd, and L. Maccone, "Advances in quantum metrology," Nat. Photonics **5**(4), 222–229 (2011).
4. J. Aasi, J. Abadie, and B. Abbott, *et al.*, "Enhanced sensitivity of the LIGO gravitational wave detector by using squeezed states of light," Nat. Photonics **7**(8), 613–619 (2013).
5. G. S. Thekkadath, M. E. Mycroft, B. A. Bell, C. G. Wade, A. Eckstein, D. S. Phillips, R. B. Patel, A. Buraczewski, A. E. Lita, T. Gerrits, S. W. Nam, M. Stobińska, A. I. Lvovsky, and I. A. Walmsley, "Quantum-enhanced interferometry with large heralded photon-number states," npj Quantum Inf. **6**(1), 89 (2020).
6. G. B. Xavier and J. P. von der Weid, "Stable single-photon interference in a 1 km fiber-optic Mach–Zehnder interferometer with continuous phase adjustment," Opt. Lett. **36**(10), 1764–1766 (2011).
7. G. Carvacho, J. Cari ne, G. Saavedra, Á. Cuevas, J. Fuenzalida, F. Toledo, M. Figueroa, A. Cabello, J.-Å. Larsson, P. Mataloni, G. Lima, and G. B. Xavier, "Postselection-loophole-free Bell test over an installed optical fiber network," Phys. Rev. Lett. **115**(3), 030503 (2015).
8. P. Toliver, J. M. Dailey, A. Agarwal, and N. A. Peters, "Continuously active interferometer stabilization and control for time-bin entanglement distribution," Opt. Express **23**(4), 4135–4143 (2015).
9. S.-B. Cho and H. Kim, "Active stabilization of a fiber-optic two-photon interferometer using continuous optical length control," Opt. Express **24**(10), 10980–10986 (2016).
10. Y. Xu, J. Lin, Y. Li, H. Dai, S. Liao, and C. Peng, "Active Phase stabilization for the interferometer with 128 actively selectable paths," IEEE Trans. Nucl. Sci. **66**(7), 1076–1080 (2019).
11. X.-s. Ma, S. Zotter, J. Kofler, R. Ursin, T. Jennewein, Č. Brukner, and A. Zeilinger, "Experimental delayed-choice entanglement swapping," Nat. Phys. **8**(6), 479–484 (2012).
12. F. Vedovato, C. Agnesi, M. Tomasin, M. Avesani, J.-A. Larsson, G. Vallone, and P. Villoresi, "Post-selection-loophole-free Bell violation with genuine time-bin entanglement," Phys. Rev. Lett. **121**(19), 190401 (2018).
13. V. Švarc, J. Hloušek, M. Nováková, J. Fiurášek, and M. Ježek, "Feedforward-enhanced Fock state conversion with linear optics," Opt. Express **28**(8), 11634–11644 (2020).
14. V. Švarc, M. Nováková, G. Mazin, and M. Ježek, "Fully tunable and switchable coupler for photonic routing in quantum detection and modulation," Opt. Lett. **44**(23), 5844–5847 (2019).
15. Y. Takeno, M. Yukawa, H. Yonezawa, and A. Furusawa, "Observation of -9 dB quadrature squeezing with improvement of phase stability in homodyne measurement," Opt. Express **15**(7), 4321–4327 (2007).
16. T. Eberle, V. Händchen, and R. Schnabel, "Stable control of 10 dB two-mode squeezed vacuum states of light," Opt. Express **21**(9), 11546–11553 (2013).
17. V. Makarov, A. Brylevski, and D. R. Hjelme, "Real-time phase tracking in single-photon interferometers," Appl. Opt. **43**(22), 4385–4392 (2004).
18. S. Takeda and A. Furusawa, "Universal quantum computing with measurement-induced continuous-variable gate sequence in a loop-based architecture," Phys. Rev. Lett. **119**(12), 120504 (2017).
19. S. Takeda, K. Takase, and A. Furusawa, "On-demand photonic entanglement synthesizer," Sci. Adv. **5**(5), eaaw4530 (2019).
20. D. Pulford, C. Robillard, and E. Huntington, "Single photon locking of an all-fiber interferometer," Rev. Sci. Instrum. **76**(6), 063114 (2005).
21. S. Suzuki, H. Yonezawa, F. Kannari, M. Sasaki, and A. Furusawa, "7 dB quadrature squeezing at 860 nm with periodically poled K Ti $OPO_4$," Appl. Phys. Lett. **89**(6), 061116 (2006).
22. S.-B. Cho and T.-G. Noh, "Stabilization of a long-armed fiber-optic single-photon interferometer," Opt. Express **17**(21), 19027–19032 (2009).
23. S. Yanikgonul, R. Guo, A. Xomalis, A. N. Vetlugin, G. Adamo, C. Soci, and N. I. Zheludev, "Phase stabilization of a coherent fiber network by single-photon counting," Opt. Lett. **45**(10), 2740–2743 (2020).
24. K. R. Motes, A. Gilchrist, J. P. Dowling, and P. P. Rohde, "Scalable boson sampling with time-bin encoding using a loop-based architecture," Phys. Rev. Lett. **113**(12), 120501 (2014).
25. Y. He, X. Ding, and Z.-E. Su, *et al.*, "Time-bin-encoded boson sampling with a single-photon device," Phys. Rev. Lett. **118**(19), 190501 (2017).
26. M. Nováková, L. Podhora, V. Švarc, and M. Ježek, "Polarization-maintaining 3D printed fiber stretcher," in preparation (2022).
27. D. W. Allan, "Statistics of atomic frequency standards," Proc. IEEE **54**(2), 221–230 (1966).
28. Y. Niwa, K. Arai, A. Ueda, M. Sakagami, N. Gouda, Y. Kobayashi, Y. Yamada, and T. Yano, "Long-term stabilization of a heterodyne metrology interferometer down to a noise level of 20 pm over an hour," Appl. Opt. **48**(32), 6105–6110 (2009).
29. M. Mičuda, E. Doláková, I. Straka, M. Miková, M. Dušek, J. Fiurášek, and M. Ježek, "Highly stable polarization independent Mach-Zehnder interferometer," Rev. Sci. Instrum. **85**(8), 083103 (2014).
30. P. Roztocki, B. MacLellan, M. Islam, C. Reimer, B. Fischer, S. Sciara, R. Helsten, Y. Jestin, A. Cino, S. T. Chu, B. Little, D. J. Moss, M. Kues, and R. Morandotti, "Arbitrary phase access for stable fiber interferometers," Laser Photonics Rev. **15**(7), 2000524 (2021).
31. V. Švarc, "GitHub repository SvarcOpticsOlomouc/stabilization," https://github.com/SvarcOpticsOlomouc/stabilization.

# Chapter 5

# Photonic switch

In this chapter, we present experimental research in photonic switching published as work [1]. The photonic switch is implemented as a Mach-Zehnder interferometer with embedded integrated EOMs. The main aim was to achieve sub-ns switching with a high extinction and low latency, enabling advanced feedforward protocols. In this article, apart from the switching capabilities, we demonstrate active time multiplexing via the loop configuration of the switch. Since the article was limited to four pages only, we enclose an extended discussion of the loop-based time multiplexing at the end of this chapter. A resume of the article follows, the full article is enclosed below.

Fast splitting, switching, and routing of light are critical tools of photonic technology in the rapidly developing fields of optical communication and optical information processing. We have developed a low-latency switchable coupler employing a high-visibility fiber MZI. We demonstrate fast switching of the coupler by changing its operation between any splitting ratios in a fraction of nanosecond. The splitting ratio is controlled using low-voltage electronic signal compatible with the output of the majority of photodetectors, which is crucial for utilization of the coupler in optical feedback and feedforward circuits. We show outstanding performance of the reported device in two demanding applications, namely a balanced time-multiplexed device for photon-number-resolving detectors and an active preparation of a photonic time-bin encoded 4-level state with time-bin separation in the range of tens of nanoseconds.

The developed coupler is based on a fiber MZI where the splitting ratio can be switched by changing the optical phase using an integrated waveguide EOM, see Fig. 5.1. The MZI was implemented to have high interference visibility resulting in high extinction ratio, exceptional phase stability enabling a long-term continuous operation (already discussed in the previous chapter),

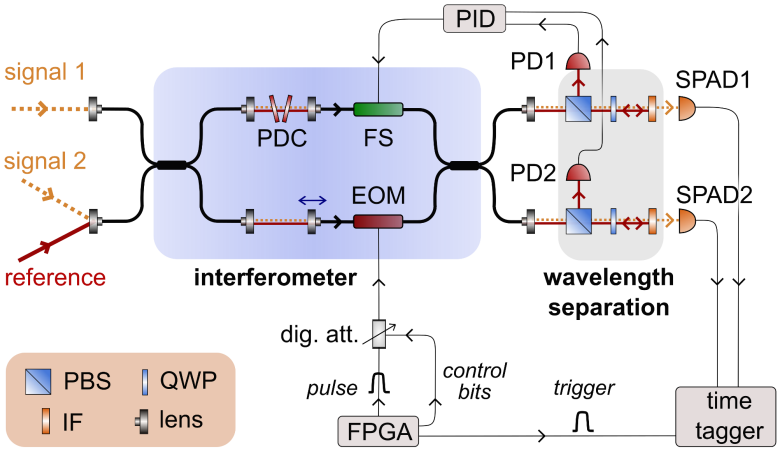


**Figure 5.1:** Simplified experimental scheme of the switchable coupler showing the signal and reference beams entering the MZI and being separated at its output. Phase dispersion compensator (PDC) and fiber stretcher (FS) are used to lock the MZI phase based on the reference detection at the photodiodes (PD1,2). Integrated electro-optic modulator (EOM) driven by FPGA based electronics is employed for switching the coupler between arbitrary splitting ratios. The output signals are detected by single-photon avalanche diodes (SPAD1,2).

and fast modulation with low overall latency between a control electronic signal and the response of the switching. In what follows we will discuss these design goals and the corresponding features of the presented solution.

High interference visibility operation requires perfect indistinguishability of interfering optical signals at the output of the MZI in all relevant degrees of freedom, namely path, spatial mode, polarization, time, and frequency. The path information is reduced by making the signals in both arms of the MZI of the same intensity by slight tuning of losses. Also, the splitting ratio of the output fiber splitter has to be close to 50:50. Spatial indistinguishability is inherent in single-mode fiber implementation. Polarization-maintaining fibers are utilized throughout the setup to keep the polarization constant in time and the same for both the MZI arms. All connector splices are made to minimize polarization crosstalk between the fiber axes, and additional polarization filtering is also included. The MZI arms are carefully adjusted to have the same optical path length using tunable air gaps. The difference between the MZI arms is further minimized by placing the components symmetrically in both arms. This is particularly important for the components exhibiting strong dispersion such as integrated EOMs and dispersion compensators. Having all these degrees of freedom under control and precisely adjusted, we have reached the interference visibility of 99.55% in the optical bandwidth

of 3 nm around 810 nm (equivalent to spectral bandwidth of 1.3 THz and pulse length down to 300 fs). It results in switching with the extinction ratio of 26 dB for continuous as well as pulsed optical signals.

The response time, also termed latency, of the realized switchable coupler is given by the propagation delay of the optical signal from the input to the output of the device and, also, by the response of the phase modulator employed. The coupler is approximately 9 m long, which corresponds to the delay of 45 ns. It can be decreased below 10 ns easily by reducing the pigtail length of the constituent components and shortening the fiber stretcher sacrificing its dynamic range. The waveguide integrated $LiNbO_3$ EOM features 10 GHz bandwidth with negligible impact on the overall latency. The modulator is controlled by voltage signals within 0 – 2.2 V using electronic pulse generator with 3.5 ns pulse width and 0.4 ns rise time for the response characterization, and a field-programmable gate array (FPGA) with 10 ns clock period to control complex measurement protocols. The FPGA was supplemented with a GaAs FET 6-bit digital attenuator with the 0.5 dB step to generate pulse sequences used for switching the coupler between arbitrary splitting ratios.

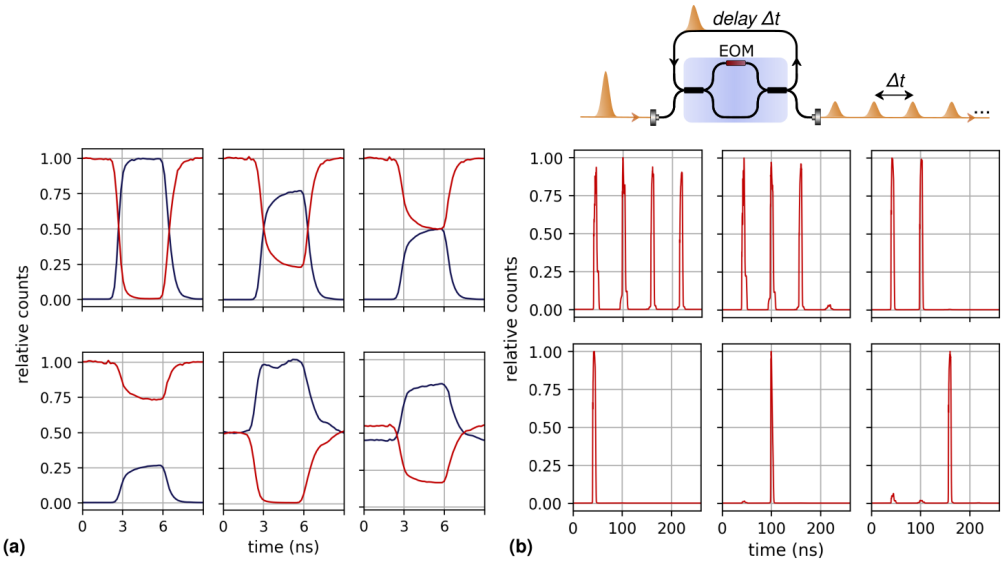


**Figure 5.2:** (a) Examples of fast switching. Red and blue data points correspond to two outputs of the interferometer. (b) Loop-based temporal multiplexing using the reported switchable coupler: scheme of the experiment (up) and various configurations of time-bin encoded 4-level photonic signal (down).

The time response was evaluated by setting a fixed initial splitting ratio and sending an electronic control pulse to the coupler. The switching pro-

cess was observed at the output ports while the single-photon level signal was injected in the first input port of the device. The accumulated photon-counting histograms are shown in Fig. 5.2(a) for various initial and target splitting ratios to demonstrate arbitrariness of the switching. The data are depicted without corrections, except for SPAD afterpulses subtraction (maximum 1% of the signal) and normalization, to show the temporal evolution of the transmittance and reflectance. The switching speed determined as the rise time (10%-90%) of the measured histograms is 0.7 ns, though the actual response of the coupler switching is estimated to be less than 0.1 ns. The limiting factors of the switching speed measurement were detection jitter, the shape of the driving pulse, and time-tag resolution.

The input optical pulse can be multiplexed in many time bins when reflected part of the signal is fed from the output of the coupler to its input to create a loop, as shown in Fig. 5.2(b). Electronic control pulses applied to the EOM have to be synchronized with the optical pulse repeatedly passing the coupler. This scheme follows the proposal of a time-multiplexed device for photon-number-resolving detectors [74]. The reported switching protocol can be generalized to arbitrary time multiplexing. We demonstrate full control over the amplitude of the individual time bins with the mean fidelity of 98.9%. Several examples of time-bin encoded 4-level optical system are depicted in Fig. 5.2(b). Tunable routing of the input signal to the resulting time bins can be complemented by their arbitrary phase modulation using EOMs in both the MZI arms. Starting from single photon input, such the routing represents an efficient way of preparing a photonic multi-level system (qudit). A second switchable coupler would be needed for the qudit analysis at the receiver.

To conclude, we have presented the sub-nanosecond switchable coupler optimized for routing faint optical signals and single photons. We have verified full tunability of the splitting ratio from 0:100 to 100:0 with the exceptional extinction of 26 dB. We have reached for the first time the balanced operation of loop-based photon-number-resolving detector exploiting the full control over the splitting ratio and ultimate stability of the developed coupler. Furthermore, we have demonstrated the deterministic preparation of photonic time-bin four-level qudit with a clock cycle of 60 ns using the presented coupler and a single delay loop.

Optics Letters

# Fully tunable and switchable coupler for photonic routing in quantum detection and modulation

VOJTĚCH ŠVARC, MARTINA NOVÁKOVÁ, GLIB MAZIN, AND MIROSLAV JEŽEK*

*Department of Optics, Faculty of Science, Palacký University, 17. listopadu 12, 77146 Olomouc, Czech Republic*
**Corresponding author: jezek@optics.upol.cz*

*Received 26 August 2019; revised 23 October 2019; accepted 28 October 2019; posted 28 October 2019 (Doc. ID 374506); published 28 November 2019*

**Photonic routing is a key building block of many optical applications challenging its development. We report a 2 × 2 photonic coupler with a splitting ratio switchable by a low-voltage electronic signal with 10 GHz bandwidth and tens of nanoseconds latency. The coupler can operate at any splitting ratio ranging from 0:100 to 100:0 with the extinction ratio of 26 dB in optical bandwidth of 1.3 THz. We show sub-nanosecond switching between arbitrary coupling regimes including a balanced 50:50 beam splitter, 0:100 switch, and a photonic tap. The core of the device is based on a Mach–Zehnder interferometer in a dual-wavelength configuration allowing real-time phase lock with long-term sub-degree stability at single-photon level. Using the reported coupler, we demonstrate for the first time, to the best of our knowledge, a perfectly balanced time-multiplexed device for photon-number-resolving detectors and also the active preparation of a photonic temporal qudit state up to four time bins. Verified long-term stable operation of the coupler at the single-photon level makes it suitable for a wide application range in quantum information processing and quantum optics in general.** 

https://doi.org/10.1364/OL.44.005844

Fast splitting, switching, and routing of light are critical tools of photonic technology in the rapidly developing fields of optical communication and optical information processing, including demanding applications such as quantum cryptography [1], neuromorphic computing [2,3], photonic simulations [4], scalable boson sampling [5,6], universal quantum computing [7], entanglement synthesizing [8], and photon counting [9]. In the last few years, high-efficiency single-photon generation has been demonstrated employing active time multiplexing [10–12]. Optical switching has also facilitated a recent pioneering demonstration of postselection-loophole-free violation of Bell's inequality with genuine time-bin entanglement [13].

The most advanced modulation, processing, and detection schemes require ultra-low latency between the control signal and the switch response, together with a large bandwidth and high extinction. Furthermore, the continuous tunability with an arbitrary splitting ratio is required [1,7]. The universal routing device would also be able to coherently superpose two incident signals acting as a coupler *switchable* between various splitting ratios. Free-space polarization-based switchable couplers using Pockels cells [6,8,9] feature ultra-low loss; however, they require high switching voltage. Consequently, they cannot provide continuous tunability, and it is very demanding to reach ultra-low latency. An alternative technique utilizes cross-phase modulation in a Sagnac interferometer driven by an auxiliary strong optical pulse [14]. This approach is polarization insensitive and exhibits medium loss and high speed; however, the latency is high, making its usage impractical in most loop-based schemes and temporal multiplexing in general. Another approach employs electro-optic phase modulators (EOMs) in a Mach–Zehnder interferometer (MZI) [13]. Using integrated EOMs instead of free-space modulators, we can reach ultra-high speed and low latency at the cost of increased loss.

The MZI operates as a 2 × 2 variable beam splitter and allows the continuous tuning of its splitting ratio. The main drawbacks of the MZI-based switchable coupler are the extinction ratio limited by visibility of the MZI and its phase instability causing the drift of the splitting ratio. The visibility optimization is particularly challenging in the case of a spectrally broad signal, such as short optical pulses and the majority of single-photon sources, and with dispersion elements utilized as a part of the MZI. The phase stability issue can be addressed by active phase locking, though it is notoriously difficult at a single-photon level or with fluctuating input signal.

In this Letter, we present a low-latency switchable coupler employing a high-visibility fiber MZI. An auxiliary light beam is injected into the MZI, co-propagates with a single-photon signal, and enables real-time continuous phase locking with a unique sub-1 deg long-term stability. The picowatt-level auxiliary beam is wavelength separated with virtually no crosstalk to the signal. We demonstrate fast switching of the coupler by changing its operation between any splitting ratios in a fraction of a nanosecond. The splitting ratio is controlled using low-voltage electronic signal compatible with the output of the majority of photodetectors, which is crucial for utilization of the coupler in optical feedback and feedforward circuits. We show outstanding performance of the reported device in two demanding applications, namely, a balanced time-multiplexed device for photon-number-resolving detectors and active preparation of a photonic time-bin encoded four-level state with time-bin separation in the range of tens of nanoseconds.

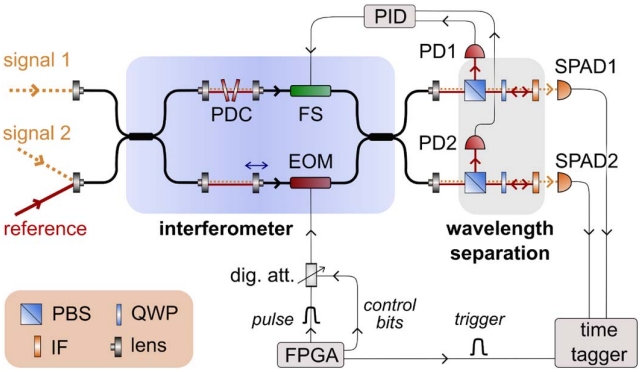


**Fig. 1.** Simplified experimental scheme of the switchable coupler showing the signal and reference beams entering the MZI and being separated at its output. Phase dispersion compensator (PDC) and fiber stretcher (FS) are used to lock the MZI phase based on the reference detection at the photodiodes (PD1,2). Integrated electro-optic modulator (EOM) driven by FPGA-based electronics is employed for switching the coupler between arbitrary splitting ratios. The output signals are detected by single-photon avalanche diodes (SPAD1,2).

The developed coupler is based on a fiber MZI where the splitting ratio can be switched by changing an optical phase using an integrated waveguide EOM (Fig. 1). The MZI was implemented to have high interference visibility resulting in a high extinction ratio, exceptional phase stability enabling long-term continuous operation, and fast modulation with low overall latency between a control electronic signal and the response of the switching. In what follows, we will discuss these design goals and the corresponding features of the presented solution.

High-interference visibility operation requires perfect indistinguishability of interfering optical signals at the output of the MZI in all relevant degrees of freedom, namely, path, spatial mode, polarization, time, and frequency. The path information is reduced by making the signals in both arms of the MZI the same intensity by slight tuning of losses. Also, the splitting ratio of the output fiber splitter has to be close to 50:50. Spatial distinguishability is inherent in single-mode-fiber implementation. Polarization-maintaining fibers are utilized throughout the setup to keep the polarization constant in time and the same for both MZI arms. All connector splices are made to minimize polarization crosstalk between the fiber axes, and additional polarization filtering is also included. The MZI arms are carefully adjusted to have the same optical path length using tunable air gaps. The difference between the MZI arms is further minimized by placing the components symmetrically in both arms. This is particularly important for the components exhibiting strong dispersion such as integrated EOMs and dispersion compensators. Having all these degrees of freedom under control and precisely adjusted, we have reached the interference visibility of 99.55% in the optical bandwidth of 3 nm around 810 nm (equivalent to spectral bandwidth of 1.3 THz and pulse length down to 300 fs). It results in switching with the extinction ratio of 26 dB for continuous as well as pulsed optical signals.

A usual problem of interferometric circuits is a random phase fluctuation caused by temperature changes, airflow, and vibrations. These adverse effects can be only partially reduced using passive methods such as thermal stabilization and acoustic and vibration isolation. On-chip circuit implementations exhibit improved stability; however, a few-degree drift per minute is still present. Therefore, active stabilization is necessary to keep the phase fluctuation small enough for advanced applications. Particularly, long-term operation of the photonic routing circuit with the ultimate extinction ratio requires a phase stability better than 1 deg. Comparing the output signal to a fixed setpoint and adjusting the phase based on the error signal represents a common solution in the case of the strong classical signal. However, such an approach is fundamentally limited by a photocounting noise when a weak optical signal is used [15]. Inherently stable interferometers [16] or repeating the stabilization and measurements steps [17] are possible solutions at the single-photon level. The best-performing technique uses an auxiliary strong optical reference co-propagating with the signal through the MZI and enabling real-time phase lock. In fibers, the reference and the signal overlap spatially and have to be multiplexed in different degrees of freedom with the wavelength being the typical choice [18]. We utilize 100 pW reference at 830 nm obtained from a spectrally and single-mode filtered luminescent diode. Its large spectral width of 10 nm allows for locking not only the optical phase but also the autocorrelation maximum, which signifies zero relative optical path of the interferometer. The reference is separated at the output of the MZI using a sequence of a polarizing beam splitter (PBS), quarter-wave plate (QWP), and a 3 nm interference filter (IF) centered at 810 nm acting together as a wavelength-selective optical isolator. The transmitted signal is detected by single-photon avalanche diodes, while the reflected reference impinges an ultra-sensitive photodiode (PD) with NEP $= 9$ fW$/\sqrt{\text{Hz}}$. The amplified PD signal from both MZI output ports is processed by a custom proportional-integral-derivative (PID) controller with the setpoint set at the maximum fringe slope and adaptively corrected for amplitude fluctuations of the reference. The produced electronic error signal is fed to a fiber stretcher (FS) with the dynamic range of 35 μm. The stabilization bandwidth is set to 30 Hz. The crosstalk from the reference to the signal is below 10 photons/s (i.e., photon crosstalk probability below $10^{-6}$ for 100 ns time bin). To manipulate the relative phase between the reference (locked to $\pi/2$) and the signal, we insert in the MZI a custom-made dispersion compensator formed by two tilted high-dispersion SF10 glass plates.

The response time, also termed latency, of the realized switchable coupler is given by the propagation delay of the optical signal from the input to the output of the device and also by the response of the phase modulator employed. The coupler is approximately 9 m long, which corresponds to the delay of 45 ns. It can be decreased below 10 ns easily by reducing the pigtail length of the constituent components and shortening the FS, sacrificing its dynamic range. Further decreasing the latency of the device seems to be superfluous especially when triggered by free-running single-photon detectors considering their typical recovery time of 10–30 ns. The waveguide integrated $LiNbO_3$ EOM features 10 GHz bandwidth with negligible impact on the overall latency. The modulator is controlled by voltage signals within 0–2.2 V using an electronic pulse generator with 3.5 ns pulse width and 0.4 ns rise time for the response characterization, and a field-programmable gate array (FPGA) with 10 ns clock period to control complex measurement protocols. The FPGA is supplemented with a GaAs 6-bit digital attenuator with the 0.5 dB step to generate pulse sequences used for switching the coupler between arbitrary splitting ratios.

We have verified the stability of the splitting ratio during continuous-wave operation and characterized the time response of the coupler to a fast-changing control signal, to demonstrate the outstanding performance of the developed coupler. The long-term stability was characterized by acquiring the output intensity for various fixed splitting ratios, particularly the most sensitive 50:50 ratio. Noise spectrum of the coupler transmittance shows 60 dB improvement for the actively real-time stabilized coupler. Allan deviation reaches the value of $5 \times 10^{-4}$ for sub-second acquisition times (affected by detector fluctuations) and exhibits a plateau at $10^{-4}$ for longer measurement durations. This is equivalent to phase stability of 0.6 deg, i.e., the optical path difference of the coupler's core interferometer is kept smaller than 1.5 nm for dozens of minutes.

The time response was evaluated by setting a fixed initial splitting ratio and sending an electronic control pulse to the coupler. The switching process was observed at the output ports while the single-photon level signal was injected in the first input port of the device. The measurement was repeated many times due to the random nature of the photon detection process, and all detection events were recorded on a time tagger. The accumulated photon-counting histograms are shown in Fig. 2 for various initial and target splitting ratios to demonstrate arbitrariness of the switching. The data are depicted without corrections, except for single-photon avalanche diodes (SPAD) afterpulses subtraction (maximum 1% of the signal) and normalization, to show the temporal evolution of the transmittance and reflectance. The switching speed determined as the rise time (10%–90%) of the measured histograms is 0.7 ns, though the actual response of the coupler switching is much faster. The measurement is affected by the SPAD jitter (0.3 ns), the rise time of the electronic control pulse (0.4 ns), and a resolution of the time tagger (0.16 ns). After correcting for these contributions, the rise time of the coupler switching is estimated to be less than 100 ps, which is compatible with the integrated EOM speed of 10 GHz.

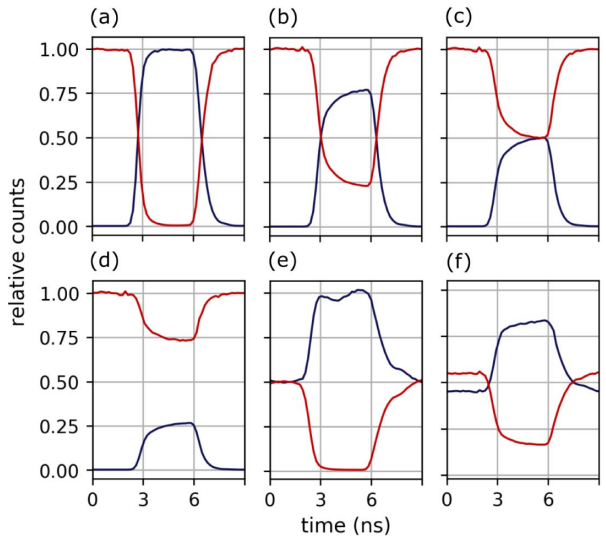


**Fig. 2.** Examples of fast switching with the splitting ratios: (a) $100:0 \rightarrow 0:100$, (b) $100:0 \rightarrow 25:75$, (c) $100:0 \rightarrow 50:50$, (d) $100:0 \rightarrow 75:25$, (e) $50:50 \rightarrow 0:100$, and (f) $55:45 \rightarrow 17:83$. Red and blue data points correspond to two outputs of the interferometer. The error bars are smaller than the data points.

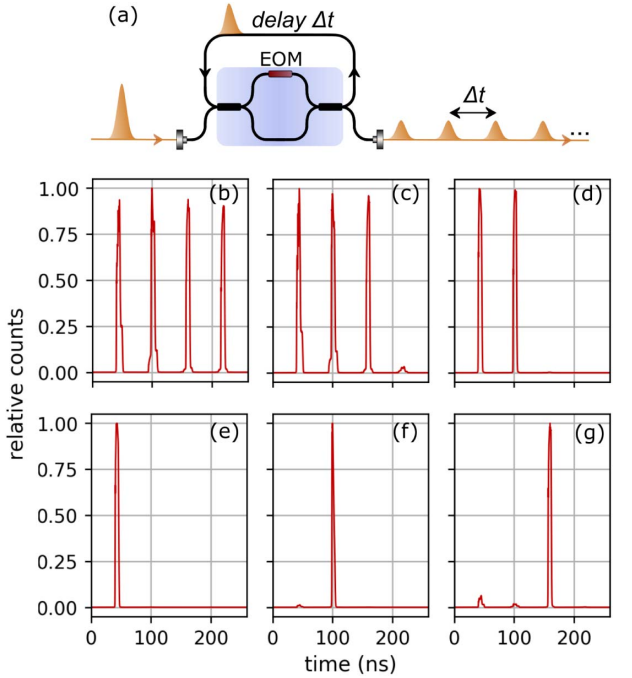


**Fig. 3.** Loop-based temporal multiplexing using the reported switchable coupler: (a) scheme of the experiment and (b)–(g) various configurations of time-bin encoded four-level photonic signal. Particularly, the panel (b) shows the balanced operation suitable for time-multiplexed photon-number-resolving detection.

The input optical pulse can be multiplexed in many time bins when the reflected part of the signal is fed from the output of the coupler to its input to create a loop, as shown in Fig. 3(a). Electronic control pulses applied to the EOM have to be synchronized with the optical pulse repeatedly passing the coupler. This scheme follows the proposal of a time-multiplexed device for photon-number-resolving detectors [19]. Recently, the scheme was experimentally verified, employing a binary switch based on a free-space Pockels cell with the latency of 2.4 μs corresponding to a fiber delay loop length of 480 m [9]. The utilized fixed splitting ratio switching results in non-uniform probability distribution of finding a photon in individual time bins. Employing the tunable coupler reported here, we were able to reach the fully balanced operation and, at the same time, decrease the latency to 60 ns corresponding to a 12 m long fiber, i.e., a direct connection between the output and input pigtails of the coupler.

The reported switching protocol can be generalized to arbitrary time multiplexing. We demonstrate full control over the amplitude of the individual time bins with the mean fidelity of 98.9%. Several examples of the time-bin encoded four-level optical system are depicted in Figs. 3(b)–3(g). The tunable routing of the input signal to the resulting time bins can be complemented by their arbitrary phase modulation using EOMs in both MZI arms. Starting from single-photon input, such routing represents an efficient way of preparing a photonic multi-level system (qudit). A second switchable coupler would be needed for qudit analysis at the receiver.

The overall loss of the coupler and the loop represents the main limitation of a photon-number-resolving loop detector,

as the signal is diminished in each cycle in the loop. The extinction ratio of the coupler determines the minimum probability of releasing a photon before the first full cycle. Here, we have focused on the extinction ratio and latency of the coupler and not performed an extensive loss optimization; hence, the total loss during a single cycle is approximately 80%. It limits the multiplexing to four balanced time bins [Fig. 3(b)]. Using the same fiber architecture with low-loss off-the-shelf components, the total loss could be decreased down to approximately 50%, with the main contribution stemming from the integrated EOM, which corresponds to eight balanced round trips. Further loss reduction is expected with the promising development of integrated phase modulators. Thin-film lithium-niobate EOM with 100 GHz bandwidth and on-chip loss of 0.1 dB was reported recently [20], though further reduction of the fiber-to-chip coupling loss and improvement of the optical bandwidth would be necessary to reach the presented coupler performance. On-chip implementation of optical delay loops required for loop-based detectors and computing represents another significant challenge. Alternatively, a free-space configuration of the whole circuit can be adopted using bulk modulators and delay lines with estimated overall loss slightly below 10%. We estimate time multiplexing to 30–40 of non-saturated *equiprobable* channels to be ultimately possible. It might be challenging, however, to reach very low latency and large electronic bandwidth due to high driving voltage required by bulk electro-optic modulators. Ultimately, the response time can be reduced below 150 ns for discrete switching [6,8].

It is important to stress that the inevitable presence of losses does not prevent utilization of the switchable coupler in a range of single-photon application in the field of quantum technology. Except for a few rare measurement protocols, e.g., conditioning on the vacuum state, the finite efficiency can be corrected for. The quality of the produced quantum state or quantum transformation is not typically decreased by losses, but the rate of the process is affected. Particularly, in applications employing measurement in coincidence basis [21,22], the reported coupler will perform nicely despite its nonzero loss.

We have presented a sub-nanosecond switchable coupler optimized for routing faint optical signals and single photons. The measured overall latency of the coupler is 45 ns with a possibility of reduction below 20 ns, which is comparable with the recovery time of the state-of-the-art single-photon detectors. We have verified full tunability of the splitting ratio from 0:100 to 100:0 with the exceptional extinction of 26 dB and unparalleled long-term stability of one part in 10,000. We have reached for the first time the balanced operation of a loop-based photon-number-resolving detector exploiting full control over the splitting ratio and ultimate stability of the developed coupler. Furthermore, we have demonstrated the deterministic preparation of photonic time-bin four-level qudit with a clock cycle of 60 ns using the presented coupler and a single delay loop. We envision the use of the reported device in advanced feedback-and feedforward-based schemes of electro-optical control of light, where a detection of a fraction of the light signal changes the splitting ratio of the remaining signal. The low-latency switchable coupler is a key device instantly applicable in a vast number of applications such as time-multiplexed single-photon sources [11], photon-number-resolving detectors [9], and various time-bin encoded communication protocols [13], including quantum key distribution [1] and hyper-entangled states preparation and measurement [23].

**Funding.** Grantová Agentura České Republiky (17-26143S); Univerzita Palackého v Olomouci (IGA-PrF-2019-010); Horizon 2020 Framework Programme (QuantERA HYPER-U-P-S,8C18002).

**Disclosures.** The authors declare no conflicts of interest.

## REFERENCES

1. J. M. Lukens, N. T. Islam, C. C. W. Lim, and D. J. Gauthier, Appl. Phys. Lett. **112**, 111102 (2018).
2. Y. Shen, N. C. Harris, S. Skirlo, M. Prabhu, T. Baehr-Jones, M. Hochberg, X. Sun, S. Zhao, H. Larochelle, D. Englund, and M. Soljačić, Nat. Photonics **11**, 441 (2017).
3. Z. Cheng, C. Ríos, W. H. P. Pernice, C. D. Wright, and H. Bhaskaran, Sci. Adv. **3**, e1700160 (2017).
4. A. Schreiber, A. Gábris, P. P. Rohde, K. Laiho, M. Štefaňák, V. Potoček, C. Hamilton, I. Jex, and C. Silberhorn, Science **336**, 55 (2012).
5. K. R. Motes, A. Gilchrist, J. P. Dowling, and P. P. Rohde, Phys. Rev. Lett. **113**, 120501 (2014).
6. Y. He, X. Ding, Z.-E. Su, H.-L. Huang, J. Qin, C. Wang, S. Unsleber, C. Chen, H. Wang, Y.-M. He, X.-L. Wang, W.-J. Zhang, S.-J. Chen, C. Schneider, M. Kamp, L.-X. You, Z. Wang, S. Höfling, C.-Y. Lu, and J.-W. Pan, Phys. Rev. Lett. **118**, 190501 (2017).
7. S. Takeda and A. Furusawa, Phys. Rev. Lett. **119**, 120504 (2017).
8. S. Takeda, K. Takase, and A. Furusawa, Sci. Adv. **5**, eaaw4530 (2019).
9. J. Tiedau, E. Meyer-Scott, T. Nitsche, S. Barkhofen, T. J. Bartley, and C. Silberhorn, Opt. Express **27**, 1 (2019).
10. C. Xiong, X. Zhang, Z. Liu, M. J. Collins, A. Mahendra, L. G. Helt, M. J. Steel, D.-Y. Choi, C. J. Chae, P. H. W. Leong, and B. J. Eggleton, Nat. Commun. **7**, 10853 (2016).
11. G. J. Mendoza, R. Santagati, J. Munns, E. Hemsley, M. Piekarek, E. Martín-López, G. D. Marshall, D. Bonneau, M. G. Thompson, and J. L. O'Brien, Optica **3**, 127 (2016).
12. F. Kaneda and P. G. Kwiat, "High-efficiency single-photon generation via large-scale active time multiplexing," arXiv:1803.04803 (2018).
13. F. Vedovato, C. Agnesi, M. Tomasin, M. Avesani, J.-A. Larsson, G. Vallone, and P. Villoresi, Phys. Rev. Lett. **121**, 190401 (2018).
14. M. A. Hall, J. B. Altepeter, and P. Kumar, Phys. Rev. Lett. **106**, 053901 (2011).
15. D. Pulford, C. Robillard, and E. Huntington, Rev. Sci. Instrum. **76**, 063114 (2005).
16. M. Mičuda, E. Doláková, I. Straka, M. Miková, M. Dušek, J. Fiurášek, and M. Ježek, Rev. Sci. Instrum. **85**, 083103 (2014).
17. M. Miková, H. Fikerová, I. Straka, M. Mičuda, J. Fiurášek, M. Ježek, and M. Dušek, Phys. Rev. A **85**, 012305 (2012).
18. G. Carvacho, J. Cariñe, G. Saavedra, Á. Cuevas, J. Fuenzalida, F. Toledo, M. Figueroa, A. Cabello, J.-Å. Larsson, P. Mataloni, G. Lima, and G. B. Xavier, Phys. Rev. Lett. **115**, 030503 (2015).
19. K. Banaszek and I. A. Walmsley, Opt. Lett. **28**, 52 (2003).
20. C. Wang, M. Zhang, X. Chen, M. Bertrand, A. Shams-Ansari, S. Chandrasekhar, P. Winzer, and M. Lončar, Nature **562**, 101 (2018).
21. F. Flamini, N. Spagnolo, and F. Sciarrino, Rep. Prog. Phys. **82**, 016001 (2019).
22. S. Slussarenko and G. J. Pryde, Appl. Phys. Rev. **6**, 041303 (2019).
23. M. Prilmüller, T. Huber, M. Müller, P. Michler, G. Weihs, and A. Predojević, Phys. Rev. Lett. **121**, 110503 (2018).

# Supplement: Loop-based time multiplexing

Here, we will provide a refined discussion of the time multiplexing schematically depicted in Fig. 5.3. Incident pulse is distributed into $n$ time bins relatively delayed by $\Delta t$, corresponding to the loop delay. Real-time control of MZI transmittance $T(t)$ enables arbitrary intensity distribution of the output pulse train. Indeed, this approach is limited by the loop loss, here expressed as the transmittance $\mu$. The output intensity for $n$-th bin $I_{\mathrm{OUT}}^{(n)}$ reads

$$\begin{aligned} I_{\mathrm{OUT}}^{(1)} &= I_{\mathrm{IN}} T_1 \\ I_{\mathrm{OUT}}^{(n)} &= I_{\mathrm{IN}} \left[1 - T_1\right] \left[1 - T_n\right] \mu^{n-1} \prod_{i=2}^{n-1} T_i \qquad \text{for } n \geq 2, \end{aligned} \tag{5.1}$$

where $T_i$ describes the transmittance for $i$-th time bin, thus $T_i = T\left(t_0 + i\Delta t\right)$ if $t_0$ is the switching time of the first bin. This is a generic model of output

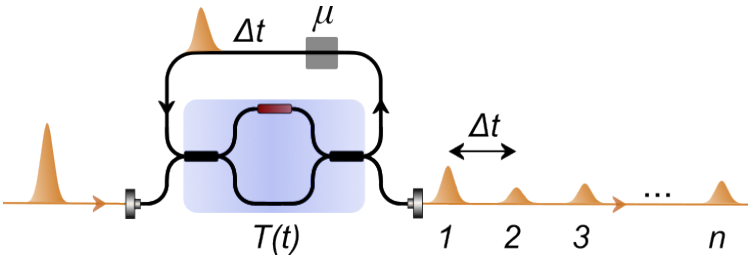


**Figure 5.3:** A scheme of loop-based time multiplexing using a MZI switch with fast control of transmittance $T(t)$. Incident pulse is split between an output and a loop with delay $\Delta t$ and transmittance $\mu$. For each roundtrip of the looped pulse $T(t)$ is modified, therefore an arbitrary train of $n$ pulses is generated.

intensity distribution for given transmittances. However, it does not tell us how to prepare a specific time-bin pattern. To prepare a specific time-bin pattern, we have to first consider that we cannot set $T_i$ directly, but we set a phase in the MZI since

$$T = \frac{\left(1 + V\cos\varphi\right)}{2}. \tag{5.2}$$

We can see that the transmittance setting is limited by the MZI visibility. Using Eqs. (5.2) and (5.1), we can find the corresponding phase settings for the MZI. In practice, we used an iterative algorithm instead of solving these equations analytically. Mainly, we were interested in the regime of the balanced multiplexing where $I_{\mathrm{OUT}}^{(i)}$ = constant for all $i$. For this regime, we

performed an analysis of imperfect phase settings and the limitation of $n$ (number of output pulses) due to setup loss.

This analysis of imperfect phase settings is important for the estimation of the robustness of the protocol since, in real experiments, the phase switching is discretized to a finite number of switching levels. For example, in [1], we controlled the switching voltage by a 6-bit digital attenuator, achieving 64 switching levels. Also, the half-wave voltage of the phase modulation may drift. In Fig. 5.4, we show how non-optimal phase settings influence the balanced time multiplexing. This analysis is done for $\mu = 90\%$, extinction 200:1 and for $n = 8$ (blue), $n = 12$ (orange), and $n = 16$ (green). We simulate the imperfect phase settings by adding a random offset to each $T_i$. The offsets have Gaussian distribution with the standard deviation of 0.07% (left) and 0.7% (right).

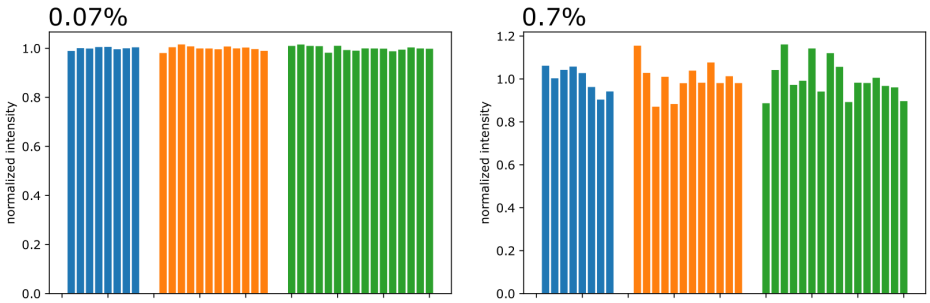


**Figure 5.4:** Non-perfect voltage settings of balanced time multiplexing with $\mu = 90\%$ and extinction 200:1 for $n = 8$ (blue), $n = 12$ (orange), and $n = 16$ (green). This simulation is performed by adding random offsets to the optimal sequence of transmittances. The offsets have Gaussian distribution with the standard deviation of 0.07% (left) and 0.7% (right).

We can observe that the time multiplexing is very sensitive to phase imperfections since even an error smaller than 1% significantly affects the intensity distribution. This is caused mainly by very high (or low) transmittances when the sequence is started. Then, a tiny deviation from the optimal value significantly changes the output intensity. We can see, however, that the error does not increase with the total number of time bins. This is correct if the transmittances are not biased thus the mean value of the imperfect transmittances is equal to the mean value of the perfect transmittances. To satisfy this condition, we have to precisely stabilize the phase. In work [2], we demonstrated a long-term phase stability of 0.05 degrees, which corresponds to the relative phase error of 0.03%. Therefore, our MZI is capable of very precise time multiplexing in this context.

| Loss per cycle $(1-\mu)$ | max cycles | min step $\lvert T_i - T_{i+1}\rvert$ |
|---|---|---|
| 5% | 60 | 0.01 % |
| 10% | 36 | 0.03 % |
| 20% | 20 | 0.06 % |
| 50% | 8 | 0.25 % |
| 90% | 3 | 2.3 % |

**Table 5.1:** The maximum number of the balanced time bins for a given loss per cycle $(1-\mu)$, evaluated for 26 dB extinction. In the third column, a minimal step between neighboring transmittances is computed.

The second type of analysis we performed is how the loss limits the number of balanced time bins. For a given loss, we maximized the number of time bins, and we also evaluated the minimal step between neighboring transmittances $\min(|T_i - T_{i+1}|)$. For this analysis, we used 26 dB extinction of our MZI switch [1]. The results are summarized in Table 5.1. With the increasing loss, the number of time bins rapidly decreases since the loss scales exponentially with the number of roundtrips. Therefore, we were limited to 4 balanced time bins in the work [1]. However, currently, we focus on an alternative approach using free-space switching and a free-space delay line. Although this approach is slower regarding the switching response and the repetition rate (as discussed in Section 3.2.2), it can provide ultra-low losses. Recently, we reached 6.5% of loss per roundtrip, enabling tens of balanced time bins. Also, we developed a way how to switch between 25 partially dependent levels with a single EOM, although conventional free-space switching provides only a few discrete levels. Since the switching levels are very stable and each is continuously adjustable for arbitrary modulation, we aim for at least 12 balanced time bins using this approach.

In the third column of Table 5.1, we show the minimal step between neighboring transmittances $\min(|T_i - T_{i+1}|)$. This parameter is essential for discrete switching, where continuous tuning of each level is impossible. For example, this is the case of a digital attenuation of a driving pulse. Here, the discretization leads to the modulation step of $2^{-b}$ where $b$ is the number of bits. In practice, however, the transmittance step is not equidistant due to the cosine dependence between the phase and transmittance described by Eq. (5.2).

Balanced multiplexing is beneficial especially for photon-number resolving detection. Conventionally, the photon-number resolving detection is performed by splitting the measured state between an array of single-photon detectors. Instead of that, the time multiplexing splits the measured state into

several time windows, using one single-photon detector solely. Additionally, we can combine the path and time multiplexing. Then, the total number of detection channels is given by a product of time and path channels. Therefore, 12 balanced time bins split between an array of 10 detectors provide 120 detection channels.

So far, we have discussed the balanced operation of time multiplexing. However, we can create an almost arbitrary time-bin pattern depending on the properties of the switch and loop, as discussed above. For example, if we perform the time-bin multiplexing of a single-photon state, we prepare a time-bin qudit state

$$|\psi\rangle = \sum_{i=1}^{n} a_i \, |t_i\rangle \,, \tag{5.3}$$

provided we can set a phase for each time bin. This can be easily done by adding an EOM to the output. To demodulate the qudit state, a clone of the time-bin multiplexing device has to be used. To perfectly overlap the neighboring time bins, the mutual phase stability of both loops has to be provided. Alternatively, a single time-multiplexing device can be used twice, once for the qudit preparation and once for the demodulation (measurement).

# Chapter 6

# Fock state conversion

In this chapter, we present theoretical and experimental research in probabilistic Fock state conversion [3]. The conversion is performed by linear optics, with the core element being a feedforward-controlled photonic switch. Firstly, we present a theoretical model of the conversion with the aim of maximizing the conversion efficiency. Secondly, we experimentally demonstrate $|2\rangle \rightarrow |1\rangle$ conversion using an extended version of the photonic switch described in the previous chapter. A resume of the article follows, the full article is enclosed below.

Preparation and controlled manipulation of nonclassical states of light lies at the heart of quantum optics and represents a key tool for the rapidly developing optical quantum technologies. Since the class of experimentally available deterministic unitary operations on quantum states of light is rather limited, it is extremely useful and fruitful to consider also probabilistic conditional operations that significantly extend the scope of quantum states that could be prepared, and transformations that could be implemented. The prime examples of such operations are the conditional single-photon addition and subtraction [76–83].

Here we study the model problem of conversion of a Fock state $|m\rangle$ to a Fock state $|n\rangle$ with $n < m$ by subtraction of $m - n$ photons. We consider a scheme involving $k$ elementary photon subtraction blocks and we demonstrate that the success probability of the scheme is maximized if we actively and adaptively choose a suitable transmittance of the beam splitter in $j$th subtraction block depending on the measurement outcomes of all the previous blocks. We experimentally demonstrate this feedforward-based protocol for the conversion of a two-photon Fock state $|2\rangle$ to the single-photon state $|1\rangle$ using an electronically controlled variable fiber beam splitter formed by a Mach-Zehnder interferometer with electrooptics modulators placed in its

arms [1]. Our measurement results clearly confirm the potential advantage of the feedforward-based photon conversion scheme.

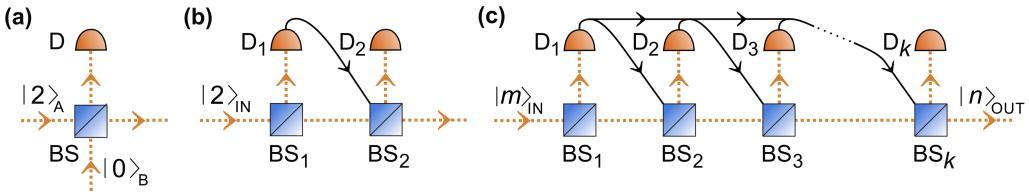


**Figure 6.1:** Fock state conversion schemes. (a) The simplest way of $|2\rangle \rightarrow |1\rangle$ conversion utilizing single beam splitter. (b) Feedforward-enhanced $|2\rangle \rightarrow |1\rangle$ conversion using two beam splitters. (c) Generic scheme for $|m\rangle \rightarrow |n\rangle$ conversion exploiting $k$ beam splitters.

Let us illustrate the protocol principle on a simple case of $|2\rangle$ to $|1\rangle$ conversion. The most straightforward scheme uses one beam splitter and a photon-number-resolving detector, as depicted in Fig. 6.1(a). The conversion is successful if one photon is subtracted at the beam splitter and one photon reaches the output. This occurs maximally in 50% cases for the beam splitter transmittance $T_1 = 0.5$. Now consider we add a second beam splitter with feedforward-controlled transmittance $T_2$ as shown in Fig. 6.1(b). If no photon is subtracted at $\mathrm{BS}_1$, we repeat the subtraction attempt with $\mathrm{BS}_2$ set to $T_2 = 0.5$. However, if one photon is subtracted at $\mathrm{BS}_1$, we activate the feedforward to steer the remaining photon directly to the output ($T_2 = 1$). Indeed, another possibility is that both photons are subtracted at $\mathrm{BS}_1$, leading to unsuccessful conversion. For this reason, $T_1$ in two-step conversion has to be higher than in single-step conversion to reach the maximal probability of success. Specifically, for $T_1 = \frac{2}{3}$ the success probability is maximized to 66.7%.

We can extend the scheme to arbitrary $|m\rangle \rightarrow |n\rangle$ conversion using $k$ subtraction steps. The generic scheme depicted in Fig. 6.1(c) uses all measurement outcomes to optimally set beam splitter transmittances $T_j$. The following explanations illustrate the principles of calculating conversion probabilities. However, for full understanding, we refer the reader to the publication below. The equation describing the probability of success $P(m, n|k)$ reads

$$P(m, n|k) = \sum_{j=0}^{m-n} \binom{m}{j} T_1^{m-j} (1 - T_1)^j P_{\max}(m - j, n|k - 1). \tag{6.1}$$

where $P_{\max}(m, n|k)$ denote the maximum achievable conversion probability. $P_{\max}(m, n|k)$ can be solved by finding roots of the $dT_1$ derivative of Eq. 6.1.

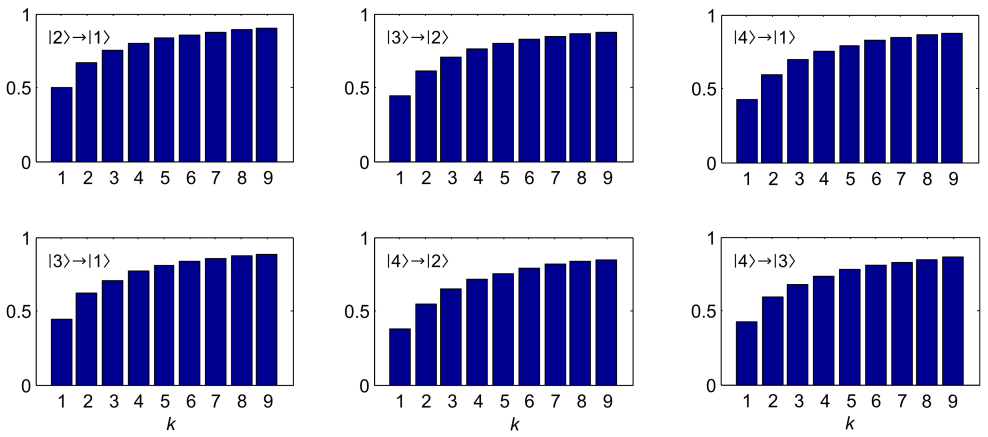


**Figure 6.2:** Optimal photon conversion probabilities $P_{\max}(m, n|k)$ are plotted for 6 combinations of $m$ and $n$.

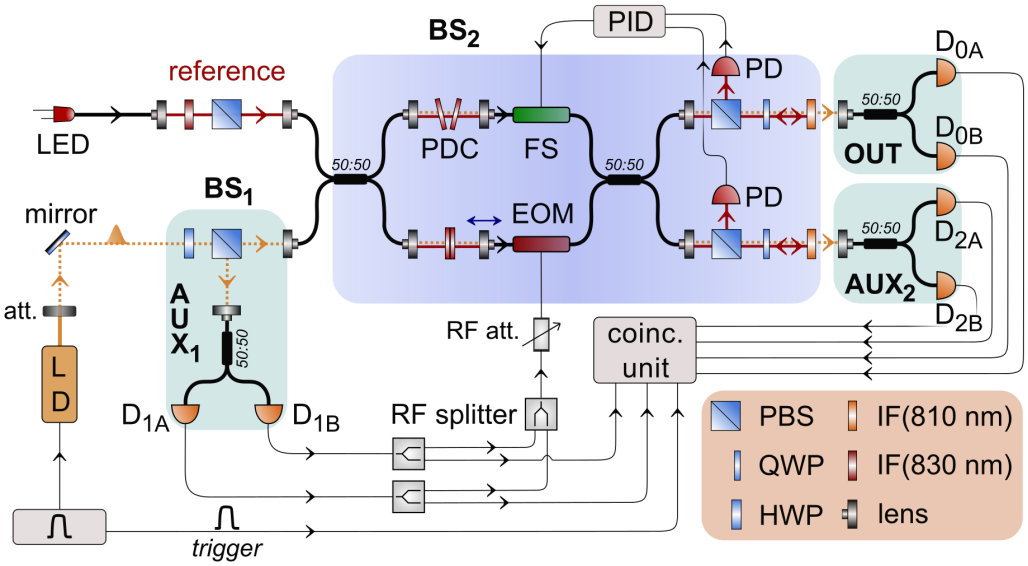


**Figure 6.3:** Experimental setup for feedforward-enhanced $|2\rangle \rightarrow |1\rangle$ conversion. The main optical parts of the setup include a variable beam splitter $BS_1$ and an electrooptically switchable beam splitter $BS_2$ implemented as Mach-Zehnder interferometer. The feedforward control of $BS_2$ is triggered by detection of a photon in the output port $AUX_1$. Legend: laser diode (LD), half-wave plate (HWP), polarization beam splitter (PBS), phase dispersion compensator (PDC), fiber stretcher (FS), electro-optic phase modulator (EOM), quarter-wave plate (QWP), photodiode (PD), single-photon detector (D), interference filter (IF).

The whole process of finding $P_{\max}(m, n|k)$ is iterative, starting from the simplest cases of conversion. In Fig. 6.2, we show maximal conversion probabi-

lities depending on the number of subtraction steps. For 9 conversion steps, the probability of success varies around 85%, depending on the conversion type. Increasing the number of subtraction steps leads to asymptotically deterministic conversion. However, in practice, detection efficiency is finite, and the scheme is affected by losses. As a consequence, the probability of success is smaller than optimal, and the produced output state becomes a mixture of Fock states. Despite these facts, we found out that the scheme remains beneficial even for inefficient detection and for a certain amount of losses. Details are included in the publication below.

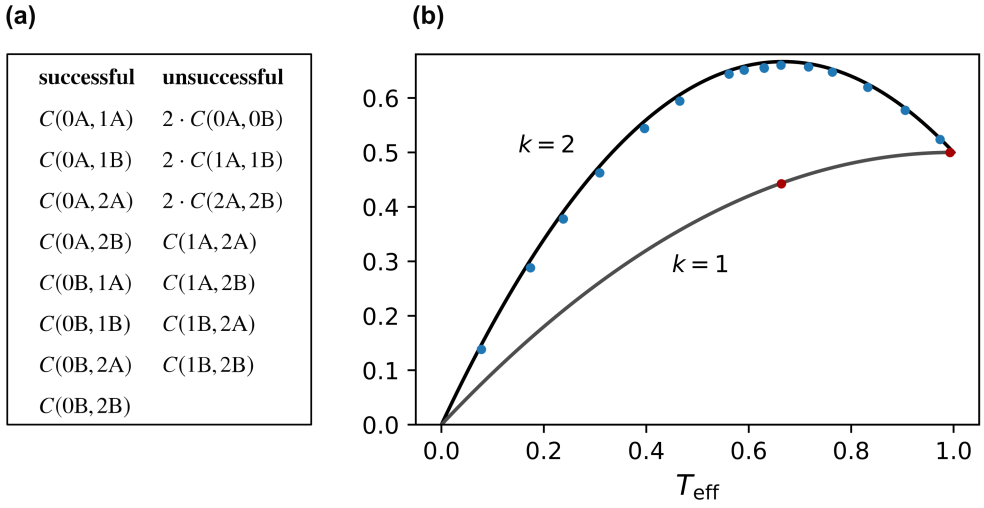


**Figure 6.4:** (a) Table of coincidence tagging, where $C(i, j)$ denotes a coincidence event between detector $\mathrm{D}_i$ and $\mathrm{D}_j$. For neighbouring detectors an event is counted twice, because if two photons reach the same output port $\mathrm{AUX}_1$, $\mathrm{AUX}_2$ or OUT, they trigger the coincidence event only with 50% probability. (b) Experimental results of conversion probability $P_{\mathrm{exp}}(2, 1|k)$ for $k = 1, 2$ depending on effective spitting ratio $T_{\mathrm{eff}}$. Blue dots representing data of feedforward-enhanced conversion $k = 2$ are plotted against the single beam splitter conversion $k = 1$ shown as red dots. Black and grey lines represent upper bounds for the ideal conversion. Error bars are smaller than the point size.

Now let us describe a proof-of-principle experimental demonstration of feedforward-enhanced $|2\rangle \rightarrow |1\rangle$ Fock state conversion as sketched in Fig. 6.1(b). The main aim of our experiment is to verify the feasibility of feedforward-controlled photon subtraction and demonstrate the potential advantage of feedforward-based scheme in comparison to the elementary single-step photon subtraction block in Fig. 6.1(a). The experiment is therefore designed such as to emulate a perfect lossless setup for both schemes. We overcome the

optical losses and finite detection efficiency by effectively balancing the losses in all channels and measuring two-photon coincidence events that indicate either success or failure of the Fock state conversion. We thus postselect only the cases when both input photons reach the single photon detectors and are detected. In this approach, the overall losses are factored out and cancelled in the calculation of the effective success probabilities of both schemes, that are determined as ratios of the measured two-photon coincidence counts. Additionally, the projection onto the two-photon subspace enables us to emulate the two-photon source with a highly attenuated coherent state.

Our experimental setup is depicted in Fig. 6.3. An attenuated laser diode periodically driven by 1 ns pulses at 2 MHz repetition rate produces signal photons at 810 nm. The signal passes through a tunable beam splitter $BS_1$ realized as a sequence of a half-wave plate and a polarization beam splitter. Subsequently, the signal enters a switchable beam splitter $BS_2$ implemented as a Mach-Zehnder interferometer described in the previous chapter. To provide the projection into a two-photon subspace, we need to discriminate at least between Fock states $|2\rangle$ and $|1\rangle$ at each output. We simplify generic photon-number-resolving detection by splitting the signal between two silicon avalanche photodiodes with detection efficiencies around 65%. To trigger the feedforward control of $BS_2$, electronic pulses generated by $D_{1A}$ and $D_{1B}$ are utilized. The pulses are merged, set to $\pi/2$ modulation voltage, and fed into an EOM.

Results of feedforward-enhanced $|2\rangle \rightarrow |1\rangle$ conversion are shown in Fig. 6.4(b). For comparison, we include data of single beam splitter conversion achieved by deactivation of the feedforward. Our results show that the proposed protocol can work experimentally with nearly ideal performance. Extension to arbitrary $|m\rangle \rightarrow |n\rangle$ conversion is possible, provided additional detection multiplexing is implemented. To improve the probability of success, an extension of the experimental setup up to $k$ beam splitters would be necessary. A resource-efficient approach would be reusing single beam splitter for $k$ times in a loop [84, 85]. Although our fiber-based experimental setup is not suitable for cascading due to a high amount of loss, an alternative approach using free-space electrooptic modulator-based switches would be convenient. The loss can be reduced below 10% per cycle, making it practical even without a coincidence basis.

In summary, we have proposed and experimentally demonstrated a feedforward-enhanced scheme for optical Fock state conversion via multiple photon subtraction. In our approach, we use all preceding measurements outcomes to optimally set transmittances of tapping beam splitters. Our findings clearly demonstrate the usefulness and advantages of the presented feedforward-based method.

Research Article | Vol. 28, No. 8 / 13 April 2020 / Optics Express 11634
Optics EXPRESS

# Feedforward-enhanced Fock state conversion with linear optics

VOJTĚCH ŠVARC,* JOSEF HLOUŠEK, MARTINA NOVÁKOVÁ, JAROMÍR FIURÁŠEK, AND MIROSLAV JEŽEK

*Department of Optics, Faculty of Science, Palacký University, 17. listopadu 12, 77146 Olomouc, Czech Republic*
*svarc@optics.upol.cz

**Abstract:** Engineering quantum states of light represents a crucial task in the vast majority of photonic quantum technology applications. Direct manipulation of the number of photons in the light signal, such as single-photon subtraction and addition, proved to be an efficient strategy for the task. Here we propose an adaptive multi-photon subtraction scheme where a particular subtraction task is conditioned by all previous subtraction events in order to maximize the probability of successful subtraction. We theoretically illustrate this technique on the model example of conversion of Fock states via photon subtraction. We also experimentally demonstrate the core building block of the proposal by implementing a feedforward-assisted conversion of two-photon state to a single-photon state. Our experiment combines two elementary photon subtraction blocks where the splitting ratio of the second subtraction beam splitter is affected by the measurement result from the first subtraction block in real time using an ultra-fast feedforward loop. The reported optimized photon subtraction scheme applies to a broad range of photonic states, including highly nonclassical Fock states and squeezed light, advancing the photonic quantum toolbox.



## 1. Introduction

Preparation and controlled manipulation of nonclassical states of light lies at the heart of quantum optics and represents a key tool for the rapidly developing optical quantum technologies. Since the class of experimentally available deterministic unitary operations on quantum states of light is rather limited, it is extremely useful and fruitful to consider also probabilistic conditional operations that significantly extend the scope of quantum states that could be prepared, and transformations that could be implemented. The prime examples of such operations are the conditional single-photon addition and subtraction [1–8]. These elementary operations can be utilized to generate highly non-classical states with negative Wigner function [3,4,8–12], implement various optical quantum gates and operations [13–18], realize probabilistic noiseless quantum amplifiers [19,20], distill continuous-variable entanglement [21–23] or to probe the fundamental properties of quantum mechanics [24,25]. Also many alternative schemes for optical quantum state preparation and manipulation via conditional single-photon or homodyne detection have been proposed and demonstrated [26–30].

Conditional photon subtraction can be performed by sending the light beam at a beam splitter that taps off a part of the signal that is subsequently measured with a single photon detector whose click heralds the photon subtraction. In the experiments one usually employs a highly unbalanced beam splitter to reduce the negative influence of imperfect photon detection with non-unit efficiency $\eta$. This makes the experimental photon subtraction closer to the action of annihilation operator $\hat{a}$, however at the expense of reduced success probability. With the advent of superconducting single-photon detectors and rapidly improved quantum detection efficiencies exceeding 90% [31,32] it nevertheless becomes relevant to investigate also a different regime of

#385609 https://doi.org/10.1364/OE.385609
Journal © 2020 Received 18 Dec 2019; revised 18 Feb 2020; accepted 18 Feb 2020; published 6 Apr 2020

Optics EXPRESS

approximate photon subtraction where one attempts to maximize the success probability by a suitable choice of the transmittances of the tapping beam splitters.

It was shown previously that the success probability of photon subtraction from a travelling beam of light can be increased by a feedforward-controlled loop-based scheme [33,34] where the light beam is repeatedly injected into the photon subtraction device until a subtraction event is detected. This approach enables asymptotically deterministic photon subtraction. The resulting subtraction operation depends on the input state and can be generally expressed as a mixture of quantum filters $t^{k\hat{n}}\hat{a}$ [34], where $\hat{n}$ is the photon number operator, $k$ is the number of loops the light beam has passed until a photon was subtracted, and $|t| < 1$ is the beam splitter amplitude transmittance. In this paper we further investigate the advantages of feedforward-based photon subtraction and we consider general multi-photon subtraction schemes involving a sequence of several elementary photon subtraction blocks, where the transmittance of each tapping beam splitter is controlled by measurement results from all preceding elementary photon subtraction blocks.

Specifically, we study the model problem of conversion of a Fock state $|m\rangle$ to a Fock state $|n\rangle$ with $n < m$ by subtraction of $m-n$ photons. We consider a scheme involving $k$ elementary photon subtraction blocks and we demonstrate that the success probability of the scheme is maximized if we actively and adaptively choose a suitable transmittance of the beam splitter in $j$th subtraction block depending on the measurement outcomes of all the previous blocks. We find that this advantage of feedforward persists even for inefficient detectors and certain amount of optical losses. We experimentally demonstrate this feedforward-based protocol for the conversion of a two-photon Fock state $|2\rangle$ to the single-photon state $|1\rangle$ using an electronically controlled variable fiber beam splitter formed by a Mach-Zehnder interferometer with electrooptics modulators placed in its arms [35]. Our measurement results clearly confirm the potential advantage of the feedforward-based photon conversion scheme.

We note that efficient extraction of a single or several photons from a light beam can be also implemented with the use of quantum light-atoms interactions [36,37]. The interaction of electromagnetic field in a cavity with atoms flying through it may also serve for quantum non-demolition photon counting with applications including observation of progressive quantum state collapse, preparation and stabilization of Fock states of the field and tomographic characterization of the cavity field states [38–41]. The atom based schemes are very promising but also very technologically demanding. Here we instead focus on simple and practicable all-optical setups with the goal to design schemes exhibiting high success probability while requiring only a few tunable beam splitters and single photon detectors.

The rest of the paper is organized as follows. Theoretical description and analysis of the protocol is provided in Section 2. The experimental setup is described in Section 3 where also the experimental results are presented and discussed. Finally, Section 4 contains brief conclusions.

## 2. Theory

Here we present theoretical derivation of optimal feedforward-based schemes for conversion of optical Fock state $|m\rangle$ to Fock state $|n\rangle$ via subtraction of $m-n$ photons. We first describe the method on the illustrative example of conversion of a two-photon Fock state $|2\rangle$ to the single-photon state $|1\rangle$ and then generalize the procedure to arbitrary $|m\rangle \rightarrow |n\rangle$ conversion with $m > n$. The $|2\rangle \rightarrow |1\rangle$ conversion can be accomplished by single photon subtraction, whose simplest instance is depicted in Fig. 1(a). The input Fock state $|2\rangle$ impinges on a beam splitter with amplitude transmittance $t$ and reflectance $r$, where it is transformed into an entangled state of output spatial modes A and B,

$$|2\rangle_A|0\rangle_B \rightarrow t^2|2\rangle_A|0\rangle_B + \sqrt{2}tr|1\rangle_A|1\rangle_B + r^2|0\rangle_A|2\rangle_B. \quad (1)$$

Optics EXPRESS

The output auxiliary mode B is measured with a photon number resolving detector. The conversion is successful if a single photon is detected, which occurs with probability $P(2,1) = 2T(1-T)$, where $T = t^2 = 1 - r^2$. This probability is maximized for $T = \frac{1}{2}$ and we get $P_{\max}(2,1) = \frac{1}{2}$. If the detector on output mode B detects two photons, then the input state is destroyed and cannot be recovered. However, if no photons are detected, then we know that the output state of mode A is still the two-photon Fock state $|2\rangle$ and we can attempt to repeat the photon subtraction. The resulting feedforward-enhanced scheme is shown in Fig. 1(b). A second beam splitter and detector are placed after the first beam splitter, and the transmittance of the second beam splitter is controlled by the feedforward signal from the first detector. Let $T_1$ and $T_2$ denote the intensity transmittances of the first and second beam splitter, respectively. If the first detector detects one photon, then $T_2$ is set to 1. On the other hand, if the first detector detects no photons, then $T_2$ is set to $\frac{1}{2}$. The overall success probability of this two-stage conversion scheme reads

$$P(2,1|2) = T_1^2 \times \frac{1}{2} + 2T_1(1-T_1) \times 1 = 2T_1 - \frac{3}{2}T_1^2. \tag{2}$$

This probability is maximized for $T_1 = \frac{2}{3}$, and we get $P_{\max}(2,1|2) = \frac{2}{3}$.

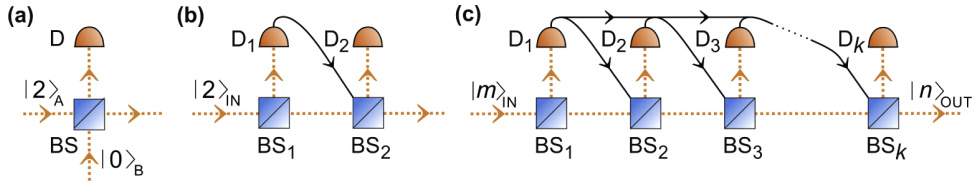


**Fig. 1.** Fock state conversion schemes. (a) The simplest way of $|2\rangle \rightarrow |1\rangle$ conversion utilizing single beam splitter. (b) Feedforward-enhanced $|2\rangle \rightarrow |1\rangle$ conversion using two beam splitters. (c) Generic scheme for $|m\rangle \rightarrow |n\rangle$ conversion exploiting $k$ beam splitters.

We now present a generic protocol for $k$-step conversion of Fock state $|m\rangle$ to Fock state $|n\rangle$, where $m > n$ and $k \geq 1$ denotes the number of elementary photon subtraction steps. The scheme is illustrated in Fig. 1(c) where the transmittance $T_j$ of beam splitter $\mathrm{BS}_j$ is controlled by the measurement outcomes of all preceding detectors $\mathrm{D}_l$, $l < j$. Let $P_{\max}(m,n|k)$ denote the maximum achievable conversion probability with $k$ steps. Suppose that we have found all optimal probabilities $P_{\max}(m-j,n|k-1)$. Considering the scheme in Fig. 1(c) as a combination of the first beam splitter and detector and a block performing optimal feedforward controlled conversion with $k-1$ steps, we can write

$$P(m,n|k) = \sum_{j=0}^{m-n} \binom{m}{j} T_1^{m-j}(1-T_1)^j P_{\max}(m-j,n|k-1). \tag{3}$$

The optimal transmittance $T_1$ can be determined by finding roots of the polynomial

$$\frac{dP(m,n|k)}{dT_1} = 0 \tag{4}$$

and choosing the root that lies in the interval $[0,1]$ and maximizes $P(m,n|k)$. Explicitly, the polynomial equation reads

$$\sum_{j=0}^{m-n} \binom{m}{j} T_1^{m-j-1}(1-T_1)^{j-1}[(m-j)(1-T_1) - jT_1]P_{\max}(m-j,n|k-1) = 0. \tag{5}$$

There are $n-1$ non-optimal roots $T_1 = 0$ and if we divide the Eq. (5) by $T_1^{n-1}$ we end up with a polynomial equation of order $m-n$ that can be solved either numerically or even analytically for $m-n \leq 4$.

Optics EXPRESS

The optimal probability $P_{\max}(m,n|k)$ can be calculated iteratively. It is useful to formally define $P_{\max}(m,n|0) = 0$, $m > n > 0$, and we also have that $P_{\max}(m,m|k) = 1$. Specifically, we first determine $P_{\max}(n+1,n|j)$ starting from $j = 1$ and proceeding up to $j = k$. We then continue with determination of $P_{\max}(n+2,n|j)$, $1 \le j \le k$, and we repeat the whole calculation for all $P_{\max}(n+l,n|j)$ with increasing $l$ until we reach $n + l = m$. In Fig. 2 we plot the optimal probabilities $P_{\max}(m,n|k)$ for 6 combinations of $m$ and $n$ and for up to 9 subtraction steps. We can see that the conversion probability increases with the number of steps $k$ and asymptotically approaches 1.

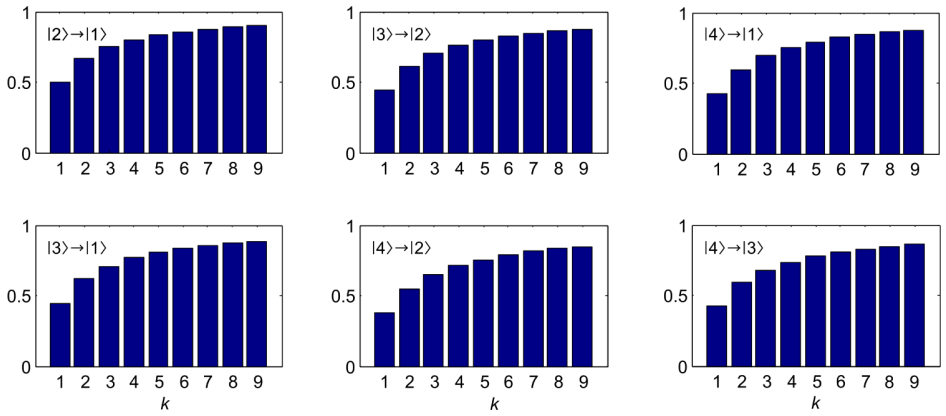


**Fig. 2.** Optimal photon conversion probabilities $P_{\max}(m,n|k)$ are plotted for 6 combinations of $m$ and $n$.

Imperfect single photon detectors with non-unit detection efficiency $\eta$ will lead to production of mixtures of various Fock states. The errors in conditional single photon subtraction due to imperfect detection can be reduced by using highly unbalanced beam splitter at the expense of reducing the overall success probability of the protocol. Since we here instead study the regime that maximizes the probability of state conversion, imperfect detection will unavoidably play a role. Let us illustrate this on the above considered example of $|2\rangle \rightarrow |1\rangle$ conversion. Remarkably, the normalized conditional output state $\rho_{\text{out}}$ is the same for both single-step conversion with $T_1 = \frac{1}{2}$ and two-step conversion with $T_1 = \frac{2}{3}$ and $T_2 = \frac{1}{2}$ or $T_2 = 1$,

$$\rho_{\text{out}} = \frac{1}{2-\eta}|1\rangle\langle 1| + \frac{1-\eta}{2-\eta}|0\rangle\langle 0|. \tag{6}$$

The overall probabilities of state preparation for the single- and two-step schemes exhibit similar dependence on $\eta$,

$$P(2,1|1,\eta) = \frac{1}{2}\eta(2-\eta), \qquad P(2,1|2,\eta) = \frac{2}{3}\eta(2-\eta), \tag{7}$$

however with different prefactors. This shows that the advantage of feedforward-based scheme is preserved even for inefficient detection. Specifically, for a given output state quality we may achieve higher state preparation probability with feedforward.

Since the feedforward-controlled switchable beam splitter will in practice introduce additional optical losses, we now investigate a more refined model of the setup in Fig. 1(b) with a lossy channel with transmittance $\eta_O$ inserted in between the beam splitters $BS_1$ and $BS_2$, see inset in Fig. 3(b). We assume that $\eta_O$ is constant and does not depend on the setting of the transmittance of $BS_2$, which is well justified for setups based on interferometric schemes with feedforward-controlled electrooptic modulators. In order to compare the feedforward-based scheme with the elementary

Optics EXPRESS

photon subtraction block in Fig. 1(a), we again consider the $|2\rangle \rightarrow |1\rangle$ Fock state conversion and we investigate the trade-off between the state conversion probability $P(2,1)$ and the single-photon fraction $p_1$ in the conditionally generated output state $\rho_{\text{out}} = p_1|1\rangle\langle 1| + (1-p_1)|0\rangle\langle 0|$. For the elementary photon subtraction block in Fig. 1(a) we get a simple parametric dependence of $P(2,1)$ and $p_1$ on the transmittance $T$ of beam splitter BS,

$$P(2,1) = 2\eta(1-T)[1-(1-T)\eta], \qquad p_1 = \frac{T}{1-(1-T)\eta}. \tag{8}$$

For $\eta \geq \frac{1}{2}$ the maximum achievable probability of state conversion is $\frac{1}{2}$, achieved for $T = 1 - \frac{1}{2\eta}$. At this point, $p_1 = 2 - \frac{1}{\eta}$. For $\eta < \frac{1}{2}$ the maximum probability reads $2\eta(1-\eta)$, which is however approached in the undesirable limit $T \rightarrow 0$, when also $p_1 \rightarrow 0$. On the other hand, in the limit $T \rightarrow 1$ also $p_1 \rightarrow 1$ but at the cost of vanishing success probability, $P(2,1) \rightarrow 0$, a well-known limit of the standard photon subtraction scheme. The trade-off between P(2,1) and $p_1$ for the elementary photon subtraction block is plotted in Fig. 3 as blue solid line for two different $\eta$. The choice $\eta = 60\%$ corresponds to detection of photons with (an array of) ordinary avalanche photodiodes while $\eta = 0.85\%$ illustrates the performance for highly efficient detectors such as superconducting single photon detectors.

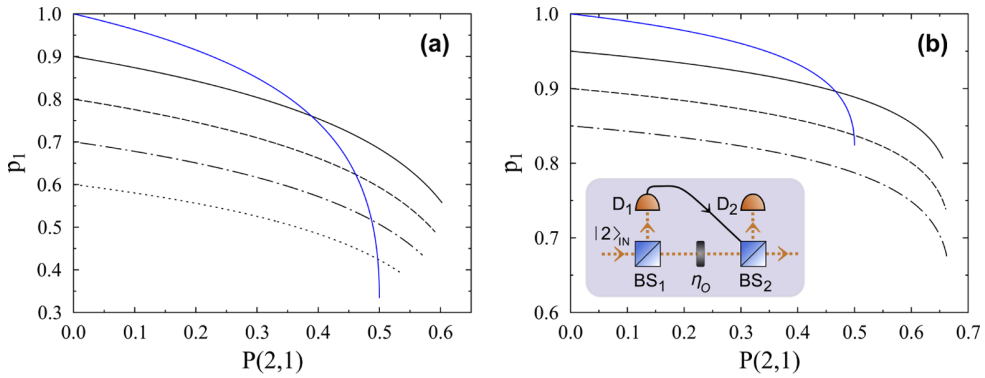


**Fig. 3.** Trade-off between probability of $2 \rightarrow 1$ Fock state conversion $P(2,1)$ and the single-photon fraction $p_1$ in the output state is displayed for two different detection efficiencies $\eta = 0.6$ (a) and $\eta = 0.85$ (b). The blue solid line represents result for the elementary photon subtraction block in Fig. 1(a). Black lines show results of the feedforward-based scheme with additional optical losses quantified by the effective transmittance $\eta_0$. The various lines in panel (a) correspond to $\eta_O = 0.9$ (solid line), 0.8 (dashed line), 0.7 (dot-dashed line) and 0.6 (dotted line) while the lines on panel (b) are plotted for $\eta_O = 0.95$ (solid line), 0.9 (dashed line) and 0.85 (dash-dotted line). The inset in panel (b) shows the optical model of the feedforward-based scheme with included optical losses of the switchable beam splitter $BS_2$.

For the feedforward-based scheme with additional optical losses where the transmittance of $BS_2$ is actively switched between $T_2$ and 1, we obtain

$$P(2,1) = 2\eta\left\{1 - T_1 - \eta + \eta T_1[2 - T_1 - \eta_O(1-T_2)(1 - T_1 + \eta_O T_1(1-T_2))] + \eta_O T_1(1-T_2)\right\},$$

$$p_1 = \frac{\eta_O T_1[1 - T_1 + \eta_O T_1 T_2(1-T_2)]}{1 - T_1 - \eta + \eta T_1[2 - T_1 - \eta_O(1-T_2)(1 - T_1 + \eta_O T_1(1-T_2))] + \eta_O T_1(1-T_2)}. \tag{9}$$

For any given $\eta$, $\eta_O$ and target conversion probability $P(2,1)$ we numerically optimize $T_1$ and $T_2$ to achieve maximum single-photon fraction $p_1$ in the output state. The results of numerical

Optics EXPRESS

optimization are plotted in Fig. 3 for two different detection efficiencies $\eta$ and several different levels of added optical loss. The maximum achievable single-photon fraction is limited by the additional optical losses, $p_1 \leq \eta_O$. If $\eta_O(3\eta - 1) \geq 1$, then the maximum conversion probability reads $P_{\max}(2, 1) = \frac{2}{3}$, and is obtained for

$$T_1 = \frac{3\eta - 1}{3\eta}, \qquad T_2 = 1 - \frac{1}{\eta_O(3\eta - 1)}. \tag{10}$$

The single photon fraction achieved at this point reads

$$p_1 = 2\eta_O - \frac{1 + 2\eta_O}{3\eta}. \tag{11}$$

The graphs in Fig. 3 indicate that the feedforward-based scheme becomes advantageous provided that $\eta_O \gtrsim \eta$, i.e. the additional optical losses should be comparable to or smaller than the effective losses in single-photon detection. In our proof-of-principle fiber-based experiment at 810 nm reported below, the losses imposed by electrooptic modulators and other optical components result in $\eta_O \lesssim 20\%$. However, an alternative approach using free-space electrooptic modulator based switches could reduce losses below 10%, yielding $\eta_O \gtrsim 90\%$, making the scheme applicable in practice.

## 3. Experiment

In this Section we report on a proof-of-principle experimental demonstration of feedforward-enhanced $|2\rangle \rightarrow |1\rangle$ Fock state conversion as sketched in Fig. 1(b). The main aim of our experiment is to verify the feasibility of feedforward-controlled photon subtraction and demonstrate the potential advantage of feedforward-based scheme in comparison to the elementary single-step photon subtraction block in Fig. 1(a). The experiment is therefore designed such as to emulate a perfect lossless setup for both schemes. We overcome the optical losses and finite detection efficiency by effectively balancing the losses in all channels and measuring two-photon coincidence events that indicate either success or failure of the Fock state conversion. We thus postselect only the cases when both input photons reach the single photon detectors and are detected. In this approach, the overall losses are factored out and cancelled in the calculation of the effective success probabilities of both schemes, that are determined as ratios of the measured two-photon coincidence counts. Additionally, the projection onto the two-photon subspace enables us to emulate the two-photon source with a highly attenuated coherent state.

Our experimental setup is depicted in Fig. 4. An attenuated laser diode periodically driven by 1 ns pulses at 2 MHz repetition rate produces signal photons at 810 nm. The signal passes through tunable beam splitter $BS_1$ realized as a sequence of a half-wave plate and a polarization beam splitter. Subsequently, the signal enters switchable beam splitter $BS_2$ implemented as a Mach-Zehnder interferometer (MZI) with a 10 GHz integrated electro-optic phase modulator PM-0K5-10-PFU-PFU-810-UL from EOSpace (EOM), enabling low-voltage and low-latency switching performance [35]. While the phase control is performed in an 8 m long MZI part formed of polarization-maintaining fibers, precise arm balancing, and dispersion compensation are done in 1 m long air gap. As a result, we reach the interference visibility 99.55% enabling the switching with extinction greater than 400:1. The MZI has an overall transmission of $\sim 20\%$. Due to the presence of environmentally induced phase fluctuations in MZI, an active phase-lock is implemented. It exploits auxiliary light at 830 nm acting as a phase reference. Particularly, we use a single-mode coupled luminescent diode with additional polarization and spectral filtering resulting in 3 nm bandwidth and power of 100 pW. The reference and the signal are merged and co-propagate through the MZI. Subsequently, at the outputs, the wavelengths are separated with a sequence of a polarizing beam splitter, a quarter-wave plate, and an interference filter acting

Optics EXPRESS

together as an optical isolator. Phase fluctuations are monitored with ultra-sensitive photodiodes, evaluated with a custom-made analog proportional-integral-derivative (PID) controller, and compensated with a fiber stretcher performing at 1 kHz bandwidth and dynamic range of 35 $\mu$m. Our technique provides continuous tunability and sub-degree stability of the phase.

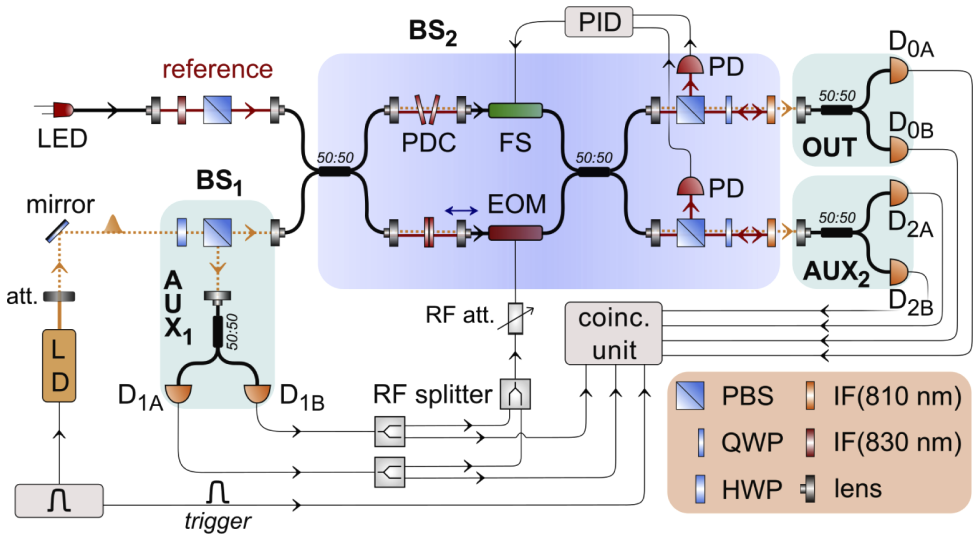


**Fig. 4.** Experimental setup for feedforward-enhanced $|2\rangle \rightarrow |1\rangle$ Fock state conversion. The main optical parts of the setup include a variable beam splitter $BS_1$ and an electrooptically switchable beam splitter $BS_2$ implemented as Mach-Zehnder interferometer. The feedforward control of $BS_2$ is triggered by detection of a photon in the output port $AUX_1$. Legend: laser diode (LD), half-wave plate (HWP), polarization beam splitter (PBS), phase dispersion compensator (PDC), fiber stretcher (FS), electro-optic phase modulator (EOM), quarter-wave plate (QWP), photodiode (PD), single-photon detector (D), interference filter (IF).

To provide the projection into two-photon subspace we need to discriminate at least between Fock states $|2\rangle$ and $|1\rangle$ at each output. We simplify generic photon number resolving detection by splitting the signal between two silicon avalanche photo-diodes with detection efficiencies around 65%. However, compared to the ideal photon number resolving detection we can discriminate the Fock state $|2\rangle$ only with 50% probability, which we take into account in data analysis. To provide balanced detection we optimize the setup to achieve equal click probabilities for neighbouring detectors $D_{jA}$ and $D_{jB}$. Since loss in $AUX_1$ port is much smaller than loss induced by $BS_2$ we modify the splitting ratio of $BS_1$ in order to compensate the imbalance. This approach is equivalent to imposing an additional artificial loss in the $AUX_1$ port. It is then relevant to evaluate the effective splitting ratio of $BS_1$ as the ratio of the signal detected at $AUX_2$ and OUT ports to signal detected at $AUX_1$ port. Particularly, we determine the effective transmittance $T_{\mathrm{eff}}$ of $BS_1$ as $(N_{0A} + N_{0B} + N_{2A} + N_{2B})/(N_{0A} + N_{0B} + N_{1A} + N_{1B} + N_{2A} + N_{2B})$ where $N_i$ denotes count rate at detector $D_i$. In our experiment, $T_{\mathrm{eff}}$ acts the same way as $T_1$ in the lossless case described by Eq. (2). To trigger the feedforward control of $BS_2$, electronic pulses generated by $D_{1A}$ and $D_{1B}$ are utilized. The pulses are merged, set to $\pi/2$ modulation voltage and fed into EOM. To reach the same shape and timing of the pulses, discriminators and delay lines are used (not shown in the scheme).

For data collection and processing, a custom made 16-channel coincidence unit is utilized [42]. To avoid random detection events, the measurement is triggered by the laser diode driving pulse. We detect all of the possible 15 combinations of two-coincidences as listed in Fig. 5(a). A

Optics EXPRESS

coincidence event is tagged as *successful* if one photon of the pair is detected at the output signal port OUT, while the other photon is heralded at $AUX_1$ or $AUX_2$ port. All other coincidence events are tagged as *unsuccessful*. Events discriminated only with 50% probability are counted with double rate. The effective success probability of conversion is then determined as the ratio of successful coincidence counts to all coincidence counts. The input coherent state contains a small amount of higher photon-number states that may be falsely indicated as two-coincidences and influence the results. Evaluating higher-order coincidences we estimate that spurious two-coincidences form ~1% of the signal causing a relative error of 0.4% in the worst case. Further reduction of the error is achievable by additional attenuation of the signal source, however, at the expense of a decreased rate of the two-photon state.

**(a)**

| successful | unsuccessful |
|---|---|
| $C(0A,1A)$ | $2 \cdot C(0A,0B)$ |
| $C(0A,1B)$ | $2 \cdot C(1A,1B)$ |
| $C(0A,2A)$ | $2 \cdot C(2A,2B)$ |
| $C(0A,2B)$ | $C(1A,2A)$ |
| $C(0B,1A)$ | $C(1A,2B)$ |
| $C(0B,1B)$ | $C(1B,2A)$ |
| $C(0B,2A)$ | $C(1B,2B)$ |
| $C(0B,2B)$ | |

**(b)**

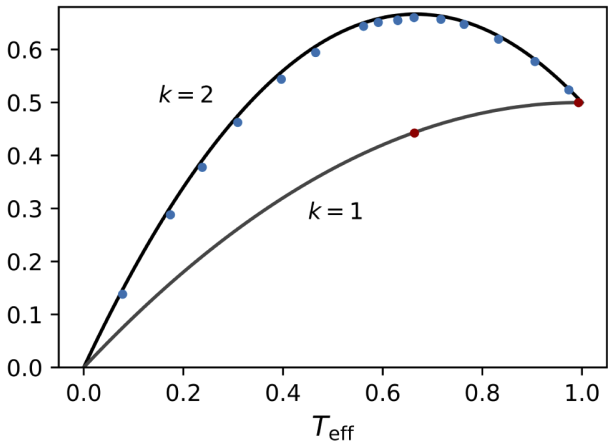


**Fig. 5.** (a) Table of coincidence tagging, where $C(i,j)$ denotes a coincidence event between detector $D_i$ and $D_j$. For neighbouring detectors an event is counted twice, because if two photons reach the same output port $AUX_1$, $AUX_2$ or OUT, they trigger the coincidence event only with 50% probability. (b) Experimental results of conversion probability $P_{exp}(2,1|k)$ for $k = 1, 2$ depending on effective spitting ratio $T_{eff}$. Blue dots representing data of feedforward-enhanced conversion $k = 2$ are plotted against the single beam splitter conversion $k = 1$ shown as red dots. Black and grey lines represent upper bounds for the ideal conversion. Error bars are smaller than the point size.

Results of feedforward-enhanced $|2\rangle \rightarrow |1\rangle$ conversion are shown in Fig. 5(b). For comparison, we include data of single beam splitter conversion achieved by deactivation of the feedforward. According to Eq. (2), the best possible performance $P_{max}(2,1|2) = 66.7\%$ is predicted for $T_1 = 66.7\%$. Experimentally we reach a very close value of $P_{exp}(2,1|2) = (66.0 \pm 0.1)\%$ for $T_{eff} = (66.30 \pm 0.05)\%$. Error caused by spurious coincidences is estimated as 0.2%.

Our results show that the proposed protocol can work experimentally with nearly ideal performance. Extension to arbitrary $|m\rangle \rightarrow |n\rangle$ conversion is possible, provided additional detection multiplexing would be used. To improve the probability of success, an extension of the experimental setup up to $k$ beam splitters would be necessary. A resource-efficient approach would be reusing single beam splitter for $k$ times in a loop [33,34]. Although our fiber-based experimental setup is not suitable for cascading due to a high amount of loss, an alternative approach using free-space electrooptic modulator based switches would be convenient. The loss can be reduced below 10% per cycle, making it practical even without the need of a coincidence basis. The limitation of this approach is the higher latency of the feedforward estimated to tens of nanoseconds ultimately [43–45].

Optics EXPRESS

## 4. Conclusion

In summary, we have proposed and experimentally demonstrated a feedforward-enhanced scheme for optical Fock state conversion via photon subtraction. In our approach, the transmittances of tapping beam splitters are controlled by all procedening measurement outcomes to maximize the success probability of photon subtraction for a given setup complexity, i.e. a given maximum number of elementary photon subtraction blocks. Our results for $|2\rangle \rightarrow |1\rangle$ conversion are directly applicable to single photon subtraction from a single-mode weakly squeezed vacuum state that can be approximated as $|0\rangle + \epsilon|2\rangle$, since the dominant vacuum term does not contribute to the subtraction. Our findings clearly demonstrate the usefulness and advantages of the presented feedforward-based method, which can be utilized for an arbitrary input state. Note however, that for input superpositions of Fock states, the output state would depend on the overall transmittance of the beam splitters hence a mixed state would be generated even with perfect detection. In such case one could investigate the trade-off between state preparation quality, as quantified e.g. by state fidelity, and success probability of the protocol and choose the most suitable operating point.

## Funding

Grantová Agentura České Republiky (19-19189S); Univerzita Palackého v Olomouci (IGA-PrF-2019-010).

## Acknowledgments

We thank Michal Dudka for the development and implementation of custom electronics.

## Disclosures

The authors declare that there are no conflicts of interest related to this article.

## References

1. J. Wenger, R. Tualle-Brouri, and P. Grangier, "Non-Gaussian statistics from individual pulses of squeezed light," Phys. Rev. Lett. **92**(15), 153601 (2004).
2. A. Zavatta, S. Viciani, and M. Bellini, "Quantum-to-classical transition with single-photon-added coherent states of light," Science **306**(5696), 660–662 (2004).
3. A. Ourjoumtsev, R. Tualle-Brouri, J. Laurat, and P. Grangier, "Generating optical Schrödinger kittens for quantum information processing," Science **312**(5770), 83–86 (2006).
4. J. Neergaard-Nielsen, B. Nielsen, C. Hettich, K. Mølmer, and E. Polzik, "Generation of a superposition of odd photon number states for quantum information networks," Phys. Rev. Lett. **97**(8), 083604 (2006).
5. K. Wakui, H. Takahashi, A. Furusawa, and M. Sasaki, "Photon subtracted squeezed states generated with periodically poled KTiOPO 4," Opt. Express **15**(6), 3568–3574 (2007).
6. N. Namekata, Y. Takahashi, G. Fujii, D. Fukuda, S. Kurimura, and S. Inoue, "Non-Gaussian operation based on photon subtraction using a photon-number-resolving detector at a telecommunications wavelength," Nat. Photonics **4**(9), 655–660 (2010).
7. M. Bellini and A. Zavatta, "Manipulating light states by single-photon addition and subtraction," in *Prog. Optics*, vol. 55 (Elsevier, 2010), pp. 41–83.
8. T. Gerrits, S. Glancy, T. S. Clement, B. Calkins, A. E. Lita, A. J. Miller, A. L. Migdall, S. W. Nam, R. P. Mirin, and E. Knill, "Generation of optical coherent-state superpositions by number-resolved photon subtraction from the squeezed vacuum," Phys. Rev. A **82**(3), 031802 (2010).
9. A. Ourjoumtsev, F. Ferreyrol, R. Tualle-Brouri, and P. Grangier, "Preparation of non-local superpositions of quasi-classical light states," Nat. Phys. **5**(3), 189–192 (2009).
10. J. Neergaard-Nielsen, M. Takeuchi, K. Wakui, H. Takahashi, K. Hayasaka, M. Takeoka, and M. Sasaki, "Optical continuous-variable qubit," Phys. Rev. Lett. **105**(5), 053602 (2010).
11. O. Magana-Loaiza, R. d. J. Leon-Montiel, A. Perez-Leija, A. URen, C. You, K. Busch, A. Lita, S. Nam, R. Mirin, and T. Gerrits, "Multiphoton Quantum-State Engineering using Conditional Measurements," arXiv preprint arXiv:1901.00122 (2019).
12. M. Cooper, L. J. Wright, C. Söller, and B. J. Smith, "Experimental generation of multi-photon Fock states," Opt. Express **21**(5), 5309–5317 (2013).
13. J. Fiurášek, "Engineering quantum operations on traveling light beams by multiple photon addition and subtraction," Phys. Rev. A **80**(5), 053822 (2009).

Optics EXPRESS


14. P. Marek and J. Fiurášek, "Elementary gates for quantum information with superposed coherent states," Phys. Rev. A **82**(1), 014304 (2010).
15. A. Tipsmark, R. Dong, A. Laghaout, P. Marek, M. Ježek, and U. Andersen, "Experimental demonstration of a Hadamard gate for coherent state qubits," Phys. Rev. A **84**(5), 050301 (2011).
16. R. Blandino, F. Ferreyrol, M. Barbieri, P. Grangier, and R. Tualle-Brouri, "Characterization of a $\pi$-phase shift quantum gate for coherent-state qubits," New J. Phys. **14**(1), 013017 (2012).
17. A. Coelho, L. Costanzo, A. Zavatta, C. Hughes, M. Kim, and M. Bellini, "Universal continuous-variable state orthogonalizer and qubit generator," Phys. Rev. Lett. **116**(11), 110501 (2016).
18. L. Costanzo, A. Coelho, N. Biagi, J. Fiurášek, M. Bellini, and A. Zavatta, "Measurement-induced strong Kerr nonlinearity for weak quantum states of light," Phys. Rev. Lett. **119**(1), 013601 (2017).
19. A. Zavatta, J. Fiurášek, and M. Bellini, "A high-fidelity noiseless amplifier for quantum light states," Nat. Photonics **5**(1), 52–56 (2011).
20. M. Usuga, C. Müller, C. Wittmann, P. Marek, R. Filip, C. Marquardt, G. Leuchs, and U. Andersen, "Noise-powered probabilistic concentration of phase information," Nat. Phys. **6**(10), 767–771 (2010).
21. A. Ourjoumtsev, A. Dantan, R. Tualle-Brouri, and P. Grangier, "Increasing entanglement between Gaussian states by coherent photon subtraction," Phys. Rev. Lett. **98**(3), 030502 (2007).
22. H. Takahashi, J. Neergaard-Nielsen, M. Takeuchi, M. Takeoka, K. Hayasaka, A. Furusawa, and M. Sasaki, "Entanglement distillation from Gaussian input states," Nat. Photonics **4**(3), 178–181 (2010).
23. Y. Kurochkin, A. S. Prasad, and A. Lvovsky, "Distillation of the two-mode squeezed state," Phys. Rev. Lett. **112**(7), 070402 (2014).
24. V. Parigi, A. Zavatta, M. Kim, and M. Bellini, "Probing quantum commutation rules by addition and subtraction of single photons to/from a light field," Science **317**(5846), 1890–1893 (2007).
25. A. Zavatta, V. Parigi, M. Kim, H. Jeong, and M. Bellini, "Experimental demonstration of the bosonic commutation relation via superpositions of quantum operations on thermal light fields," Phys. Rev. Lett. **103**(14), 140406 (2009).
26. S. A. Babichev, B. Brezger, and A. I. Lvovsky, "Remote preparation of a single-mode photonic qubit by measuring field quadrature noise," Phys. Rev. Lett. **92**(4), 047903 (2004).
27. E. Bimbard, N. Jain, A. MacRae, and A. Lvovsky, "Quantum-optical state engineering up to the two-photon level," Nat. Photonics **4**(4), 243–247 (2010).
28. K. Huang, H. Le Jeannic, J. Ruaudel, V. B. Verma, M. D. Shaw, F. Marsili, S. W. Nam, E. Wu, H. Zeng, Y.-C. Jeong, R. Filip, O. Morin, and J. Laurat, "Optical synthesis of large-amplitude squeezed coherent-state superpositions with minimal resources," Phys. Rev. Lett. **115**(2), 023602 (2015).
29. M. Yukawa, K. Miyata, T. Mizuta, H. Yonezawa, P. Marek, R. Filip, and A. Furusawa, "Generating superposition of up-to three photons for continuous variable quantum information processing," Opt. Express **21**(5), 5529–5535 (2013).
30. D. V. Sychev, A. E. Ulanov, A. A. Pushkina, M. W. Richards, I. A. Fedorov, and A. I. Lvovsky, "Enlargement of optical Schrödinger's cat states," Nat. Photonics **11**(6), 379–382 (2017).
31. F. Marsili, V. B. Verma, J. A. Stern, S. Harrington, A. E. Lita, T. Gerrits, I. Vayshenker, B. Baek, M. D. Shaw, R. P. Mirin, and S. W. Nam, "Detecting single infrared photons with 93% system efficiency," Nat. Photonics **7**(3), 210–214 (2013).
32. H. Le Jeannic, V. B. Verma, A. Cavaillès, F. Marsili, M. D. Shaw, K. Huang, O. Morin, S. W. Nam, and J. Laurat, "High-efficiency WSi superconducting nanowire single-photon detectors for quantum state engineering in the near infrared," Opt. Lett. **41**(22), 5341–5344 (2016).
33. J. Calsamiglia, S. M. Barnett, N. Lütkenhaus, and K.-A. Suominen, "Removal of a single photon by adaptive absorption," Phys. Rev. A **64**(4), 043814 (2001).
34. P. Marek, J. Provazník, and R. Filip, "Loop-based subtraction of a single photon from a traveling beam of light," Opt. Express **26**(23), 29837–29847 (2018).
35. V. Švarc, M. Nováková, G. Mazin, and M. Ježek, "Fully tunable and switchable coupler for photonic routing in quantum detection and modulation," Opt. Lett. **44**(23), 5844–5847 (2019).
36. J. Honer, R. Löw, H. Weimer, T. Pfau, and H. P. Büchler, "Artificial atoms can do more than atoms: deterministic single photon subtraction from arbitrary light fields," Phys. Rev. Lett. **107**(9), 093601 (2011).
37. S. Rosenblum, O. Bechler, I. Shomroni, Y. Lovsky, G. Guendelman, and B. Dayan, "Extraction of a single photon from an optical pulse," Nat. Photonics **10**(1), 19–22 (2016).
38. S. Gleyzes, S. Kuhr, C. Guerlin, J. Bernu, S. Deleglise, U. B. Hoff, M. Brune, J.-M. Raimond, and S. Haroche, "Quantum jumps of light recording the birth and death of a photon in a cavity," Nature **446**(7133), 297–300 (2007).
39. C. Guerlin, J. Bernu, S. Deleglise, C. Sayrin, S. Gleyzes, S. Kuhr, M. Brune, J.-M. Raimond, and S. Haroche, "Progressive field-state collapse and quantum non-demolition photon counting," Nature **448**(7156), 889–893 (2007).
40. S. Deleglise, I. Dotsenko, C. Sayrin, J. Bernu, M. Brune, J.-M. Raimond, and S. Haroche, "Reconstruction of non-classical cavity field states with snapshots of their decoherence," Nature **455**(7212), 510–514 (2008).
41. C. Sayrin, I. Dotsenko, X. Zhou, B. Peaudecerf, T. Rybarczyk, S. Gleyzes, P. Rouchon, M. Mirrahimi, H. Amini, M. Brune, J.-M. Raimond, and S. Haroche, "Real-time quantum feedback prepares and stabilizes photon number states," Nature **477**(7362), 73–77 (2011).
42. J. Hloušek, M. Dudka, I. Straka, and M. Ježek, "Accurate Detection of Arbitrary Photon Statistics," Phys. Rev. Lett. **123**(15), 153604 (2019).

Optics EXPRESS

43. R. Prevedel, P. Walther, F. Tiefenbacher, P. Böhi, R. Kaltenbaek, T. Jennewein, and A. Zeilinger, "High-speed linear optics quantum computing using active feed-forward," Nature **445**(7123), 65–69 (2007).
44. X. song Ma, S. Zotter, N. Tetik, A. Qarry, T. Jennewein, and A. Zeilinger, "A high-speed tunable beam splitter for feed-forward photonic quantum information processing," Opt. Express **19**(23), 22723–22730 (2011).
45. Y. He, X. Ding, Z.-E. Su, H.-L. Huang, J. Qin, C. Wang, S. Unsleber, C. Chen, H. Wang, Y.-M. He, X.-L. Wang, W.-J. Zhang, S.-J. Chen, C. Schneider, M. Kamp, L.-X. You, Z. Wang, S. Höfling, C.-Y. Lu, and J.-W. Pan, "Time-Bin-Encoded Boson Sampling with a Single-Photon Device," Phys. Rev. Lett. **118**(19), 190501 (2017).

# Chapter 7

# Conclusions

This Thesis represents an overview of photonic switching methods and their applications in quantum protocols. The research presented here compiles the results published in three articles: Firstly, we implemented a Mach-Zehnder interferometer with ultra-fast phase switching and demonstrated loop-based time multiplexing for qudit preparation and photon-number-resolving detection [1]. Secondly, a phase stabilization technique was developed, allowing for the stabilization of a single-photon interferometer and interferometric networks with ultra-high precision [2]. Thirdly, a protocol for probabilistic conversion between Fock states was proposed and implemented using a Mach-Zehnder interferometer with feedforward operation [3].

The first part of the Thesis discusses common methods of photonic switching and compares them in the context of quantum technology. The fastest response is enabled by interferometric schemes utilizing an integrated electro-optic modulator, while the lowest losses are achieved using polarization switching with Pockels cells. Possible approaches to active phase stabilization of single-photon interferometers are also discussed. The following chapter provides a brief overview of the theoretical and experimental tools used in the research. A detailed analysis of the Mach-Zehnder interferometer is performed with an emphasis on the phase estimation under real conditions. Further, technical aspects of phase stabilization and phase modulation are described. Additionally, detection, data processing, and basic tools of quantum optics relevant to our research are described. The subsequent chapters are focused on individual research projects.

In the work [1], we present a fast single-photon switch using phase modulation in a Mach-Zehnder interferometer. We aimed to achieve fast operation, high visibility, and full tunability. Therefore, we used a hybrid configuration of the Mach-Zehnder interferometer, combining fiber and free space. The fiber part allows for fast phase control via an integrated electro-optic phase

modulator with a 10 GHz bandwidth, while the free-space part allows for precise balancing of the interferometer together with dispersion compensation, polarization filtering, and dispersion-based phase tunability. With this approach, we achieved sub-nanosecond switching with an extinction of 26 dB for an optical bandwidth of 1.3 THz. Further, using a loop configuration of the photonic switch, we performed temporal multiplexing. The incident pulse is trapped into a loop, and during each roundtrip, a fraction is split to the output depending on the switched phase. Using this approach, we demonstrate full control over four time bins with a mean fidelity of 98.9%. The potential applications are photon-number-resolving detection and qudit encoding. Although the presented switch is impractical for the applications due to 7 dB of loss, a low-loss polarization-based switch enabling practical temporal multiplexing is being developed.

In the work [2], we focused on optimizing the phase stabilization of a single-photon Mach-Zehnder interferometer with fast phase switching [2]. A typical problem of interferometers is their phase instability caused by environmental fluctuations. To stabilize the interferometer, we use an auxiliary light acting as the phase reference. The reference is operating at a different wavelength than the quantum signal. The advantage of this approach is in continuous operation and the independence of the quantum signal. Additionally, a strong reference can be used, achieving much greater speed and precision of phase stabilization compared to a single-photon reference. However, to achieve maximum precision in the long term, additional requirements must be satisfied. Firstly, the spectral stability of the reference and signal beams must be ensured to exclude their mutual phase shift. Secondly, phase stabilization must be independent of the overall intensity of the reference beam. In this work, we discuss these problems and propose their solutions, e.g., by using adaptive setpoint. Furthermore, we discuss other sources of errors in phase stabilization, namely local detuning in the interferometer. The experimental implementation of phase stabilization utilizes an active feedback loop with a 1 kHz response, consisting of an analog PID controller, a fiber phase modulator, and sensitive photodiodes. Thanks to a thorough optimization of the interferometer and stabilization over all available parameters, we achieved exceptional phase stability of 0.05 degrees for 15 hours, exceeding any previous results in the field of single-photon interferometer stabilization by 1 or 2 orders of magnitude. Moreover, due to the low power of the reference (1 nW) and efficient wavelength separation, crosstalk from the reference to the single-photon signal is negligible.

In the work [3], we proposed and experimentally implemented a probabilistic protocol for the conversion between Fock states. Fock state conversion enables the preparation of highly non-classical states, which can serve as

resources for quantum information protocols. In our approach, photon subtraction is used to transform a state with a higher photon number into a state with a lower photon number. In each subtraction step, the results of all previous subtraction steps are considered, enabling the conversion with maximal probability. This task is implemented by a sequence of beam splitters with feedforward-controlled splitting ratios. The theoretical analysis shows that the probability of successful conversion is around 85% (depending on the type of conversion) using a sequence of nine splitters. We also investigate the influence of losses and limited detection efficiency on the protocol. The analysis reveals that the protocol can offer an advantage over passive conversion if the losses in the switchable beam splitter are lower than the losses during detection. We experimentally demonstrated a model case of $|2\rangle \rightarrow |1\rangle$ conversion using a sequence of two splitters. This was achieved using a Mach-Zehnder interferometer with feedforward operation and a passive tunable beam splitter. By measuring on a coincidence basis, we replicated the theoretical predictions of a 66.6% conversion success rate.

Currently, we have been developing a polarization-based photonic switch with the aim of minimizing the loss while keeping the speed moderate. Together with the switch, we develop an ultra-low-loss optical delay line based on multiple reflections between plane mirrors. Apart from the loss, we aim for a high stability of the delay line and to reduce beam aberrations. So far, we have implemented a switch-delay-line setup with 6.5% of roundtrip loss, a 60 ns switching window, and 25 partially dependent switching levels. Especially in terms of the switching levels, our results are unique. However, the development of the setup is still in progress thus further improvements are possible. As a first application of the prototype switching setup, we plan to realize a photon-number-resolving detector. Combining multiplexing in time and space, we aim for more than 30 balanced detection channels.

Fast photonic switching and precise phase stabilization are essential building blocks in quantum information processing as well as in quantum communication. The conversion of Fock states enables the preparation of highly non-classical states and the realization of a wide range of quantum operations. Therefore, we believe that our results will contribute to the development of quantum optics and quantum technologies.

# Shrnutí výsledků práce v češtině

Tato disertační práce se zabývá experimentální realizací jednofotonového fotonického spínání pomocí interferometrů s rychlým fázovým spínáním a dopřednou vazbou, které jsou následně využity pro experimenty a techniky související s kvantově informatickými protokoly. Zaprvé, pomocí Mach-Zehnderova interferometru s rychlým fázovým spínáním a plnou fázovou laditelností byl demonstrován princip přípravy vícedimenzionálních kvantových stavů pomocí rozdělení vstupního pulsu do několika časových oken [1]. Zadruhé, byla vyvinuta technika fázové stabilizace, umožňující stabilizovat jednofotonový interferometr a interferometrické sítě s vysokou přesností po dobu desítek hodin [2]. Zatřetí, pomocí Mach-Zehnderova interferometru s dopřednou vazbou byl realizován protokol pro probabilistickou konverzi mezi Fockovými stavy [3].

V první části práce jsou diskutovány různé metody fotonického spínání a porovnánány v kontextu kvantové technologie. Nejrychlejší odezvu umožňují interferometrická schémata využívající integrovaný elektro-optický modulátor, zatímco nejnižší ztráty představuje polarizační spínání pomocí Pockelsových cel. Dále jsou diskutovány možné přístupy k aktivní fázové stabilizaci jednofotonových interferometrů. Další kapitola obsahuje stručný přehled teoretických a experimentálních nástrojů, které byly využity v rámci výzkumu. Je proveden detailní rozbor Mach-Zehnderova interferometru a nastíněny technické aspekty fázové stabilizace a fázové modulace. Dále je popsána detekce, zpracování dat a základní nástoje kvantové optiky relevantní pro tuto práci. Následující kapitoly se zabývají jednotlivými výzkumnými projekty.

V práci [1] je prezentován rychlý jednofotonový přepínač využívající fázovou modulaci v Mach-Zehnderově interferometeru. V našem přístupu jsme se zaměřili primárně na rychlé fázové spínání a vysokou vizibilitu. Rychlé fázové spínání je zajištěno pomocí integrovaného elektro-optického modulátoru s 10 GHz šířkou pásma. Kromě vláknových prvků však interferometr obsahuje i objemové elementy, což umožňuje přesné srovnání ramen interferometru a umístění disperzních elementů pro kompenzaci disperze a dosažení plné fázové laditelnosti. Díky tomuto přístupu jsme dosáhli libovolného subnanosekundového spínání s extinkcí 26 dB pro šířku optického spektra 1.3 THz. Dále jsme demonstrovali dvě aplikace fotonického spínače. Propojením jednoho výstupu se vstupem interferometru jsme dostali takzvanou smyčkovou konfiguraci, díky níž mohl být interferometr využit několikanásobně. Zaprvé jsme demonstrovali rozdělení vstupního pulsu do čtyř časových oken, což v závislosti na obsazenosti oken odpovídá různým kvantovým stavům s dimenzí 4. Zadruhé, ve speciálním případě, kdy jsou všechna okna stejně

obsazena a na výstup umístíme jednofotonový detektor, dostáváme zařízení rozlišující počet fotonů.

V článku [2] jsme se zaměřili na dosažení co nejlepší fázové stabilizace Mach-Zehnderova interferometru s rychlým fázovým spínáním [2]. Typickým problémem interferometrů je totiž jejich fázová nestabilita způsobena fluktuacemi prostředí. Aby bylo zamezeno spontánnímu fázovému driftu v interferometru, je třeba jej stabilizovat. Náš přístup spočíval ve využití dvou vlnových délek – na jedné vlnové délce je nesen kvantový signál a druhá vlnová délka slouží jako fázová reference. Výhodou tohoto přístupu je, že fázová stabilizace je prováděna kontinuálně a nezávisle na kvantovém signálu. Navíc je možné použít relativně silný referenční svazek, a tím dosáhnout mnohem větší rychlosti a přesnosti fázové stabilizace než by tomu bylo v případě jednofotonového referenčního svazku. Pro dosažení maximální přesnosti i v dlouhočasové škále je však třeba zajistit další požadavky. Zaprvé je třeba zajistit spektrální stabilitu referenčního a signálního svazku, a tím vyloučit jejich vzájemné fázové rozposunutí. Zadruhé, fázová stabilizace musí být nezávislá na celkové intenzitě referenčního svazku. V práci tyto problémy diskutujeme a navrhujeme jejich řešení. Dále diskutujeme další zdoje chyb fázové stabilizace, a to lokální fluktuace intenzity v interferometeru. Experimentální realizace fázové stabilizace využívá aktivní zpětnovazební smyčku s 1 kHz odezvou složenou z analogové PID regulace, vláknového fázového modulátoru a citlivých fotodiod. Díky důkladné optimalizaci interferometru i stabilizace přes všechny dostupné parametry jsme byli schopni dosáhnout výjimečné fázové stability 0,05° po dobu 15 hodin, což je o 1-2 řády lepší výsledek než jaké byly dosud dosaženy v oblasti stabilizace jednofotonových inferferometrů. Navíc, díky nízkému výkonu referenčního svazku (1 nW) a kvalitní separaci vlnových délek jsou přeslechy z referenčního svazku do jednofotonového signálu zanedbatelné.

V článku [3] jsme navrhli a experimentálně realizovali probabilistický protokol konverze mezi Fockovými stavy. Konverze Fockových stavů umožňuje připravit vysoce neklasické stavy, jež mohou být zdrojem pro kvantově-informatické protokoly. V našem případě navrhujeme konverzi směrem dolů, tedy měníme stav s vyšším počtem fotonů na stav s nižším počtem fotonů. K tomu využíváme síť děličů svazku, jejichž dělicí poměr je ovládán pomocí dopředné vazby. Z teoretické analýzy vyplývá, že pravděpodobnost úspěšné konverze je okolo 85% (v závislosti na typu konverze) při použití sekvence 9 děličů. Dále vyšetřujeme vliv ztrát a omezené detekční účinnosti na protokol. Z analýzy plyne, že protokol může nabídnout jistou výhodu oproti pasivní konverzi pokud jsou ztráty na spinatelném děliči nižší než ztráty při detekci. Dále jsme experimentálně demonstrovali modelový případ $|2\rangle \rightarrow |1\rangle$ konverze pomocí sekvence 2 děličů. Toho jsme docílili pomocí Mach-Zehnderova interferome-

tru s dopřednou vazbou a pasivního laditelného děliče svazku. Při měření v koincidenční bázi jsme dokázali zreplikovat teoretické predikce úspěšnosti této konverze 66,6%.

Nyní pracujeme na nové generaci fotonického spínače, který je optimalizován na ztráty. Společně se spínačem vyvíjíme nízkoztrátovou zpožďovací linku umožňující realizaci komplexních kvantových protokolů využívajících časové multiplexování. Náš přístup využívá polarizační spínání ve volném prostoru a optickou zpožďovací linku pomocí několikanásobného odrazu na zrcátcích. Celý systém má 6.5% ztrát na oběh, délku spínacího okna 60 ns a 25 částečně závislých hladin. Zejména co se týče počtu hladin, jsou naše parametry unikátní. Celý systém je však stále ve vývoji a další zlepšení v budoucnu jsou možná. Nejbližší plánovaná aplikace fotonického spínače je realizace detektoru rozlišujícího počet fotonů. Využitím časového i prostorového multiplexingu plánujeme zrealizovat více než 30 vyvážených detekčních kanálů.

Výsledky našeho výzkumu rozšiřují dostupné metody fotonického spínání a obohacují pole kvantové optiky a kvantových technologií. Rychlé fotonické spínání i přesná fázová stabilizace jsou důležitými stavebními bloky nejen v kvantovém zpracování informace, ale i kvantových komunikacích. Konverze Fockových stavů umožňuje přípravu vysoce neklasických stavů a realizaci široké škály kvantových operací.

# References


[1] V. Švarc, M. Nováková, G. Mazin, and M. Ježek, "Fully tunable and switchable coupler for photonic routing in quantum detection and modulation," *Opt. Lett.*, vol. 44, no. 23, pp. 5844–5847, 2019.

[2] V. Švarc, M. Nováková, M. Dudka, and M. Ježek, "Sub-0.1 degree phase locking of a single-photon interferometer," *Opt. Express*, vol. 31, no. 8, pp. 12562–12571, 2023.

[3] V. Švarc, J. Hloušek, M. Nováková, J. Fiurášek, and M. Ježek, "Feedforward-enhanced Fock state conversion with linear optics," *Opt. Express*, vol. 28, no. 8, pp. 11634–11644, 2020.

[4] J. Aasi, J. Abadie, B. Abbott, R. Abbott, T. Abbott, M. Abernathy, C. Adams, T. Adams, P. Addesso, R. Adhikari, *et al.*, "Enhanced sensitivity of the LIGO gravitational wave detector by using squeezed states of light," *Nature Photonics*, vol. 7, no. 8, pp. 613–619, 2013.

[5] H.-S. Zhong, H. Wang, Y.-H. Deng, M.-C. Chen, L.-C. Peng, Y.-H. Luo, J. Qin, D. Wu, X. Ding, Y. Hu, *et al.*, "Quantum computational advantage using photons," *Science*, vol. 370, no. 6523, pp. 1460–1463, 2020.

[6] F. Bova, A. Goldfarb, and R. G. Melko, "Commercial applications of quantum computing," *EPJ quantum technology*, vol. 8, no. 1, p. 2, 2021.

[7] J. M. Lukens, N. T. Islam, C. C. W. Lim, and D. J. Gauthier, "Reconfigurable generation and measurement of mutually unbiased bases for time-bin qudits," *Applied Physics Letters*, vol. 112, no. 11, p. 111102, 2018.

[8] A. Schreiber, A. Gábris, P. P. Rohde, K. Laiho, M. Štefaňák, V. Potoček, C. Hamilton, I. Jex, and C. Silberhorn, "A 2D quantum walk simulation of two-particle dynamics," *Science*, vol. 336, no. 6077, pp. 55–58, 2012.

[9] K. R. Motes, A. Gilchrist, J. P. Dowling, and P. P. Rohde, "Scalable boson sampling with time-bin encoding using a loop-based architecture," *Phys. Rev. Lett.*, vol. 113, no. 12, p. 120501, 2014.

[10] Y. He, X. Ding, Z.-E. Su, H.-L. Huang, J. Qin, C. Wang, S. Unsleber, C. Chen, H. Wang, Y.-M. He, X.-L. Wang, W.-J. Zhang, S.-J. Chen, C. Schneider, M. Kamp, L.-X. You, Z. Wang, S. Höfling, C.-Y. Lu, and J.-W. Pan, "Time-bin-encoded boson sampling with a single-photon device," *Phys. Rev. Lett.*, vol. 118, no. 19, p. 190501, 2017.

[11] H. Wang, J. Qin, X. Ding, M.-C. Chen, S. Chen, X. You, Y.-M. He, X. Jiang, L. You, Z. Wang, *et al.*, "Boson sampling with 20 input photons and a 60-mode interferometer in a $10^{14}$-dimensional hilbert space," *Phys. Rev. Lett.*, vol. 123, no. 25, p. 250503, 2019.

[12] P. P. Rohde, "Simple scheme for universal linear-optics quantum computing with constant experimental complexity using fiber loops," *Phys. Rev. A*, vol. 91, no. 1, p. 012306, 2015.

[13] S. Takeda and A. Furusawa, "Universal quantum computing with measurement-induced continuous-variable gate sequence in a loop-based architecture," *Phys. Rev. Lett.*, vol. 119, p. 120504, 2017.

[14] S. Takeda, K. Takase, and A. Furusawa, "On-demand photonic entanglement synthesizer," *Sci. Adv.*, vol. 5, no. 5, p. eaaw4530, 2019.

[15] K. Yonezu, Y. Enomoto, T. Yoshida, and S. Takeda, "Universal multi-mode linear optical quantum operation in time domain," in *Frontiers in Optics*, pp. JTu5A–33, Optica Publishing Group, 2022.

[16] F. Vedovato, C. Agnesi, M. Tomasin, M. Avesani, J.-A. Larsson, G. Vallone, and P. Villoresi, "Post-selection-loophole-free Bell violation with genuine time-bin entanglement," *Phys. Rev. Lett.*, vol. 121, p. 190401, 2018.

[17] C. Xiong, X. Zhang, Z. Liu, M. J. Collins, A. Mahendra, L. G. Helt, M. J. Steel, D.-Y. Choi, C. J. Chae, P. H. W. Leong, and B. J. Eggleton, "Active temporal multiplexing of indistinguishable heralded single photons," *Nat. Commun.*, vol. 7, p. 10853, 2016.

[18] G. J. Mendoza, R. Santagati, J. Munns, E. Hemsley, M. Piekarek, E. Martín-López, G. D. Marshall, D. Bonneau, M. G. Thompson, and J. L. O'Brien, "Active temporal and spatial multiplexing of photons," *Optica*, vol. 3, no. 2, pp. 127–132, 2016.

[19] F. Kaneda and P. G. Kwiat, "High-efficiency single-photon generation via large-scale active time multiplexing," *Science advances*, vol. 5, no. 10, p. eaaw8586, 2019.

[20] E. Meyer-Scott, C. Silberhorn, and A. Migdall, "Single-photon sources: Approaching the ideal through multiplexing," *Review of Scientific Instruments*, vol. 91, no. 4, p. 041101, 2020.

[21] J. Tiedau, E. Meyer-Scott, T. Nitsche, S. Barkhofen, T. J. Bartley, and C. Silberhorn, "A high dynamic range optical detector for measuring single photons and bright light," *Opt. Express*, vol. 27, pp. 1–15, 2019.

[22] C. Wang, M. Zhang, X. Chen, M. Bertrand, A. Shams-Ansari, S. Chandrasekhar, P. Winzer, and M. Lončar, "Integrated lithium niobate electro-optic modulators operating at CMOS-compatible voltages," *Nature*, 2018.

[23] V. Makarov, A. Brylevski, and D. R. Hjelme, "Real-time phase tracking in single-photon interferometers," *Appl. Opt.*, vol. 43, no. 22, pp. 4385–4392, 2004.

[24] D. Pulford, C. Robillard, and E. Huntington, "Single photon locking of an all-fiber interferometer," *Rev. Sci. Instrum.*, vol. 76, no. 6, p. 063114, 2005.

[25] G. B. Xavier and J. P. von der Weid, "Stable single-photon interference in a 1 km fiber-optic Mach–Zehnder interferometer with continuous phase adjustment," *Opt. Lett.*, vol. 36, no. 10, pp. 1764–1766, 2011.

[26] P. Toliver, J. M. Dailey, A. Agarwal, and N. A. Peters, "Continuously active interferometer stabilization and control for time-bin entanglement distribution," *Opt. Express*, vol. 23, no. 4, pp. 4135–4143, 2015.

[27] S.-B. Cho and H. Kim, "Active stabilization of a fiber-optic two-photon interferometer using continuous optical length control," *Opt. Express*, vol. 24, no. 10, pp. 10980–10986, 2016.

[28] M. Miková, H. Fikerová, I. Straka, M. Mičuda, J. Fiurášek, M. Ježek, and M. Dušek, "Increasing efficiency of a linear-optical quantum gate using electronic feed-forward," *Phys. Rev. A*, vol. 85, no. 1, p. 012305, 2012.

[29] X.-s. Ma, S. Zotter, J. Kofler, R. Ursin, T. Jennewein, Č. Brukner, and A. Zeilinger, "Experimental delayed-choice entanglement swapping," *Nature Physics*, vol. 8, no. 6, pp. 479–484, 2012.

[30] A. Alarcon, P. González, J. Cariñe, G. Lima, and G. B. Xavier, "Polarization-independent single-photon switch based on a fiber-optical Sagnac interferometer for quantum communication networks," *Opt. Express*, vol. 28, no. 22, pp. 33731–33738, 2020.

[31] D. A. B. Miller, "Perfect optics with imperfect components," *Optica*, vol. 2, no. 8, p. 747, 2015.

[32] K. Suzuki, G. Cong, K. Tanizawa, S.-H. Kim, K. Ikeda, S. Namiki, and H. Kawashima, "Ultra-high-extinction-ratio 2x2 silicon optical switch with variable splitter," *Opt. Express*, vol. 23, no. 7, p. 9086, 2015.

[33] C. M. Wilkes, X. Qiang, J. Wang, R. Santagati, S. Paesani, X. Zhou, D. A. B. Miller, G. D. Marshall, M. G. Thompson, and J. L. O'Brien, "60 dB high-extinction auto-configured Mach-Zehnder interferometer," *Opt. Lett.*, vol. 41, no. 22, p. 5318, 2016.

[34] S. Liu, H. Cai, C. T. DeRose, P. Davids, A. Pomerene, A. L. Starbuck, D. C. Trotter, R. Camacho, J. Urayama, and A. Lentine, "High speed ultra-broadband amplitude modulators with ultrahigh extinction $>$ 65 dB," *Opt. Express*, vol. 25, no. 10, p. 11254, 2017.

[35] X. song Ma, S. Zotter, N. Tetik, A. Qarry, T. Jennewein, and A. Zeilinger, "A high-speed tunable beam splitter for feed-forward photonic quantum information processing," *Opt. Express*, vol. 19, no. 23, pp. 22723–22730, 2011.

[36] J. Wang, S. Paesani, Y. Ding, R. Santagati, P. Skrzypczyk, A. Salavrakos, J. Tura, R. Augusiak, L. Mančinska, D. Bacco, *et al.*, "Multidimensional quantum entanglement with large-scale integrated optics," *Science*, vol. 360, no. 6386, pp. 285–291, 2018.

[37] Y. Ding, C. Peucheret, H. Ou, and K. Yvind, "Fully etched apodized grating coupler on the SOI platform with -0.58 db coupling efficiency," *Opt. Lett.*, vol. 39, no. 18, pp. 5348–5350, 2014.

[38] J. Nauriyal, M. Song, R. Yu, and J. Cardenas, "Fiber-to-chip fusion splicing for low-loss photonic packaging," *Optica*, vol. 6, no. 5, pp. 549–552, 2019.

[39] M. A. Hall, J. B. Altepeter, and P. Kumar, "Ultrafast switching of photonic entanglement," *Phys. Rev. Lett.*, vol. 106, p. 053901, 2011.

[40] G. Roberts, M. Pittaluga, M. Minder, M. Lucamarini, J. Dynes, Z. Yuan, and A. Shields, "Patterning-effect mitigating intensity modulator for secure decoy-state quantum key distribution," *Opt. Lett.*, vol. 43, no. 20, pp. 5110–5113, 2018.

[41] M. Mičuda, E. Doláková, I. Straka, M. Miková, M. Dušek, J. Fiurášek, and M. Ježek, "Highly stable polarization independent Mach-Zehnder interferometer," *Rev. Sci. Instrum.*, vol. 85, no. 8, p. 083103, 2014.

[42] G. L. Zanin, M. J. Jacquet, M. Spagnolo, P. Schiansky, I. A. Calafell, L. A. Rozema, and P. Walther, "Fiber-compatible photonic feed-forward with 99% fidelity," *Opt. Express*, vol. 29, no. 3, pp. 3425–3437, 2021.

[43] S. Baur, D. Tiarks, G. Rempe, and S. Dürr, "Single-photon switch based on Rydberg blockade," *Phys. Rev. Lett.*, vol. 112, no. 7, p. 073901, 2014.

[44] T. Volz, A. Reinhard, M. Winger, A. Badolato, K. J. Hennessy, E. L. Hu, and A. Imamoğlu, "Ultrafast all-optical switching by single photons," *Nature Photonics*, vol. 6, no. 9, pp. 605–609, 2012.

[45] A. Pscherer, M. Meierhofer, D. Wang, H. Kelkar, D. Martín-Cano, T. Utikal, S. Götzinger, and V. Sandoghdar, "Single-molecule vacuum Rabi splitting: Four-wave mixing and optical switching at the single-photon level," *Phys. Rev. Lett.*, vol. 127, no. 13, p. 133603, 2021.

[46] W. K. Wootters and W. H. Zurek, "A single quantum cannot be cloned," *Nature*, vol. 299, no. 5886, pp. 802–803, 1982.

[47] S. Suzuki, H. Yonezawa, F. Kannari, M. Sasaki, and A. Furusawa, "7 dB quadrature squeezing at 860 nm with periodically poled $KTiOPO_4$," *Appl. Phys. Lett.*, vol. 89, no. 6, p. 061116, 2006.

[48] Y. Takeno, M. Yukawa, H. Yonezawa, and A. Furusawa, "Observation of -9 dB quadrature squeezing with improvement of phase stability in homodyne measurement," *Opt. Express*, vol. 15, no. 7, pp. 4321–4327, 2007.

[49] T. Eberle, V. Händchen, and R. Schnabel, "Stable control of 10 dB two-mode squeezed vacuum states of light," *Opt. Express*, vol. 21, no. 9, pp. 11546–11553, 2013.

[50] V. Giovannetti, S. Lloyd, and L. Maccone, "Advances in quantum metrology," *Nature Photonics*, vol. 5, no. 4, pp. 222–229, 2011.

[51] G. Thekkadath, M. Mycroft, B. Bell, C. Wade, A. Eckstein, D. Phillips, R. Patel, A. Buraczewski, A. Lita, T. Gerrits, *et al.*, "Quantum-enhanced interferometry with large heralded photon-number states," *NPJ Quantum Information*, vol. 6, no. 1, pp. 1–6, 2020.

[52] G. Carvacho, J. Cariñe, G. Saavedra, Á. Cuevas, J. Fuenzalida, F. Toledo, M. Figueroa, A. Cabello, J.-Å. Larsson, P. Mataloni, G. Lima, and G. B. Xavier, "Postselection-Loophole-Free Bell Test Over an Installed Optical Fiber Network," *Phys. Rev. Lett.*, vol. 115, no. 3, p. 030503, 2015.

[53] Y. Xu, J. Lin, Y. Li, H. Dai, S. Liao, and C. Peng, "Active Phase stabilization for the interferometer with 128 actively selectable paths," *IEEE Trans. Nucl. Sci.*, vol. 66, no. 7, pp. 1076–1080, 2019.

[54] A. Cuevas, G. Carvacho, G. Saavedra, J. Cariñe, W. Nogueira, M. Figueroa, A. Cabello, P. Mataloni, G. Lima, and G. Xavier, "Long-distance distribution of genuine energy-time entanglement," *Nature Communications*, vol. 4, no. 1, p. 2871, 2013.

[55] M. Dall'Arno, A. Bisio, G. M. D'Ariano, M. Miková, M. Ježek, and M. Dušek, "Experimental implementation of unambiguous quantum reading," *Phys. Rev. A*, vol. 85, no. 1, p. 012308, 2012.

[56] M. Miková, H. Fikerová, I. Straka, M. Mičuda, M. Ježek, M. Dušek, and R. Filip, "Carrying qubits with particles whose noninformational degrees of freedom are nonfactorable," *Phys. Rev. A*, vol. 87, no. 4, p. 042327, 2013.

[57] M. Miková, M. Sedlák, I. Straka, M. Mičuda, M. Ziman, M. Ježek, M. Dušek, and J. Fiurášek, "Optimal entanglement-assisted discrimination of quantum measurements," *Phys. Rev. A*, vol. 90, no. 2, p. 022317, 2014.

[58] M. Miková, I. Straka, M. Mičuda, V. Krčmarský, M. Dušek, M. Ježek, J. Fiurášek, and R. Filip, "Faithful conditional quantum state transfer between weakly coupled qubits," *Scientific Reports*, vol. 6, no. 1, p. 32125, 2016.

[59] G. Jotzu, T. J. Bartley, H. B. Coldenstrodt-Ronge, B. J. Smith, and I. A. Walmsley, "Continuous phase stabilization and active interferometer control using two modes," *Journal of Modern Optics*, vol. 59, no. 1, pp. 42–45, 2012.

[60] S. Wu, W. Huang, P. Yang, S. Liu, and L. Chen, "Arbitrary phase-locking in Mach–Zehnder interferometer," *Opt. Commun.*, vol. 442, pp. 148–151, 2019.

[61] P. Roztocki, B. MacLellan, M. Islam, C. Reimer, B. Fischer, S. Sciara, R. Helsten, Y. Jestin, A. Cino, S. T. Chu, *et al.*, "Arbitrary phase access for stable fiber interferometers," *Laser & Photonics Reviews*, vol. 15, no. 7, p. 2000524, 2021.

[62] S. Yanikgonul, R. Guo, A. Xomalis, A. N. Vetlugin, G. Adamo, C. Soci, and N. I. Zheludev, "Phase stabilization of a coherent fiber network by single-photon counting," *Opt. Lett.*, vol. 45, no. 10, pp. 2740–2743, 2020.

[63] S.-B. Cho and T.-G. Noh, "Stabilization of a long-armed fiber-optic single-photon interferometer," *Opt. Express*, vol. 17, no. 21, pp. 19027–19032, 2009.

[64] V. Švarc, "Aktivní fázová stabilizace interferometru pomocí zpětnovazební PID regulace." Bachelor's Thesis, Palacký University Olomouc, 2016.

[65] V. Švarc, "Active phase stabilization of fiber interferometers for single photon measurements." Master's Thesis, Palacký University Olomouc, 2018.

[66] M. Nováková, L. Podhora, V. Švarc, and M. Ježek, "Polarization-maintaining 3D printed fiber stretcher," *in preparation*, 2023.

[67] "Thorlabs 10A manual (online)." https://www.thorlabs.us/drawings/27607916c5eee514-CAFF97CF-D440-A31B-33A3C5C579C145D4/PDF10A2-Manual.pdf.

[68] D. W. Allan, "Statistics of atomic frequency standards," *Proceedings of the IEEE*, vol. 54, no. 2, pp. 221–230, 1966.

[69] D. V. Land, A. P. Levick, and J. W. Hand, "The use of the Allan deviation for the measurement of the noise and drift performance of microwave radiometers," *Measurement Science and Technology*, vol. 18, no. 7, p. 1917, 2007.

[70] P. Kok, W. J. Munro, K. Nemoto, T. C. Ralph, J. P. Dowling, and G. J. Milburn, "Linear optical quantum computing with photonic qubits," *Reviews of modern physics*, vol. 79, no. 1, p. 135, 2007.

[71] M. O. Scully and M. S. Zubairy, *Quantum Optics*. Cambridge University Press, 1997.

[72] P. Senellart, G. Solomon, and A. White, "High-performance semiconductor quantum-dot single-photon sources," *Nature nanotechnology*, vol. 12, no. 11, pp. 1026–1039, 2017.

[73] Y. Arakawa and M. J. Holmes, "Progress in quantum-dot single photon sources for quantum information technologies: A broad spectrum overview," *Applied Physics Reviews*, vol. 7, no. 2, 2020.

[74] K. Banaszek and I. A. Walmsley, "Photon counting with a loop detector," *Opt. Lett.*, vol. 28, no. 1, p. 52, 2003.

[75] M. Prilmüller, T. Huber, M. Müller, P. Michler, G. Weihs, and A. Predojević, "Hyperentanglement of photons emitted by a quantum dot," *Phys. Rev. Lett.*, vol. 121, no. 11, p. 110503, 2018.

[76] J. Wenger, R. Tualle-Brouri, and P. Grangier, "Non-Gaussian statistics from individual pulses of squeezed light," *Phys. Rev. Lett.*, vol. 92, no. 15, p. 153601, 2004.

[77] A. Zavatta, S. Viciani, and M. Bellini, "Quantum-to-classical transition with single-photon-added coherent states of light," *Science*, vol. 306, no. 5696, pp. 660–662, 2004.

[78] A. Ourjoumtsev, R. Tualle-Brouri, J. Laurat, and P. Grangier, "Generating optical Schrödinger kittens for quantum information processing," *Science*, vol. 312, no. 5770, pp. 83–86, 2006.

[79] J. Neergaard-Nielsen, B. Nielsen, C. Hettich, K. Mølmer, and E. Polzik, "Generation of a superposition of odd photon number states for quantum information networks," *Phys. Rev. Lett.*, vol. 97, no. 8, p. 083604, 2006.

[80] K. Wakui, H. Takahashi, A. Furusawa, and M. Sasaki, "Photon subtracted squeezed states generated with periodically poled KTiOPO 4," *Opt. Express*, vol. 15, no. 6, pp. 3568–3574, 2007.

[81] N. Namekata, Y. Takahashi, G. Fujii, D. Fukuda, S. Kurimura, and S. Inoue, "Non-Gaussian operation based on photon subtraction using a photon-number-resolving detector at a telecommunications wavelength," *Nat. Photonics*, vol. 4, no. 9, p. 655, 2010.

[82] M. Bellini and A. Zavatta, "Manipulating light states by single-photon addition and subtraction," in *Prog. Optics*, vol. 55, pp. 41–83, Elsevier, 2010.

[83] T. Gerrits, S. Glancy, T. S. Clement, B. Calkins, A. E. Lita, A. J. Miller, A. L. Migdall, S. W. Nam, R. P. Mirin, and E. Knill, "Generation of optical coherent-state superpositions by number-resolved photon subtraction from the squeezed vacuum," *Phys. Rev. A*, vol. 82, no. 3, p. 031802, 2010.

[84] J. Calsamiglia, S. M. Barnett, N. Lütkenhaus, and K.-A. Suominen, "Removal of a single photon by adaptive absorption," *Phys. Rev. A*, vol. 64, no. 4, p. 043814, 2001.

[85] P. Marek, J. Provazník, and R. Filip, "Loop-based subtraction of a single photon from a traveling beam of light," *Opt. Express*, vol. 26, no. 23, pp. 29837–29847, 2018.